Experimental and Numerical Investigation of Mass

Transfer in Passive Scaled-up Micromixers

Kristina Jenna Cook

A Thesis

in

The Department

of

Mechanical and Industrial Engineering

Presented in Partial Fulfillment of the Requirements

for the Degree of Master of Applied Science (Mechanical Engineering) at

Concordia University

Montréal, Québec, Canada

March 2012

CONCORDIA UNIVERSITY
School of Graduate Studies

This is to certify that the thesis prepared

By: Kristina Jenna Cook

Entitled: Experimental and Numerical Investigation of Mass Transfer in Passive Scaled-up Micromixers

and submitted in partial fulfillment of the requirements for the degree of

Master of Applied Science (Mechanical Engineering)

complies with the regulations of the University and meets the accepted standards with respect to originality and quality.

Signed by the final examining committee:

Dr. M. Medraj _____ Chair

Dr. F. Haghighat _____ Examiner

Dr. G. Vatistas _____ Examiner

Dr. I. Hassan _____ Supervisor

Approved by _____
          Chair of Department or Graduate Program Director

_____
Dean of Faculty

Date   March 5, 2012

Abstract

Experimental and Numerical Investigation of Mass Transfer in Passive Scaled-up Micromixers

Kristina Jenna Cook

Micromixers are vital components in micro-total analysis systems (µ-TAS) and Lab-on-Chip (LOC) devices, with applications in drug delivery, medical diagnostics, and chemical analyses, amongst others. Traditional macroscale mixing techniques may not be applied at the microscale, where viscous forces become important compared to inertial forces. As such, it remains a challenge to effectively and thoroughly mix liquid species in small characteristic dimensions.

The present work aims to analyze flow phenomena and mass transfer in three novel scaled-up micromixers, which make use of variations in channel geometry to induce mixing. Designs based on multi-lamination inlets, obstruction filled channels, Dean vortex inducing curved channels, and helical flow inducing grooves are investigated. Flow visualization is used as a qualitative tool, providing valuable information regarding flow patterns and mixing. Induced fluorescence is applied to assess whole field concentration distribution, and provide quantitative species

distribution data. Complex three dimensional flows are analyzed using numerical simulations, which show good agreement with experimental work.

The mixers are evaluated over Reynolds numbers ranging from 0.5 to 100, corresponding to Péclet numbers ranging from 1.25×10^3 to 1.25×10^5. Results show a decreasing-increasing trend in the degree of mixing with increasing Reynolds number, as the dominant mixing mechanism changes from mass diffusion to mass advection. Up to 90% mixing is reported. To allow for reasonable mixing performance comparison with published work, an equivalent length parameter is proposed. The present devices offer good mixing in shorter lengths over a wide range of Reynolds numbers compared to numerous published devices.

Acknowledgements

I would first like to thank Dr. Hassan for igniting my interest in research, and providing guidance throughout my undergraduate and graduate career. The knowledge and work ethic I've gained under his supervision are invaluable, and I am incredibly grateful for the opportunities and encouragement he has provided. I am also grateful to FQRNT for financial support.

Thank you to current and past group members, including Dino, Amen, Mohamed, Carole, Othman, Hani, Ming and Ling. The friendships formed will always be remembered. Fan, thank you for imparting your knowledge onto me, and for all the good laughs. I'd also like to thank my close friends for their encouragement.

Mom, Dad, and Ian, thank you for your love, support and encouragement. It is impossible to express how grateful I am for everything you've taught me, including the value of hard work and that dreams are never out of reach. Peter, *mon amour*, thank you for making every day brighter, and for always believing in me.

If I have seen further it is by standing on the shoulders of giants

- Issac Netwon

Table of Contents

List of Figures

Nomenclature

List of Symbols

A	Area [m^2]
A_i	Area at inlet [m^2]
C	Concentration [$\mu g/L$]
D	Diffusion coefficient [$m^2 \cdot s^{-1}$]
D_H	Hydraulic diameter [m]
H	Channel height [m]
H_g	Groove height [m]
I	Fluorescence Intensity [a.u.]
j_{diff}	Diffusive flux [$kg \cdot m^{-2} \cdot s^{-1}$]
j_{conv}	Convective flux [$kg \cdot m^{-2} \cdot s^{-1}$]
L	Length [m]
$\dot{m}$	Mass flow rate [$kg \cdot s^{-1}$]
N	Total number of data points
p	Path of diffusion [m]
P	Pressure [$kg \cdot m^{-1} \cdot s^{-2}$]
R	Mean radius of curvature, $(R_{in} + R_{out})/2$
R_{in}	Inner radius [m]
R_{out}	Outer radius [m]
t	Thickness [m]

U	Average velocity [m·s^{-1}]
$\vec{V}$	Velocity vector [m·s^{-1}]
W	Width [m]
W_A	Width of inlet A [m]
W_B	Width of inlet B [m]
w_p	Width of pin [mm]
x	Distance along x-axis [m]
y	Distance along y-axis [m]
z	Distance along z-axis [m]

Greek

θ	Slant angle
μ	Dynamic viscosity [kg/m·s]
ρ	Density [kg·m^{-3}]
σ	Standard deviation
φ	Angle at beginning of second groove
ω	Angle and end of first groove
φ	Angle at beginning of first groove

Subscripts

A	Micromixer A
avg	Average
B	Micromixer B
curve	Data obtained from curve

exp	Data obtained from experiment
i	i^{th} position
in	Inlet
m	Model
max	Maximum
min	Minimum
mix	Mixed
num	Data obtained numerically
obs	Occupied by obstructions
out	Outlet
p	Prototype
ref	Reference value
tot	Total

Dimensionless parameters

K	Dean number ($Re\sqrt{D_H/R}$)
Re	Reynolds number ($\rho \cdot U \cdot D_H/\mu$)
Sc	Schmidt number ($\mu/\rho \cdot D$)
Pe	Péclet number ($U \cdot D_H/D$)
x*	Equivalent length

Acronyms

a.u.	Arbitrary units
CFD	Computational fluid dynamics
CGM	Connected groove micromixer
CNC	Computer numerically controlled
DI	De-ionized
IF	Induced Fluorescence
LOC	Lab on Chip
MI	Mixing Index
MP	Mixing Parameter
SAR	Split and recombine
S.F.	Scaling factor
SGM	Slanted groove micromixer
SHM	Staggered herringbone micromixer
μ-PIV	Micro particle image velocimetry
μ-PTV	Micro particle tracking velocimetry
μ-TAS	Micro total analysis system

Chapter 1

Introduction

With the trend towards the miniaturization of devices in the biological, medical and chemical industries, the study of microfluidics and microfluidic components has attracted much attention over the past decade. Benefits associated with microscale fluidic devices include reduced sample consumption, reduced operation time, smaller footprint areas, and ease of integration into portable analysis systems. At the microscale, viscous forces and surface tension become important factors compared to inertia. As such, it is essential to develop an in depth understanding of fluid dynamics and transport phenomena at the microscale.

Micro-total analysis systems (μ-TAS) are comprised of numerous individual and interrelated elements, including micro-pumps, micro-valves, micro heat exchangers, micro-reactors, and micro-mixers. Each independent element is critical to the overall operation and performance of the μ-TAS, and must be studied extensively prior to implementation in a complete system. Micromixers are integral components in micro-total analysis systems, with applications in the fields of drug delivery, medical diagnosis, food engineering, and chemical and DNA analyses, amongst others (Jeong et al. 2010). In many such applications, it is essential to thoroughly and rapidly mix two or more species for a chemical reaction or homogenization to occur. Due to the small

characteristic dimensions of such devices, large pressure drops result. In practical applications, flow at the microscale is therefore supplied at low flow rates, which fall in the laminar regime. As a result, the turbulence applied to macroscale mixing is not feasible. It thus remains a challenge to effectively and thoroughly mix multiple species in microfluidic devices. To further develop μ-TAS for lab on a chip (LOC) applications, it is essential to develop micromixers with increased mixing efficiency, reduced pressure drop, and short mixing length and time. The study of microfluidics, namely the principles of mass transport at the microscale, is thus indispensible to the advancement and widespread implementation and production of microfluidic devices.

Flow visualization is a widely implemented and useful technique used to analyze liquid flow patterns. To analyze the distribution of species along micromixers, induced fluorescence (IF) has been employed by several research groups. This non-invasive optical technique allows for the qualitative and quantitative concentration distributions of species to be evaluated. From such information, the mixing efficiency may be assessed. Numerical simulations have been widely applied to the study of micromixers, and are indispensible when used to understand complex flow patterns which are not easily discernible by experiment alone.

The present study evaluates the species distribution and mixing efficiency of three passive scaled-up micromixers through use of flow visualization and induced fluorescence. When analyzing complex, three dimensional flow fields, numerical simulations are used as a tool of assistance.

Chapter 2 presents an extensive literature review of the state of the art in micromixing techniques, with a focus on passive micromixers. Chapter 3 presents the experimental facilities and techniques used in the investigation, including details of the induced fluorescence technique. The details of numerical analysis are also introduced. A novel comparison technique, which allows the mixing performance of devices of various scales to be reasonably compared, is also proposed. Chapter 4 presents the experimental evaluation of a parallel lamination micromixer with tear drop obstruction elements, while chapter 5 presents the experimental and numerical evaluation of a serpentine channel micromixer with slanted grooves. Based on the advantages of the aforementioned designs, chapter 6 presents the experimental and numerical study of a flow dividing micromixer with grooves and a multi-lamination inlet. Chapter 7 concludes the work and highlights goals for future improvements.

Chapter 2

Literature Review

While a definitive categorization for micromixers does not exist, micromixers have been broadly categorized as either passive or active (Nguyen and Wu 2005, Hessel et al. 2005, Aubin et al. 2010, Elmabruk et al. 2008). Active micromixers make use of external fields and forces to promote mixing, while passive micromixers take advantage of repeated variations in channel geometry to induce mixing. The aforementioned micromixer categories may be further divided based on operating principle, mixing mechanism, or geometry, although classification is left to the discretion of the author. While both gas and liquid mixing have been presented in the literature, the focus of this work is on liquid-liquid mixing. A review of recently developed micromixers and pioneering micro-mixing principles follows.

2.1 Active Micromixers

Active micromixers rely on time-dependent external disturbances to induce mixing. In general, active micromixers are able to achieve more thorough mixing than their passive counterparts due to the use of chaotic advection as the primary mixing mechanism. A wide variety of active mixing techniques have been investigated to date.

Moving components within a microchannel disturb the fluid interface and promote mixing. Hsiung et al. (2007), for example, experimentally and numerically

studied a micromixer based on pneumatically driven moving side walls, and reported a mixing efficiency of over 90%. Mixing was achieved as a result of the stretching and folding of the fluids in a significantly reduced channel diameter. To physically disturb fluids, the application of artificial cilia on microchannel walls was studied numerically (Khatavkar et al. 2007) and experimentally (Vilfan et al. 2010), where artificial cilia were placed in a magnetic field. Electrostatic attraction forces were used by den Toonder et al. (2008) to actuate artificial cilia and promote mixing.

Magneto-hydrodynamic disturbances have also been applied to promote vortex formation at the microscale (Affanni and Chiorboli 2010), however their application is limited to the use of electrolyte solutions (Nguyen and Wu 2005). The use of magnetic nanoparticles, or ferrofluids as a stirring mechanism has also emerged as a micromixing technique (Wen et al. 2009). Acoustic waves promote large disturbance forces and fast mixing by perturbing a fluid interface. This may be achieved by surface acoustic waves (Luong et al. 2011, Yeo and Friend 2009), or through use of oscillating trapped air bubbles (Ahmed et al. 2009 a,b). At frequencies of approximately 50 kHz, however, ultrasonic mixing may lead to temperature increase and possible cavitation - events which are highly damaging to biological samples (Lin et al. 2011, Nguyen and Wu 2005). Additionally, large shear gradients may arise along cell membranes at the low frequency operation typical of conventional acoustic driven micromixers, rendering these devices unsuitable for biological-based microfluidics (Yeo and Friend 2009).

Active micromixers typically require external power supplies and components, rendering them bulky, more costly, challenging to fabricate, and difficult to integrate into micro-total analysis systems. Additionally, effective operating ranges may be quite limited. For these reasons, passive micromixers, which make use of channel geometry to induce mixing, have been studied intensely.

2.2 Passive Micromixers

Passive micromixers may be divided based on a variety of mixing techniques and principles. While no strict standard exists for their further classification, several authors have categorized these passive devices based on the primary mixing mechanism, namely molecular diffusion or mass advection (Nguyen 2007).

At the microscale, a lack of turbulent flow renders traditional macroscale mixing techniques inapplicable. At the low Reynolds numbers employed in micromixing devices, diffusion remains an important mass transfer mechanism. Diffusive transport is dependent on the interfacial species area as well as the concentration gradient, and is governed by Fick's Law (Nguyen 2007)

$$j_{diff} = -D\frac{dC}{dy} \qquad (2.1)$$

where j_{diff} is the flux of diffusion, D is the diffusion coefficient, and dC/dy represents the concentration gradient of the species. As diffusive transport relies on molecular transport across a concentration gradient, it is typically a rather slow process. Various

micromixers operate on the principle of reducing lamellae width to enhance the interfacial area while reducing the path of diffusion.

Chaotic advection relies on the continuous stretching, folding and breaking-up of fluids caused by transverse flow. The mass flux resulting from advection, j_{conv}, may be represented as (Nguyen 2007):

$$j_{conv} = VC \qquad (2.2)$$

where V is the velocity vector and C is the concentration. It is worth noting that advection increases the interfacial area available for diffusion, and thus may reduce the path of diffusion. The balancing of mass fluxes is well known as the advection-diffusion equation.

As a given micromixer may be diffusion dominant or advection dominant depending of the range of operation, micromixers are further classified in this work based on their geometry.

2.2.1 Parallel Lamination Inlets

The most basic parallel lamination micromixers are those with simple T- and Y-inlets, where diffusion occurs along the interface of the two supplied species. Due to its elementary nature, this type of structure has been used as a reference for mixing performance comparison by many authors. As fast mixing in parallel lamination devices is achieved by increasing the species interface area and reducing the path of diffusion, species may be divided into multiple lamellae and combined prior to entering the main

channel, typically through interdigital inlets. The reduced characteristic widths of the lamellae allow for a reduction in diffusion path, and thus reduced mixing time. In traditional even lamella width mixers, *n* substreams theoretically allow the channel length to be reduced by a factor of n^2 (Nguyen 2007). An early introduction to multi-lamination mixers was given by Bessoth et al. (1999), who used distributive mixing to physically split fluids into multiple thinner striations, which were then re-arranged and recombined.

Hessel et al. (2003) experimentally investigated three interdigital inlet designs: rectangular, triangular and slit-shaped, as shown in figure 2.1. Each consisted of 2 × 15 feed microchannels with widths and depths of 60 μm and 150 μm, respectively. The rectangular mixer, which was unable to achieve sufficient mixing, was evaluated over Reynolds numbers ranging from 2 ≤ Re ≤ 341, corresponding to Péclet numbers ranging
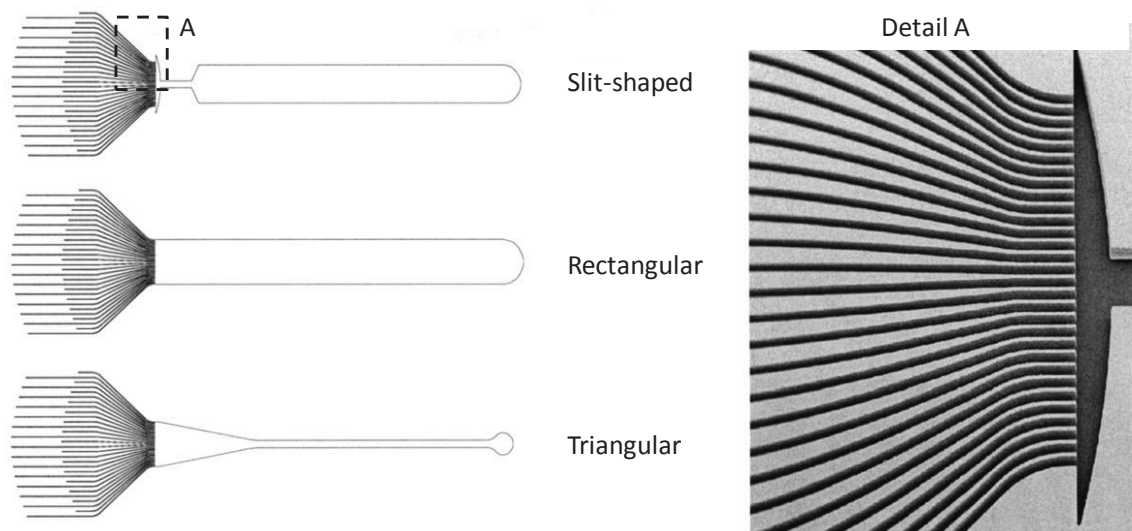
Figure 2.1: Sample of interdigital mixers (Hessel et al. 2003)

from 6.41×10^3 to 1.07×10^6. The triangular device resulted in more uniform concentration profiles compared to the rectangular mixer. This demonstrated the ability of the focusing structure to improve mixing by reducing lamella width. At Re ≥ 170 (Pe ≥ 5.34×10^5), the formation of additional lamellae was observed along the channel length; a definitive cause was not identified. Additionally, lamellae were found to be thicker in the center of the channel, and decrease in size toward the sidewalls. This was attributed to the orientation of the inlets (parallel) in comparison to the angled channel walls. It was concluded that lamella thickness is slightly dependent on channel geometry. The slit-shaped interdigital inlet, evaluated over 85 ≤ Re ≤ 1702.94 (2.67×10^5 ≤ Pe ≤ 5.34×10^6), led to recirculation zones and broken lamella after species were focused to reduce lamellae width. At higher flow rates, jet formation induced eddies in the expansion region of the mixer, leading to enhanced mixing compared to the previous two designs. Significant tilting of species interfaces was observed (Hardt and Schönfeld 2003). To further improve mixing, the SuperFocus design was developed, with a total of 124 microchannels and a focusing structure. A pressure drop of approximately 250 kPa was reported at a Reynolds number of 4427 (Pe = 1.39×10^7).

Further to their work, Löb et al. (2004) proposed a semi-analytical model to compare mixing in the rectangular, triangular and SuperFocus mixers. The SuperFocus allowed for lamellae of equal width to be created, as a result of its curved inlet structure. The mixing length and time of the SuperFocus mixer were reduced by several orders of magnitude compared to the rectangular mixer at 8 L/h (Re ≈ 4427).

Wu and Nguyen (2005) presented an analytical model for 2D convective-diffusive transport in parallel lamination micromixers, and concluded that the Péclet number was the most important parameter in parallel lamination micromixers; low Péclet numbers showed higher mixing efficiency. Cerbelli and Giona (2008) investigated the manner in which the degree of lamination affects mixing length for various flow profiles, and challenged the commonly accepted belief that the mixing length is approximately equal to the lamella thickness squared. The authors concluded that the mixing length is highly affected by flow profile, and that a general scaling between lamellae thickness and mixing length cannot be assumed.

Parallel lamination inlets have been shown to be effective mixers by significantly reducing the path of diffusion and increasing the area available for diffusion. Complex inlet structure and the requirement for precision alignment are drawbacks, however.

2.2.2 Split and Recombine

Alternate means to rapidly reduce the path of diffusion and increase the interfacial species area have been developed in the form of split and recombine (SAR) or serial lamination micromixers. These devices, which typically involve rather complex three dimensional structures, periodically divide species horizontally (or vertically) and recombine them vertically (or horizontally) to rapidly increase the number of striations, as shown in figure 2.2. Theoretically, the number of interfaces after the nth SAR unit increases from 1 to $2^{n+1} - 1$ (Xie et al. 2011).

Li et al. (2010b) proposed a split and recombine micromixer with 16 mixing units for fast mixing. The main channel width and height of their mixer measured 1 mm and 0.4 mm, respectively, while each mixing unit was 1 mm in length. Their device periodically divided species vertically, and rearranged them horizontally, to produce multiple striations. For each of the two fluids used, optimal mixing coefficients of 0.11 and 0.12 were reported at 100 µL/min (Re ≈ 2.4), where a value of 0 represents complete mixing. The design, however, had a drawback: flow tended towards the
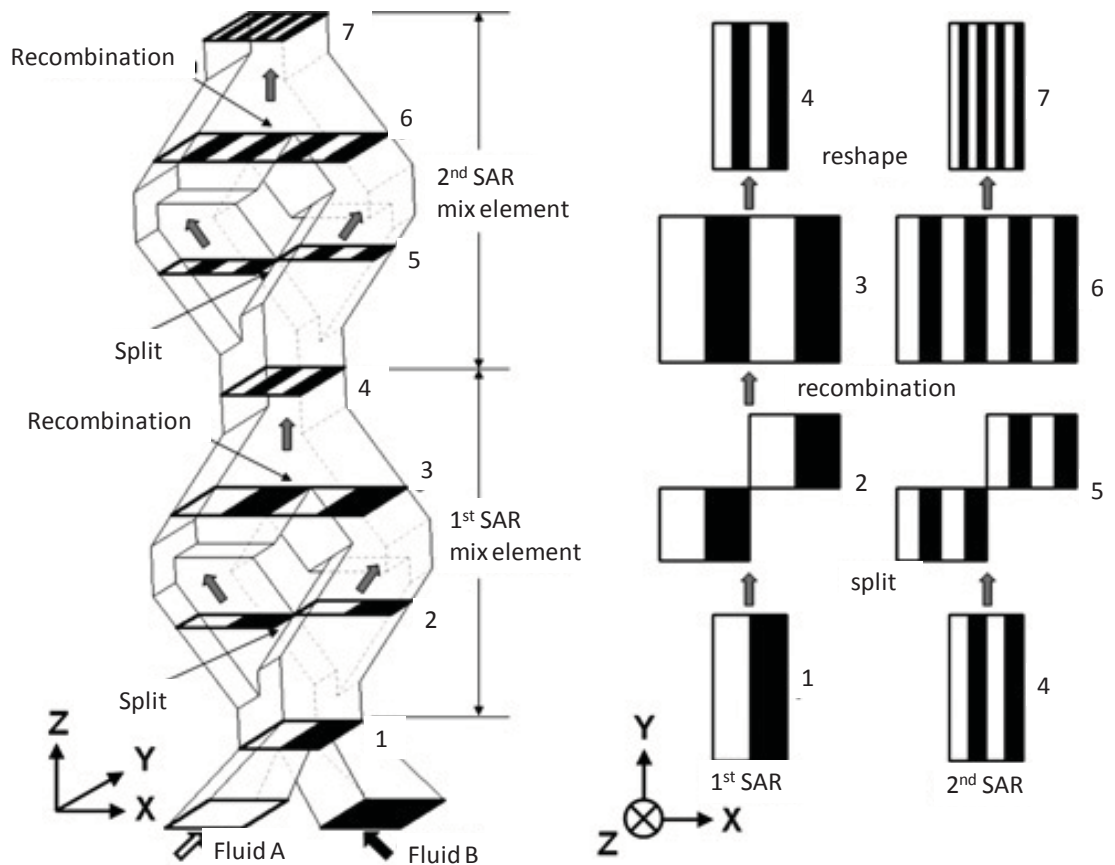
Figure 2.2: Demonstration of split and recombine principle (Xie et al. 2011)

channel with minimal resistance. As resistance was not equal on both sides of the mixer, sub flows did not contain equal amounts of each species, leading to uneven mixing. To improve the performance of their device, Li et al. (2010a) introduced a shim divider to force fluids to divide prior to entering sub channels. The resultant mixing efficiency parameter was 0.065 for both fluids – a marked improvement compared to the previous design.

To increase the interfacial species area, Xie et al. (2011) numerically optimized and experimentally investigated a 2-layer SAR micromixer with a cross section of 100 μm × 200 μm (width × height). Over $0.3 \leq Re \leq 3$, mixing increased with increasing branch angle, as did pressure drop. This was a result of chaotic advection caused by increased inertia. Using a viscous mixture of 95 % glycerol – 5 % water, complete mixing was achieved at $Re \approx 0.0053$ after 25 mixing elements, corresponding to a linear mixing length of 10 mm. Using 5 % glycerol – 95 % water, the mixing length ranged from ≈ 3 mm at $Re = 0.052$ to 7.6 mm at $Re = 3.09$. Owing to the fluid viscosity, lamination patterns are not as shown in figure 2.2. An increasing-decreasing trend in mixing length was observed with increasing Re, with an inflection point at $Re \approx 3.09$.

Lim et al. (2011) proposed a three-dimensional crossing manifold micromixer with sequential horizontally and vertically crossing tube bundles. The cross section measured 50 μm × 50 μm. Species were repeatedly spilt and recombined along the channel length to increase the number of striations. In their six-layer device, the degree of mixing increased rapidly along the channel length. The non-uniform momentum in

the channel caused the fluid layers to deform slightly, leading to increased surface area

and enhanced convection. Two species were divided in to 36 segments at a distance of

250 µm from the inlet, and 90% mixing was reported at Re = 1 (Pe = 10^3), with a

corresponding pressure drop of 970 Pa. At Pe = 10^2 and Pe = 10^4, 98% and 74% mixing

were reported, respectively.

While rapid lamination is achieved with SAR devices, they may be limited by

complex fabrication and the need for precision multi-layer bonding.

2.2.3 Bas-relief Structures

To generate transverse flows in micromixers, slanted bas-relief structures, or

grooves, have been placed along channel surfaces.   These structures create an

anisotropic pressure gradient; resistance to flow is lower along the direction of the

grooves than orthogonal to the structures. The resultant helical flow enhances mixing

by stretching and folding fluid over the cross section of the channel.

Stroock et al. (2002) experimentally investigated the effect of grooves and

herringbones on helical flow and mixing in a Y-inlet micromixer, as shown in figure 2.3.

They defined chaotic flow as the exponential stretching and folding of volumes of fluid

as a function of the axial distance travelled by the volume. The authors proposed a

design to achieve chaotic stirring at Re < 100 by creating transverse flows; slanted

groove structures at the base of the microchannel induced helical flow patterns. They

found the same qualitative patterns for Re < 100. Further to this design, the authors

investigated the staggered herringbone micromixer (SHM), which created two counter-

rotating vortices. The change in herringbone orientation changed the position of the centers of rotation. The efficiency of the SHM was controlled by the asymmetry of the herringbones, and the amplitude of the fluid rotation in each half cycle, which is in turn controlled by the geometry of the herringbones and the number of herringbones per half cycle. Symmetric herringbones showed non-chaotic flow structures. When the asymmetry parameter was set to 2/3, most of the cross sectional flow was chaotic. A groove angle of 45° with the flow direction was optimal. Once again for Re < 100, the flow patterns were qualitatively similar. The authors used fluorescence dye with confocal microscopy to evaluate mixing in an unobstructed, slanted ridges, and staggered herringbone Y-inlet micromixers. They found mixing was negligible in the simple mixer at high Pe (2×10^5), as well as in the slanted groove mixer. The SHM
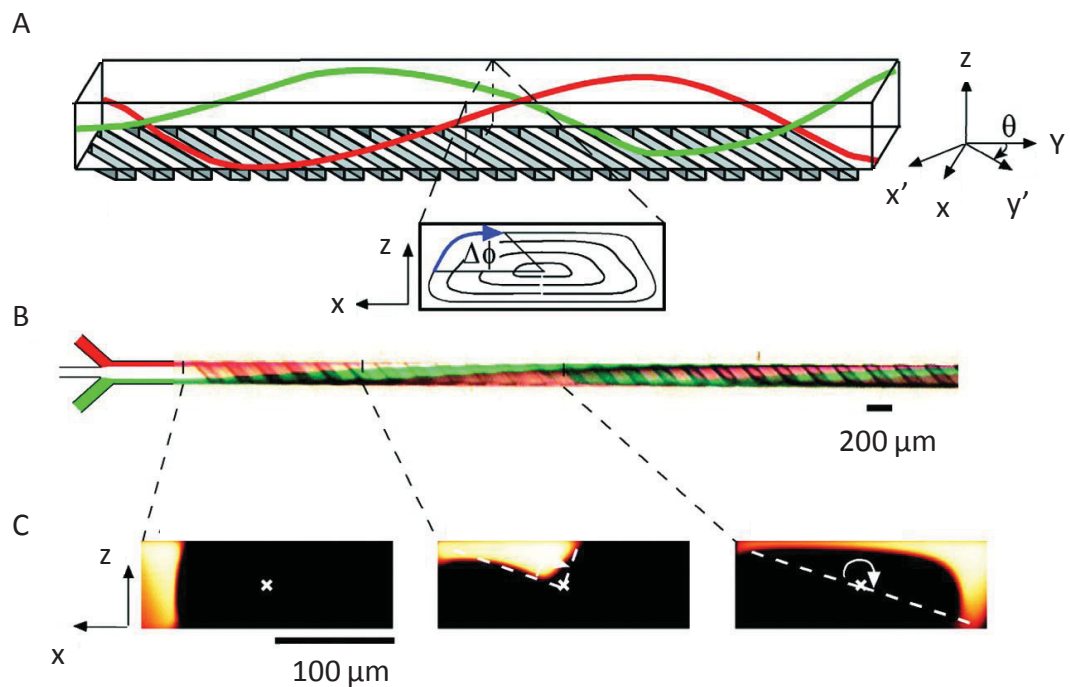
Figure 2.3: Demonstration of groove-induced rotation (Stroock et al. 2002)

demonstrated good mixing for a range of Pe numbers (up to 9 x 10^5). The number of

filaments increased and their thickness decreased as a function of the number of mixing

cycles. Ninety percent mixing was achieved at 0.7 cm for Pe = 2 x 10^3, and 1.7 cm for Pe

= 90 x 10^5. The 90 % mixing length increased linearly with ln(Pe) for large Pe.

Further to their work, several authors have focused on optimizing the geometric

parameters of groove-enhanced micromixers.   While general guidelines have been

established, it is important to note that each optimization is valid only for certain

operating conditions. A universal optimal layout has not been established.

Yang et al. (2005) numerically investigated the effect of a variety of geometric

parameters on fluid mixing in staggered herringbone micromixers at Re = 10 and Pe = 2

× 10^4. Mixing was significantly improved with increasing depth of groove, where small

vortical structures were observed in the vicinity of the grooves.   Asymmetric groove

lengths were favourable due to enhanced transportation capabilities; the longer arm

transported fluid from one side of the channel to the other. Additionally, the alteration

of asymmetric vortices, caused by asymmetric branches, provided a higher degree of

mixing.   Mixing due to the implementation of herringbones was a result of both

molecular diffusion and bulk advection. Vortical motion along the channel and within

the grooves stretched and folded the fluid interface.

Lynn and Dandy (2007) reported that flow directly above the grooves is viscously

affected by the flow contained within the groove, while flow over the ridges is viscously

affected by the recirculation above the ridges. This region appeared to hinder the non-

axial transport of the fluid in the direction of the grooves, reducing the total helicity of the flow. As such, the authors numerically investigated the effect of groove spacing on mixing in a slanted groove micromixer (SGM) at Re = 0.02, hypothesizing that a reduction in ridge width would increase helical flow and the degree of mixing. Decreasing the width of the ridges increased the magnitude of helical flow above the grooves by up to 50%. Additionally, the magnitude of helical flow increased with increasing groove depth ratio for ratios ranging from 0.09 to 2. Contrary to previous work, the authors found that the channel aspect ratio had a significant effect on helical flow. The authors stated that these observations may be extended to SHM devices.

Making use of reduced width ridges, Choudhary et al. (2010) numerically and experimentally investigated changes in the center of rotation along the transverse and longitudinal directions in four micromixers with varying arrangements of herringbone structures. Mixing was attributed to the production of counter-rotating vortices of varying sizes, with changing centers of rotation. The device with asymmetric herringbones on the top and bottom surfaces produced the highest average helicity and vorticity at Re ≤ 10.

Yang et al. (2008) modified the classic slanted groove mixer by introducing grooves along the sidewalls, in a device known as the connected-groove micromixer (CGM). Three devices were developed and compared to the basic SGM over 1 ≤ Re ≤ 100. The design with staggered slanted grooves and sidewall grooves outperformed all investigated devices, and showed over 50% greater mixing than the standard SGM over

the investigated Reynolds numbers. This improved design required a 10-15 mm channel length to obtain complete mixing, whereas the SGM required 30 mm.

Du et al. (2010) numerically simulated the SHM and SGM micromixers at Re = 0.3. In both mixers, increasing groove depth led to enhanced mixing – beyond a critical value, however, increasing groove depth was ineffective. Very deep grooves led to a large amount of fluid entering the grooves, where slow mixing became significant. Microchannel flow was hardly affected by the transverse flow with very narrow grooves. Excessively wide grooves, however, created dead zones in the microchannel volume. Mixing in the SGM was coarser and slower than that in the SHM, where two transverse vortices periodically altered locations. A hybrid mixer, containing both SGM and SHM portion, did not lead to mixing improvement.

Chen et al. (2011b) experimentally and numerically investigated a novel micromixer with a series of x-patterned slanted ridges on the top and bottom surfaces over $0.05 \leq Re \leq 50$. Their 750 μm wide, 90 μm deep, and 4 cm long mixer was based on the generation of lateral fluid motion to achieve chaotic advection. A decreasing-increasing trend in mixing efficiency was observed with increasing Reynolds number, with an inflection point at Re = 1. At Re ≤ 1, diffusion dominated. Flow crept through the ridges and the fluid interface was not distorted. At Re ≥ 1, secondary flow in combination with bulk flow along the channel axis distorted and stretched the interface, allowing for increased mass transfer.

Overall, several conclusions were typically agreed upon: 1) Staggered herringbone mixers provide superior mixing compared to slanted groove mixers. 2) Staggered herringbone mixers are optimized with asymmetric arms, where the width fraction of the long arm is approximately 2/3. 3) Typically, maximum non-axial flow occurs over a groove intersection angle of 45°. 4) The magnitude of helical flow is strongly dependent (asymptotically) on groove depth ratio. Controversy exists regarding the effect of channel aspect ratio on helical flow.

2.2.4 Curved Channels

The development of Dean vortices in curved microchannels has been shown to enhance mixing by increasing the interfacial species area. Fluid at the center of a channel has a higher velocity and centrifugal force than fluid at the sidewalls. As such, when fluid travels around a curve, the higher momentum fluid in the center of the channel is forced outward, while fluid at the outer wall is displaced in compensation, as shown in figure 2.4. A measure of the strength of the Dean vortices generated in a curved channel is given by the Dean number, K,

$$K = \text{Re} \sqrt{\frac{D_H}{R}} \tag{2.3}$$

where Re is the Reynolds number, D_H is the hydraulic diameter of the channel, and R is the mean radius of curvature of the channel.

Schönfeld and Hardt (2004) compared chaotic flow patterns observed in the staggered-herringbone mixer with those obtained in a curved channel. The authors

suggested that chaotic mixing may be produced by a simpler means, rather than applying grooved microstructures. They proposed that alternating flows may be achieved by changing the sign of curvature of the channels, in the form of a meandering channel. This was proposed beyond a critical Dean number ($\approx$ 200), where four vortices were observed.

Howell et al. (2004) experimentally investigated a square cross-section curved channel which enhanced lateral instabilities in the flow, generating a secondary cross channel flow. At Re = 3, mixing was a result of diffusion, and at Re = 10, species were vertically stacked. At higher Reynolds numbers (Re =16, 30) the formation of vortices was noted. The authors found that the magnitude of the secondary flow was inversely proportional to the radius of curvature. Additionally, deeper channels were found to be more effective mixers. At higher flow rates, the authors believed whorls formed parallel to the axis of the channel.
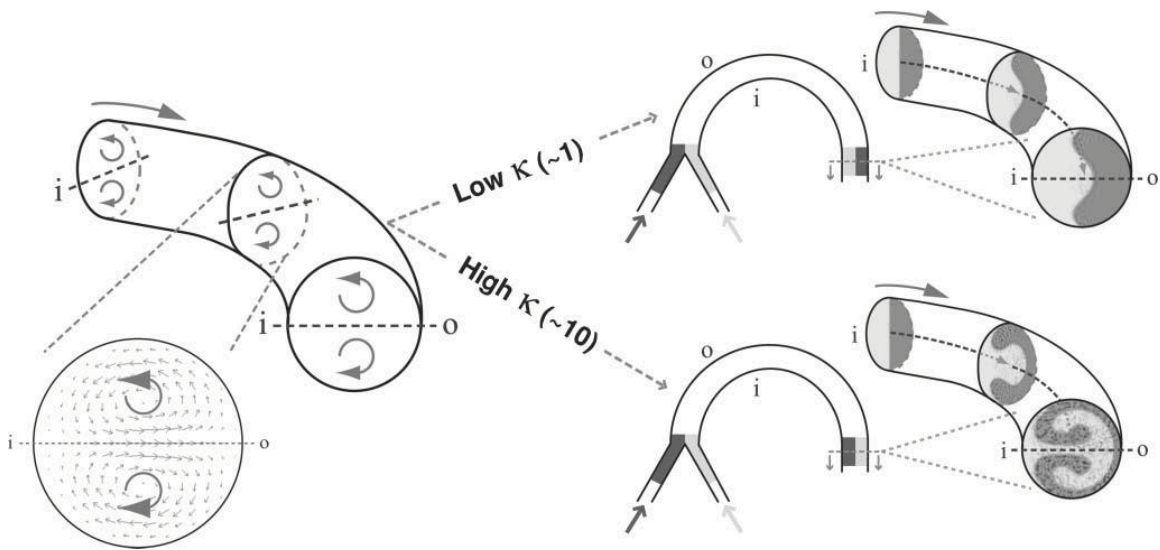
Figure 2.4: Dean vortex formation in a curved channel (Sudarsan and Ugaz 2006)

Jiang et al. (2004) numerically and experimentally investigated a curved rectangular cross-section microchannel with 4 meandering elements. The hydraulic diameter was 200 μm and the radius of channel curvature was 1000 μm. Exponential interface growth indicated chaotic mixing at high Dean numbers, although the mechanism of chaotic mixing differed from K = 100 to K = 200. At lower Dean numbers (K = 10), helical flow was weak and the center of rotation was located close to the center of the channel; two counter rotating vortices were observed in the entire channel cross section. As the Dean number increased, the helical flow became stronger and the center of rotation moved toward the outer channel wall (K = 100). Above a critical Dean number, K ≈ 150, a qualitative change in flow pattern occurred: additional counter rotating vortices formed close to the outer channel wall, creating a total of 4 vortices in the channel cross section. With increasing K, the helical rotation was increased, the centers of rotation were shifted, and, due to increased asymmetry, mixing was enhanced from one curved segment to the next.

Modifying the traditional curved channel, Sudarsan and Ugaz (2006) experimentally investigated the mixing efficiency of spiral microchannels, with a width and height of 150 μm and 29 μm, respectively, over 0.02 ≤ Re ≤ 18.6. The strength of the secondary flow increased as the species travelled from the outer to the inner portion of the spiral due to the decrease in radius of curvature. At low Dean numbers, the secondary flow was too weak to perturb the flow, and hence mixing was diffusion dominant. Increasing flow rates (Re = 10) led to enhanced secondary flow and thus enhanced mixing. At the lowest flow rate, (Re = 0.02) 80% mixing was achieved after a

length of 19 mm. At the highest flow rate (Re = 18.6), 90% mixing was achieved at the same length. The mixing length became shorter with increasing Reynolds number due to the enhancement of secondary flow.

Chen et al. (2011a) proposed a micromixer based on the generation of Dean vortices in staggered curved channels over $0.5 \leq Re \leq 50$ ($0.22 \leq K \leq 22.36$, $1.25 \times 10^3 \leq Pe \leq 1.25 \times 10^5$). Their device generated counter-rotating vortices in the curved channel, and periodically divided and recombined fluids through curved sub-channels. At $Re \leq 1$, mixing was diffusion dominant, and the degree of mixing decreased with increasing Reynolds number. Beyond Re = 10, secondary flow was observed, and mixing increased with increasing Re, as a result of increased Dean vortices and stronger species impingement. Approximately 90% mixing was observed after 22 mixing elements.

Curved channels allow for the formation of chaotic advection through Dean vortex generation, while offering the benefits of simple planar fabrication. Two counter-rotating vortices characterize Dean vortices. To achieve four counter-rotating vortices and take advantage of increased interfacial area, relatively high Dean numbers, beyond $K \approx 140$, are required.

2.2.5 Obstruction Filled Channels

To repeatedly and periodically break up flow, increase species interfacial area, and reduce the path of diffusion, several researchers have implemented obstructions of various geometries along the micromixer length. Obstructions not only increase the interfacial area, promoting diffusion, but may generate vortices and encourage

transversal flow, promoting chaotic advection. Figure 2.5 shows a sample of an obstruction-filled channel.

Hong et al. (2004) evaluated a micromixer with modified Tesla structures over 1 to 100 μL/min (Re < 100). The mixer was dependent on transverse dispersion at the end of each mixing cell to promote mixing as a result of impacting sub-flows. The mixing performance showed patterns similar to Taylor dispersion, where convection and diffusion are important. A decreasing-increasing trend in the degree of mixing was observed with increasing flow rate.

To promote transverse fluid flow, Bhagat and Papautsky (2008) evaluated fluid mixing and particle mixing in a planar micromixer with 45° angled rectangular obstructions at Re = 0.05 (Pe = 300). Compared to the Tesla mixer of Hong et al. and the Y-mixer, their design achieved superior particle mixing, though fluid mixing performance was similar to that of the Tesla structure.

Also promoting transverse flow, Lin et al. (2007) numerically and experimentally investigated J baffles in a T-inlet mixer over 5 ≤ Re ≤ 350. The baffles forced fluid is a direction perpendicular to the channel axis, promoting enhanced mixing. Although mixing was higher at higher Re, the increase in mixing, compared to a straight channel, was more noticeable at lower Re. Over 80% mixing was obtained after the 14th baffle at Re = 350.

Bhagat et al. (2007) numerically evaluated obstructions of various geometries at
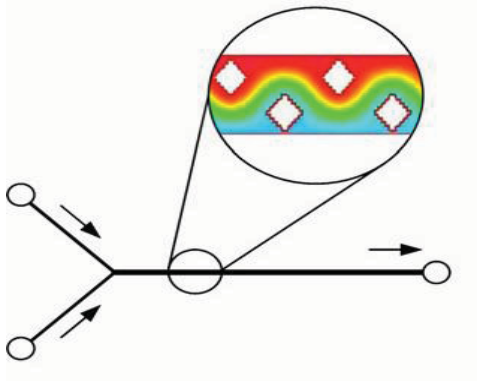
Figure 2.5: Obstruction placed along channel length (Bhagat et al. 2007)
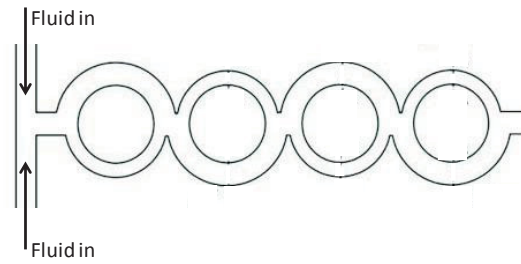
Figure 2.6: Large flow diving structures (Ansari et al. 2010)

Re = 0.1. Circular, triangular, smooth diamond, and stepped diamond obstacles were compared. Circular obstructions produced the worst mixing (40%), followed by diamond (44%), triangular (56%) and stepped diamond (77%). Dead volumes generated by triangular elements, however, rendered them undesirable. Experimental evaluations of a Y-inlet mixer with a 1 × 1 repetitive pattern of shaped diamond obstructions showed a decreasing-increasing trend in mixing efficiency with increasing Reynolds numbers over 0.02 ≤ Re ≤ 10, with an inflection point at Re = 1.

Following their work, Hsieh and Yang (2009) numerically investigated the effect of rectangular protrusions on the side walls of a diamond shaped obstruction-filled channel. Compared to channels without protrusions, the rectangular protrusions increased mixing index from 0.38 to 0.97, with a value of 1 representing complete mixing. The mixing index exhibited a decreasing trend from Re = 0.1 to 1, and an increasing trend from Re = 10 to 100, due to the change in mixing mechanism from

diffusion dominance to convection dominance. Higher vorticity values were seen at the corners of the obstructions and boundary protrusions due to flow separation.   Vortices in opposite directions induced secondary flow, allowing for efficient mixing due to vortex agitation. Protrusions increased the magnitude of the vortices and enhanced fluid stretching. Obstacles broke up flow and induced velocity in the transverse direction, while sidewall protrusions facilitated stirring in that region.

Extending their work, Tseng et al. (2011) numerically investigated the effect of the shape, width and length of boundary protrusions on mixing efficiency in a diamond-obstruction filled mixer over 0.01 ≤ Re ≤ 100. The authors observed elevated vorticity values around the corners of the obstacles and protrusions, leading to increased mixing from vortex agitation. The addition of protrusions led to an increase in stream-wise flow velocity, and hence increased centrifugal force and increased secondary flow. A comparison of square, elliptical and triangular protrusions showed that square protrusions provided the highest degree of mixing. The effect of protrusion length on mixing was rather insignificant. Micromixers with larger protrusion width worked best at higher Re.

Obstructions have also been placed in shaped channels. Nguyen et al. (2008) experimentally investigated the mixing efficiency of a micromixer with square obstructions in a square-wave channel with a modified Y-junction inlet over 5.5 ≤ Re ≤ 56. They found that mixing was improved due to vortex formation at the square obstacle region, especially at the entrances with smaller dimensions due to sudden

cross sectional area changes. Mixing time was also less due to the reduction in diffusion length. Lateral molecular diffusion was observed, and vortices were generated as the fluids collided at the square obstructions. The mixing rate increased with increasing flow rate due to the increase in vortex formation. Large vortices formed in the secondary flow due to an abrupt change in cross sectional area.

The application of obstructions along a channel length provides a variety of means to enhance mixing. Flow may be guided in a transverse direction, promoting Taylor dispersion, it may be focused to reduce the path of diffusion, and the generation of vortices and secondary flow may also occur at higher flow rates.

2.2.6 Flow Dividing Structures

Large structures of various shapes placed along the channel length repeatedly divide flow into two substreams, which are then recombined into the main channel, as shown in figure 2.6.

Chung and Shih (2008) proposed and investigated a three-inlet three-rhombus micromixer with a converging-diverging structure over $5 \leq Re \leq 200$. Smaller turning angles, higher Reynolds number and increased number of rhombic elements increased the degree of mixing as a result of increased recirculation. Molecular diffusion was dominant for $Re < 10$ whereas at $Re > 10$, recirculation was responsible for enhanced mixing. Inertial effects and pressure gradients caused recirculation at the angled portions of the mixer. A mixing efficiency of 94 % was reported with a corresponding pressure drop of 5693 Pa at $Re = 200$ for a 30° turning angle. To promote asymmetric

flow and increase inertial effects over 1 ≤ Re ≤ 50, Chung and Shih (2007) applied two constriction elements to the symmetric design with a 90° turning angle. The constriction elements and bends induced focusing/diverging effects, recirculation and Dean vortices, while the double zigzag channels split and recombined the flow. Fluidic mixing was found to be related to the blockage ratio of the constriction elements and Reynolds number. Mixing efficiency increased with decreasing blockage ratio and increasing Reynolds number. At Re = 50, mixing efficiencies of 33.6% and 93% were reported for the devices without and with constriction elements, respectively. A higher pressure drop of 8036 Pa at Re = 20 was reported in the constricted device.

Further to their work, Chang et al. (2011) numerically and experimentally investigated a rhombic micromixer with branch channels. The mixer with branches outperformed the basic rhombic mixer in terms of mixing as a result of the increased vortex generation near the branch junctions beyond Re = 10. Over 90 % mixing was achieved at Re ≥ 80 and 98 % at Re = 120. The pressure drop was less than 9 kPa at Re = 120.

Fan and Hassan (2010) also took advantage of 90° bends in channel geometry to induce vortices and enhance mixing in a scaled up micromixer. Their scaled-up cross-omega mixer was evaluated over 1 ≤ Re ≤ 50 numerically and experimentally, and exhibited a decreasing-increasing trend with increasing Re with a minimum at Re = 10, as a result of the dominant mixing mechanism changing from mass diffusion to mass-

convection. Induced fluorescence data showed approximately 70 % mixing after five mixing units at Re = 50.

Ansari et al. (2010) numerically and experimentally investigated the mixing performance of a passive micromixer with curved sub-channels of uneven width over 10 ≤ Re ≤ 80 using water and ethanol. The difference in inertial forces between the two streams created an unbalanced collision, perturbing the fluid interface due to transverse flows. The degree of mixing increased with increasing collision imbalance at higher Reynolds numbers. Ansari and Kim (2010) then numerically investigated the effect of unbalanced channel widths in rhombic sub-channels over 1 ≤ Re ≤ 80. For Re ≤ 20, where diffusion dominates, the mixing performance decreased with increasing Re. Inertial forces were not sufficient to create transverse flow. Beyond Re = 20, mixing increased with increasing Reynolds number. Overall, the circular channel device showed better performance than the rhombic device at Re > 20 as a result of the Dean vortices in the curved channel. At Re = 1 and 20, both devices showed approximately 20% and 15% mixing, respectively. At Re = 80, the circular and rhombic devices showed approximately 57% and 51% mixing, respectively.

Lu et al. (2010) numerically and experimentally investigated the mixing efficiency and mixing time of a passive micromixer with two tee inlets and four butterfly-shaped mixing elements over 8 ≤ Re ≤ 48, as calculated based on the inlet dimensions. It was found that at low Re, mixing was dominated by viscous forces, and mixing was not well completed. As the Reynolds number increased (Re = 16), obvious fluid interface

distortions were seen in the mixing elements, and transverse fluid motion became important, especially at the walls. Beyond Re = 24.1, helical rotation was observed, and transverse flows stirred the fluid rapidly, such that interface area and efficiency were increased. At higher Reynolds numbers, inertial forces were dominant compared to viscous forces, and mixing was enhanced. Complete mixing was observed at the mixer outlet at the highest flow rate; vortex formation was found to be the primary mixing mechanism. The degree of mixing ranged from 26 % to 99 % at the outlet.

2.2.7 Combination Mixers

To combine the benefits associated with various mixing techniques and geometric configurations, several authors have proposed combination micromixers.

To take advantage of the increase in interfacial area resultant from the formation of Dean vortices, curved channels have been integrated into several designs. Mouza et al. (2008) experimentally investigated a meandering curved microchannel with circular division elements and 14 repetition structures to generate alternating Dean vortices over $20 \leq \text{Re} \leq 350$. Curved channels resulted in the fluid interface moving from the center to the outer wall, while the intermediate dividing structures broke the symmetry on the secondary flow. At lower Dean numbers ($K = 8$) secondary flow was very weak; alternating channel curvature merely returned the species interface to its original position. At higher K, stronger transverse flow caused the species at the outer wall to be transported to the inner wall within the first mixing element, and chaotic advection was reported at K > 140. Mixing time decreased dramatically with an increase

in Dean number up to the critical Dean number. Beyond this point, the formation of two additional vortices was credited with enhanced mixing.

Tsai and Wu (2011) also implemented modifications to a serpentine channel by adding radial baffles. The device was investigated over $0.054 \leq Re \leq 81$. The addition of baffles to curved channels improved the degree of mixing by increasing the interfacial area while Dean vortices improved mixing, especially at high Re and lower radius of curvature. The position of baffles greatly affected the degree of mixing as a result of lateral convection and the generation of vortices behind the baffles, which were observed at $Re \geq 27$. A decreasing-increasing trend in mixing efficiency was observed with increasing Re, with an inflection point at $Re = 3$. At $Re = 81$, greater than 90% mixing was achieved, and a separation vortex was noted downstream of the second baffle. At $Re = 0.054$, a high degree of mixing (M > 95%) was reported due to the increased residence time allowing for pure diffusion.

To enhance helical flow in curved channels, bas-relief structures have been introduced. Hu et al. (2006) investigated the mixing of water and acetone in a 200 μm × 100 μm (w × d) curved channel micromixer with herringbone grooves. Outlet mixing efficiency varied from 90 - 98 % over $1 \leq Re \leq 10$. Tan et al. (2008) investigated a long LOC-integrated micromixer with staggered herringbone structures in the straight portion of a meandering channel for medical diagnostic purposes. The direction of secondary flow was periodically reversed to enhance folding along the channel length.

Chen et al. (2009) experimentally investigated the mixing efficiency of a curved-channel passive micromixer with four high-density cylindrical obstruction clusters at low flow-rates 0.1 - 10 μL/min. The channel was 200 μm wide and 45 μm deep, while the total length was taken as 35 mm. Mixing efficiency was best at low flow rates, and decreased with increasing flow rate. The splitting and recombining of the flow due to the pillar obstructions increased the interface area, causing a reduction in the path of diffusion.

Adeosun and Lawal (2009) experimentally and numerically investigated the mixing efficiency a micromixer which applied a multi-lamination technique at the inlet, where eight substreams were introduced to the mixing channel. Isosceles trapezoidal structures were placed within the mixer channel to increase the contact area. Tested Reynolds numbers, based on outlet cross sectional area, ranged from 5.1 to 12.8. Mixing improved at lower Reynolds as a result of the longer residence time.

Tofteberg et al. (2010) combined the concepts of inducing chaotic advection via slanted grooves and serial lamination in a passive four-module micromixer. After slanted grooves created controlled 90° fluid rotation, species were divided, rotated, and recombined to double the number of lamellae in each module. In a 300 μm x 50 μm (width x height) channel, the optimum values, of those tested, were found to be a groove angle of 55°, groove depth of 50 μm, and a groove width of 200 μm. After 4 rotating cycles (modules) at Re = 5, approximately 90 % mixing was achieved. For Re < 5, the lamination process was unchanged, and in the Stokes flow regime, almost perfect

lamination was observed. With increasing momentum effect, the helical flow pattern changed, and lamination was no longer ideal.

2.3 Mixing Evaluation Techniques

While both single phase and two-phase mixing have been reported in the literature, liquid-liquid mixing is the focus of this work. Both experimental and numerical techniques have been widely applied to assess the flow patterns and mixing performance of micromixers. Each evaluation methodology offers unique benefits and is limited by disadvantages.

Aubin et al. (2010) provided a comprehensive review of micro-mixing principles, and detail experimental evaluation techniques. To determine concentration distribution, dilution-based methods, which include the use of coloured dyes, fluorescence species, and chemical based reactions, have been widely applied. As concentration distribution and mixing performance are a result of flow fields within the micromixer, a variety of techniques have been employed to assess flow patterns, including micro particle image velocimetry (μ-PIV) and micro particle tracking velocimetry (μ-PTV). Commonly applied optical based measurement techniques are limited by a number of factors, including image resolution, plane of measurement, direction of view, reflections, and the necessity of a transparent device. Experimental work is also subject to uncertainty resulting from equipment used. Several researchers made use of commercial software to analyze single-phase liquid mixing and flow patterns via computation fluid dynamics (CFD). The accuracy of numerical work,

however, is limited by numerical diffusion. Hardt and Schönfeld (2003) proposed measures to reduce its effect, such as decreasing the grid size and applying a higher order solving scheme.

To thoroughly analyze mass transfer in micromixers, a combination of experimental and numerical work is indispensible.

2.4 Summary and Motivation

The demand for disposable LOCs for applications in the biomedical and chemical industries has increased dramatically over recent years. As an essential component of LOC platforms, micromixers have emerged at the forefront of promising research areas. Due to the low Reynolds numbers and small channel diameters employed, it remains a challenge to effectively mix liquids at the microscale. Innovative micromixers, which offer high mixing performance, low pressure drop, short mixing length, and ease of integration, are necessary.

Active and passive micromixers have been proposed and studied in the literature. While active micromixers typically offer high mixing efficiency and rapid mixing, challenges involving system integration and control, complex fabrication, and higher production costs have been presented. As a result, passive micromixers, which make use of channel geometry to induce mixing, have been deemed preferable by numerous researchers.

A variety of geometric variations have been proposed to enhance the performance of passive micromixers, which operate at low Reynolds numbers where traditional turbulent mixing techniques are inapplicable. Amongst designs, a common goal exists: to improve mixing by increasing the interfacial species area and reducing the path of diffusion, as well as creating transverse flow. Good mixing should be achieved rapidly and in a small footprint area. Additionally, low pressure drop is desirable, such that regions of extreme constriction and sharp angles should be avoided. In practical applications, micromixers are typically fabricated via lithography. Designs with minimal complexity, allowing for easier fabrication, are therefore desired.

2.5 Objectives

The principle of operation, design, fabrication, experimental testing and numerical simulation of three novel passive micromixers are discussed in this work. The following outlines the goals of the current work:

- Design and evaluate novel scaled-up micromixers which operate over a wide range of Reynolds numbers. Two-dye flow visualization is used to qualitatively assess flow patterns and mixing performance, while induced fluorescence (IF) is used to provide quantitative whole-field concentration distribution data. Numerical simulations are applied to assess the complex flow patterns of two mixers.

- Experimentally evaluate the performance of the "Parallel Lamination Micromixer with Tear Drop Obstructions". This mixer uses a seven-lamellae uneven

interdigital inlet to reduce the path of diffusion and increase the interfacial species area. Tear-drop obstructions periodically reduce the path of diffusion and increase interfacial area, while promoting the formation of Dean vortices at higher Reynolds numbers. Sidewall mixing is encouraged through the application of obstructions on the sidewalls and reduced lamellae thickness.

- Experimentally and numerically evaluate the "Groove-Enhanced Serpentine Micromixer". This Y-inlet serpentine mixer with four semi-circular portions contains slanted grooves along the channel base to promote helical flow. The curved channel promotes Dean vortices at higher Re.

- Based on the results of the previous two mixers, the "Mixer with Groove-Enhanced Division Elements" is designed and evaluated experimentally and numerically. The device uses a simple three-lamellae parallel lamination inlet to reduce the path of diffusion and increase interfacial area. Grooves on the base of five circular division elements promote flow rotation at all Re, while Dean vortices develop at higher Re.

- Propose a comparison technique allowing for mixers of various sizes to be reasonably compared.

Chapter 3

Micromixer Evaluation: Experimental and

Numerical Techniques

To assess the performance of micromixers with various geometries, three novel scaled up passive micromixers are experimentally evaluated through flow visualization and micro-induced fluorescence. Flow visualization is used to assess flow patterns and provide qualitative mixing efficiency information along the channel lengths, while induced fluorescence is used to obtain quantitative whole-field concentration distribution information. Numerical simulations are applied to complement experimental work for two mixers which involve complex three dimensional flow patterns. A quantitative means to assess mixing performance is discussed, and a technique to allow for reasonable comparison between micromixers of different scales is proposed.

3.1 Similarity

To reduce manufacturing costs and allow for ease of experimental manipulation, scaled up micromixers were designed and fabricated. The applicability of using scaled-up test sections for micro-scale investigations has previously been validated experimentally and numerically (Xia 2009, Fan and Hassan 2010). Xia (2009) fabricated meso and micro-scale mixers based on chaotic mixing and sequential lamination and

reported consistent observations between the devices. To demonstrate the validity of a scaled-up test section for micro-scale investigations, both dimensional and geometric similarity must be achieved. Geometric similarity between the model (m), and the prototype (p) is conserved when

$$\left.\frac{D_H}{L}\right|_m = \left.\frac{D_H}{L}\right|_p \tag{3.1}$$

$$\left.\frac{H}{L}\right|_m = \left.\frac{H}{L}\right|_p \tag{3.2}$$

$$\left.\frac{W}{L}\right|_m = \left.\frac{W}{L}\right|_p \tag{3.3}$$

where H, and W represent the channel height and width, respectively, at any given location along the channel length, L.

Two mechanisms are responsible for mixing: mass advection and mass diffusion. Therefore, velocity and concentration are critical parameters. Two dimensionless parameters, the Reynolds number and Péclet number, are thus used to preserve dynamic similarity. The Reynolds number

$$Re = \frac{\rho U D_H}{\mu} \tag{3.4}$$

represents the ratio of inertial to viscous forces, where ρ is the density, U is the mean velocity and μ is the viscosity. The Péclet number,

$$Pe = \frac{UD_H}{D} \qquad (3.5)$$

is the ratio of the rate of advection to the rate of diffusion. According to equations (3.4) and (3.5), and assuming fluids with the same properties are used in the model and prototype, maintaining the Reynolds number between the model and prototype allows for the Péclet number to be conserved, thus preserving dynamic similarity.

3.2 Experimental Evaluation

3.2.1 Fabrication Basics

To allow for ease of experimental manipulation and reduced fabrication costs, scaled up micromixers have been produced. All three designs were machined in cast acrylic using conventional micro computer numerically controlled (CNC) machining. Although similar manufacturing procedures were followed for all devices, slight modifications were carried out in terms of bonding and sealing the devices. Particular details pertaining to each of the three designs are addressed in their respective chapters.

3.2.2 Experimental Facilities

Figure 3.1 shows the facilities used for both flow visualization and induced fluorescence measurements. For both flow visualization and IF investigations, two syringe pumps (New Era Pump Systems Inc., model NE-1010), equipped with 60 mL capacity syringes (BD company) were digitally set to the required flow rates. With this

Figure 3.1: Experimental facilities used for flow visualization and IF measurements

size syringe, the maximum and minimum flow rates are 7635 mL/hr and 58.26 µL/hr, respectively, with a dispensing accuracy of ± 1 %. Species were supplied to the inlets of the test section through flexible tubing (Tygon tubing, 1/8 inch inner diameter) attached

to the test sections via threaded barbed fittings. For flow visualization experiments, these species were de-ionized (DI) water mixed with food colour, whereas for IF experiments, these fluids were de-ionized water and a solution of de-ionized water and Rhodamine 6G (Sigma-Aldrich). Waste solutions were directed to a reservoir for safe disposal. For flow visualization experiments, a colour 3CCD camera (Sony CDX-9000) captured images at various positions along the test section. A light ring supplied uniform lighting above the test section to reduce the occurrence of shadows and provide higher quality images. For induced fluorescence measurements, the test section was positioned on and secured to a microscope stage (Nikon Eclipse TE2000-S). A mercury lamp (Chiu Technical Corporation, Mercury 100 W) supplied continuous light through either a 2 × or 4 × magnification objective lens to the test section. Emission light from the test section was directed through an Epi-fluorescence filter (Chroma Technology), which filtered out the excitation light from the laser (considered to be *noise)*, and allowed only the re-emitted light to be captured by the detector and CCD camera (Dantec Dynamics - HiSense MkII). Images were processed on a Dell Precision Workstation (two 3.60 GHz Intel Xeon processors, 4 GB of RAM, two 250 GB 7200 rpm hard disks and 128 MB video card). A frame grabber card (NI-IMAQ PCI-1426) was used to record the images from the camera, which was controlled through the computer by a synchronization unit. Images were processed using Flow Manager Software v4.50.

3.2.3 Flow Visualization

To visualize flow patterns and qualitatively assess mixing along the channel length, solutions of food colour and DI water were prepared for flow visualization

experiments. Several trials showed that both red and green or red and blue solutions showed good contrast. Two colours were used to allow for species to be more easily distinguishable; using water with a single colour solution did not permit mixing to be as easily visualized. For all investigated test sections, a syringe filled with fluid and tapped free of any air bubbles was attached to each inlet via flexible tubing and barbed fittings. Syringes were slowly pressed to fill the channels of the test sections. The larger-scale mixer investigated in chapter 4 was filled manually, and rotated and adjusted as needed during the filling process to ensure no air bubbles were trapped in the device. The smaller-scale mixers of chapter 5 and 6 were filled using the syringe pumps at low flow rates. Once filled, the test sections were carefully placed beneath the camera with uniform lighting. It was essential to avoid abrupt motion with the filled test sections to prevent the formation of bubbles. Syringe pumps were set to the desired flow rates, based on the two-fluid inlet Reynolds number, and started simultaneously. Images were then taken at a rate of 30 frames/s at various locations along the test sections. After completing flow visualization, areas of interest were identified for further investigation using induced fluorescence.

3.2.4 Induced Fluorescence

3.2.4.1 Principle of Operation

Induced fluorescence is a non-intrusive, optical technique used to obtain qualitative and quantitative concentration and temperature distribution data. In this

work, Rhodamine 6G, a concentration dependent and temperature-independent dye, is used to evaluate species distribution.

Fluorescence results from a three-stage process that occurs in fluorophores, as shown in the electronic-state, or Jablonski, diagram in figure 3.2a. In its ground state, a fluorophore has a relatively low energy level. Upon absorbing light energy (stage 1), it becomes excited to a higher vibration energy level; excitation lasts approximately 10^{-15} seconds. As the fluorophore is unstable at high energy levels, it quickly relaxes to a lower energy level, in an event known as vibrational relaxation (stage 2). This typically lasts $10^{-14} - 10^{-11}$ seconds. To once again become stable, the fluorophore releases excess energy as emitted light and drops to the ground state (stage 3) in a process known as fluorescence, which lasts approximately $10^{-9} - 10^{-7}$ seconds (Johnson and Davidson). At its ground state, the fluorophore may now absorb light energy and repeatedly undergo the excitation-emission process.

The number of excited fluorophores is related to the wavelength of the excited light. There exists a wavelength, known as the peak excitation wavelength, at which the proportion of excited fluorophores is maximal. At shorter or longer wavelengths, a smaller proportion of fluorophores absorb energy. A similar phenomenon occurs during emission, or the loss of energy, where a peak emission wavelength exists. This is shown in figure 3.2b. According to Planck's law, the energy of an absorbed photon is inversely proportional to the wavelength. As such, the emitted light has a longer wavelength and lower energy than the absorbed light. The peak excitation and emission wavelengths of
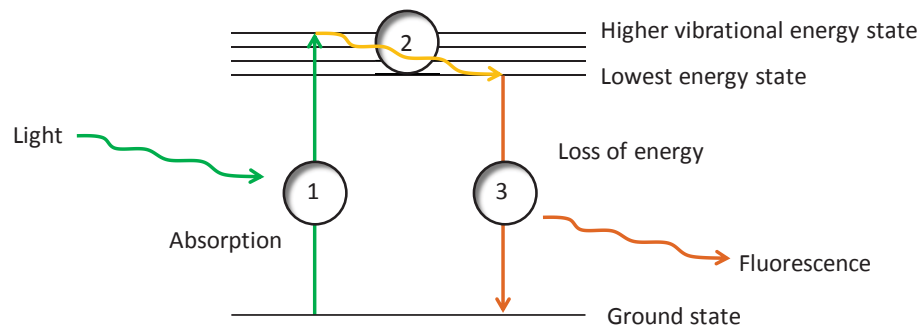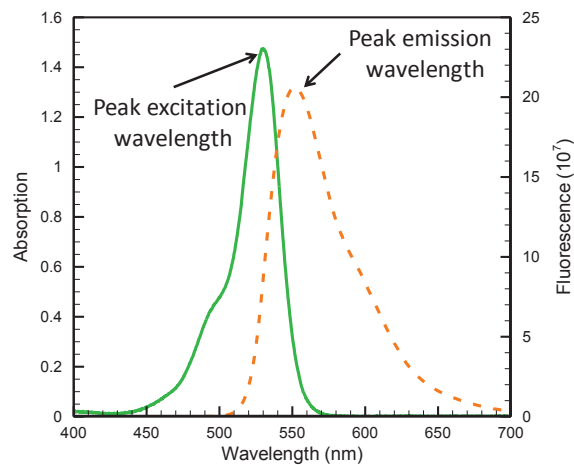
Figure 3.2: a) Jablonski diagram showing excitation-emission process b) excitation and emission spectra of Rhodamine 6G c) visible light spectrum.

Rhodamine 6G are 526 nm and 555 nm, respectively (Abramowitz and Davidson). The difference in peak wavelength is known as the Stokes shift. As a result of their differing wavelengths, absorption and emission light appear as different colours, as shown in the visible light spectrum in figure 3.2c. This difference in excitation and emission spectra allows for the excitation light to be filtered, and fluorescence light to be captured. It is important to ensure that the excitation and emission spectra do not have overlapping

42

peak wavelengths, as this would lead to self-quenching, a phenomena whereby re-emitted fluorescence is re-excited by the excitation light. It is additionally important to select an appropriate light source and fluorescent dye combination.

3.2.4.2 Calibration

Prior to conducting experiments, it is essential to calibrate the system. Over a certain range, a linear relationship exists between the concentration of the fluorescence solution and the fluorescence intensity signal. The following relation thus applies to the linear region:

$$C_i = \frac{C_{max} - C_{min}}{I_{max} - I_{min}} \left(I_i - I_{min} \right) \tag{3.6}$$

In the above equation, C_i is the concentration at a given point i, and C_{max} and C_{min} are maximum and minimum recorded concentration values on the calibration curve, respectively. I_i is the fluorescence intensity at a point i, and I_{max} and I_{min} are the maximum and minimum recorded fluorescence intensities on the calibration curve, respectively. This relationship allows for the concentration of a species to be determined based on the captured intensity signal.

To locate the measurement plane, the proper stage height must first be selected. In order to identify the upper and lower surfaces of the test section, the top and bottom surfaces of the device were etched, and the test section was secured to the microscope stage. The stage height was adjusted until the etches were clear and in focus on the microscope. The positions of the stage at these locations were recorded. Given the

height of the test section, a relation between the stage height and focus plane was established. The center plane, or any desired focus plane, may then be easily located. The center planes of the channels were selected for measurement. Light intensity was also adjusted to achieve uniform intensity across the investigated region. Stage height and light intensity were maintained from the calibration to experimentation process.

To begin the calibration process, an area free of obstructions, sidewalls or surface scratches must be selected for calibration; otherwise, irregularities in intensity present during calibration will affect all subsequent images. Solutions of de-ionized water and Rhodamine 6G with concentrations ranging from 0 – 1400 µg/L (chapter 4) and 0 – 750 µg/L (chapters 5 and 6) were used. To ensure strong fluorescence intensity readings, solutions with relatively high concentrations were used to account for the size of the scaled up test sections. A syringe was first filled with de-ionized water, which was supplied to the test section. The mercury lamp was turned on, the pump was started, and 30 images were recorded at intervals of 0.05 seconds at an appropriate calibration location. The process was repeated for all remaining concentrations. Resultant grey scale images were then averaged, and each concentration was related to a given intensity. A linear relation between concentration and intensity was then developed, as shown by the sample calibration curve in figure 3.3. Calibration was performed prior to each separate experimental run.
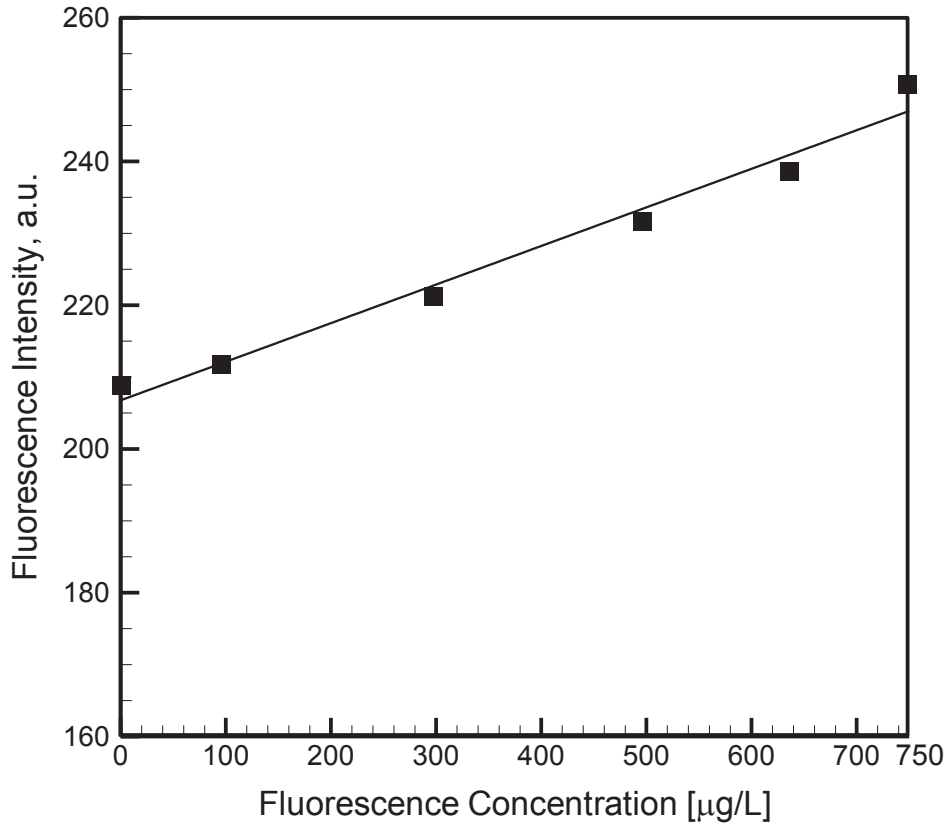
Figure 3.3: Sample calibration curve showing linear relation between fluorescence concentration and intensity.

3.2.4.3 Data Collection and Processing

As with flow visualization experiments, the channel volume was slowly filled with fluid, ensuring large air bubbles were not trapped in the channel. The test section was secured to the microscope stage, and syringe pumps were digitally set to the desired flow rates. The location of channel side walls was determined and recorded during the experimental process. Operating conditions, such as stage height and light intensity were kept constant. Figure 3.4 depicts the data processing procedure. Sixty images were captured at intervals of 0.05 seconds at a given location along the test section.

a)

b)

c)
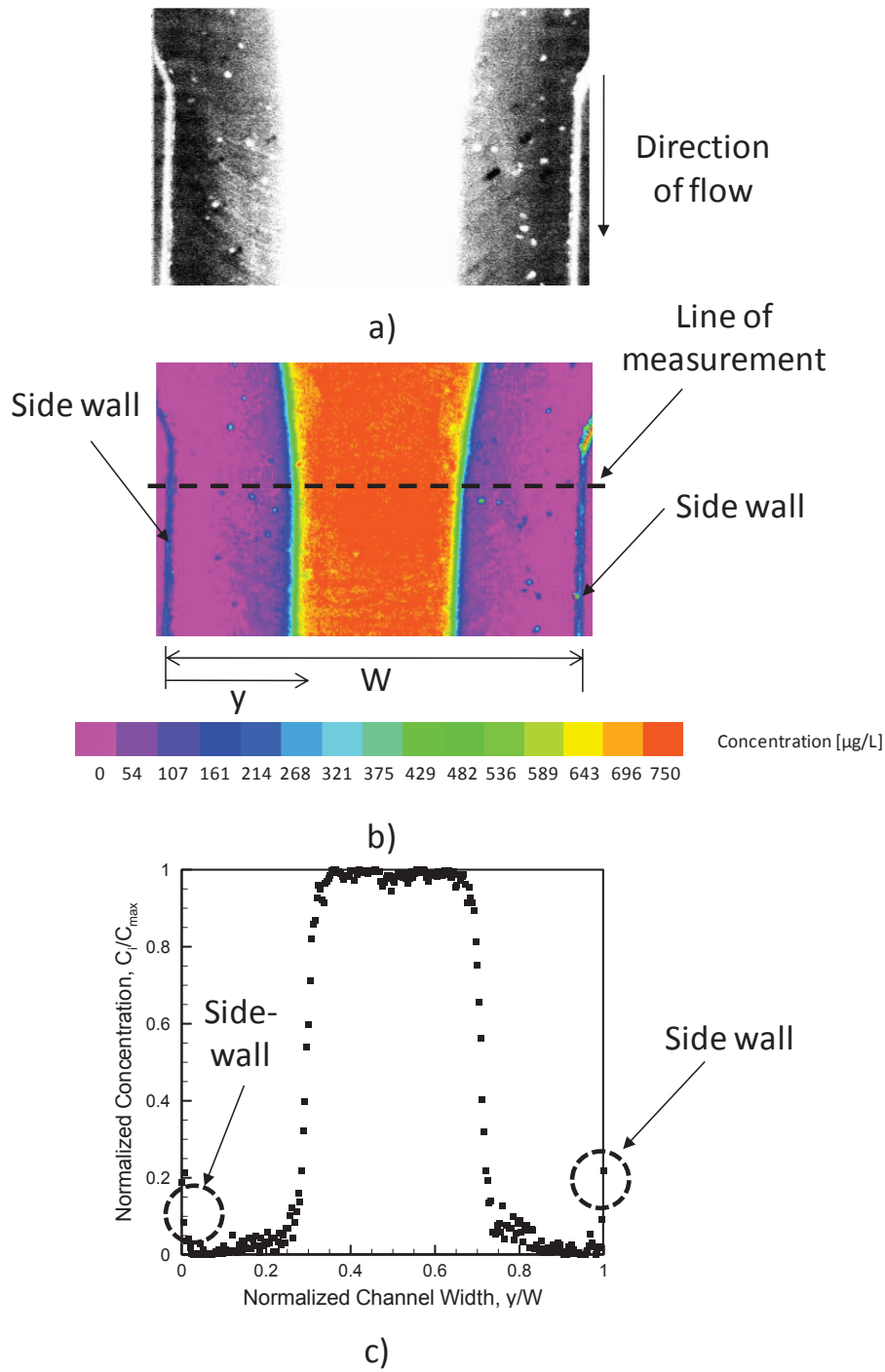
Figure 3.4: Data processing procedure. a) Grey scale image b) corresponding concentration distribution map c) concentration distribution data.

Images of 1344 × 1024 pixels were captured with a resolution of approximately 3.3 μm/pixel at 2 × magnification and 1.6 μm/pixel at 4 × magnification. These images were processed using Flow Manager Software, where re-sampling was carried out at 5 × 5 pixels, such that the resultant image resolutions were approximately 16.6 μm/pixel at 2 × magnification and 8 μm/pixel at 4 × magnification. Grey scale images were averaged (figure 3.4a) and converted to concentration maps (figure 3.4b) through use of the previously established calibration curve. To determine the concentration distribution at a certain location along the channel length, a line of measurement was selected. Data for the chosen line may then be presented in a manner similar to that shown in figure 3.4c.

3.2.5 Experimental Challenges

Experimental investigations are subject to a multitude of challenges. Test section leakage is a common problem, both at the inlets/outlet and within the channel layers. Additionally, filling the channel manually to avoid trapped air bubbles is time consuming and difficult. Any abrupt motion with the filled test section may lead to the formation of air bubbles in the channel. Care must be taken to gently place the test section on the measurement surface. As test sections were machined in cast acrylic, reflections were unavoidable, particularly at the side walls. This was apparent in IF processed images, where concentration values appeared skewed in the region of reflections. Also, regions free of surface defects and scratches must be selected for investigation, as such areas affect the recorded light intensity, and thus concentration distribution data. Due to the scaled up nature of the devices, channels occupied a

relatively large fluid volume, such that repeated filling of the syringes was required. This requires the test section to be dismounted, filled and freed of air bubbles, and re-positioned on the microscope stage. It is also challenging to achieve uniform lighting conditions. A black cardboard sleeve was used during IF measurements to reduce any external light sources.

3.3 Uncertainty

Several factors must be taken into account when considering the uncertainty associated with experimental data. Errors related to concentration should first be addressed. The accuracy of the concentration of the prepared fluorescence solutions is limited by the equipment used to produce the solutions, namely the scale (A&D HL-100, accuracy ± 0.005 g) and graduated cylinders (± 2.5 mL). To minimize errors, a high concentration stock solution was first prepared, which was then used to prepare lower concentration solutions with smaller graduated cylinders (± 0.34 mL). With time, the integrity of the fluorescence solutions deteriorated as Rhodamine 6G was found to adhere to the storage container surfaces. Slight concentration degradation is accounted for by performing calibration prior to each experiment. Errors associated with calibration curves vary with each test section. As such, calibration errors related to each mixer are discussed in their respective chapters. Minor reflections near the side walls are inevitable, though the affected region is small in comparison with the channel width. The effects of photobleaching may also be ignored, as a continuous light source is used with moving fluid. The accuracy of the syringe pumps (± 1 %) must also be noted as it

influences the volume flow rate. Manufacturing tolerances (± 0.0254 mm) also contribute to the uncertainty of results.

3.4 Numerical Evaluation

To assist in describing the complex three dimensional flow fields in the test sections described in chapters 5 and 6, numerical simulations were carried out using Fluent v13.0. Several assumptions were made: the flow was assumed to be steady state, incompressible and laminar. Governing equations are thus the continuity equation, Navier-Stokes equation and advection-diffusion equation, and are given respectively by:

$$\vec{\nabla} \bullet \vec{V} = 0 \tag{3.7}$$

$$\rho \vec{V} \bullet \nabla \vec{V} = \vec{\nabla} P + \mu \nabla^2 \vec{V} \tag{3.8}$$

$$\vec{V} \bullet \vec{\nabla} C = D \nabla^2 C \tag{3.9}$$

where P represents the pressure, and other variables were previously defined. At all walls, the no-slip boundary condition was applied, inlets were set to 'velocity-inlet', and the outlet was set to 'pressure-outlet' with a gage pressure of 0 Pa. Note that body forces may be neglected. In accordance with experimental work, properties of water were applied. The density, viscosity, and diffusivity were set to constant values of 998.2 kg/m^3, 1.003 × 10^{-3} kg/m·s, and 4 × 10^{-10} m^2/s (Gendron et al. 2008), respectively. 'Second Order' was applied for the discretization of pressure, 'SIMPLEC' mode was applied for pressure-velocity coupling, 'QUICK' was selected as the spatial discretization

for momentum and concentration. Convergence criteria were set to 10^{-10}, 10^{-5}, and 10^{-10} for continuity, velocity, and concentration, respectively. Modeling of liquid mixing is not free of numerical diffusion, however Hardt and Schönfeld (2003) proposed measures to reduce its effect, such as decreasing the grid size and applying a higher order solving scheme. Details pertaining to grid size and number and further discussed in subsequent chapters.

3.5 Mixing Performance

It is worth noting that in quantifying the mixing performance of micromixers, a lack of uniformity exits in the literature. A variety of formulas to assess mixing efficiency have been proposed, including variations of the mixing index (Ansari et al. 2010, Lu et al. 2010, Chen et al. 2011 a,b), mixing efficiency (Fan and Hassan 2010), and standard deviation in intensity (Stroock et al. 2002, Bhagat et al. 2007), amongst others. Assessing the degree of mixing is statistics-based, and is dependent on species distribution. The use of different mixing performance formulas therefore results in different mixing performance values. In certain cases, values may be converted to a common mixing performance parameter.

To quantify the degree of mixing in this work, the mixing index, *MI*, is calculated (Ansari et al. 2010):

$$MI = 1 - \sqrt{\frac{\sigma^2}{\sigma^2_{max}}} \qquad (3.10)$$

where σ, the standard deviation in concentration distribution, is a measure of the variation from the mixed value, and is given by:

$$\sigma = \sqrt{\frac{1}{N}\sum_{i=1}^{N}\left(c_i - C_{mix}\right)^2} \qquad (3.11)$$

where the total number of samples is denoted by N, and C_{mix} represents the perfectly mixed concentration. To obtain perfect mixing, the normalized concentration at a given location should be 0.5. The value of the mixing index ranges from 0 to 1, representing unmixed and perfectly mixed species, respectively.

3.6 Comparison

Similarity, as described in section 3.1, shows that mixing phenomena is preserved from scaled-up to scaled-down mixers. To accurately compare the mixing efficiency of various devices, however, it is important to consider the degree of mixing at a given length. To allow for more reasonable mixing performance comparison, an equivalent length is proposed in this work.

For a given characteristic length, or hydraulic diameter, mixing at comparable locations should be considered. Assessment based on the degree of mixing at the outlet alone is inaccurate - many devices are considerably longer or shorter than their counterparts. The length to hydraulic diameter ratio, L/D_H, provides an indication of the relative size of a given micromixer. In essence, this represents the length of a mixer compared to its characteristic dimension, or hydraulic diameter. Figure 3.5 presents two arbitrary mixers, A and B, of width W_A and W_B, respectively and length L_A and L_B,
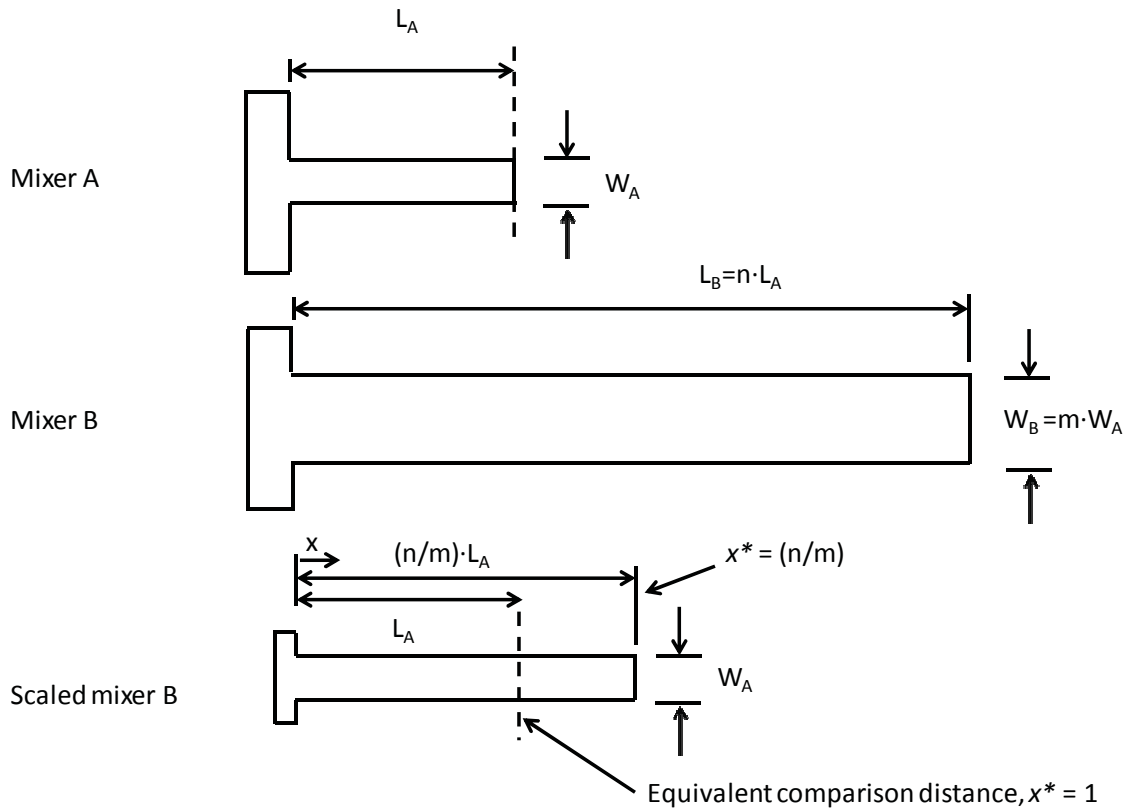
Figure 3.5: Scaling relation between mixers.

respectively. This is a simple 2-dimensional case, where the width is presented rather than the hydraulic diameter. To accurately compare mixing along the length of a given device, micromixer B should have the same hydraulic diameter (in the 3-D case) or width (in the 2-D case) as micromixer A. Figure 3.5 thus presents the scaled version of mixer B, where the hydraulic diameters (widths) are equal. Upon scaling the devices to the same hydraulic diameter, mixing along the length may now be reasonably compared.

The concept of equivalent length, x^* is introduced.

$$x^* = \left(\frac{x}{L_B}\right) \times S.F.$$ (3.12)

In the above equation, the normalized distance along the compared micromixer (micromixer B) is given by x/L_B, and varies from 0 to 1, while $S.F.$ is a scaling factor, which represents the ratio of the length to hydraulic diameter ratio of the compared devices:

$$S.F. = \frac{\left(L_B / D_{HB}\right)}{\left(L_A / D_{HA}\right)}$$ (3.13)

The scaling factor, in essence, represents how much longer (or shorter) mixer B is compared to mixer A, when both devices are at the same scale and have the same hydraulic diameter. For comparison in subsequent chapters, the scaled-up micromixers presented in this work are selected as micromixer A, such that $x^* = 1$ represents the outlet of the proposed micromixer. A value of $x^* < 1$ means the length to hydraulic diameter ratio is smaller than that of the proposed device, whereas $x^* > 1$ signifies a device with a larger length to hydraulic diameter ratio. Thus, a device which obtains a given efficiency at a lower x^* value provides superior mixing along the investigated channel length. This parameter is intended only to compare mixing efficiency based on the scale of the device.

Chapter 4

Parallel Lamination Micromixer with Tear Drop

Obstructions

A passive scaled-up parallel lamination micromixer with tear drop obstructions is experimentally investigated over $1 \leq Re \leq 100$ ($2.5 \times 10^3 \leq Pe \leq 2.5 \times 10^5$). The device promotes diffusion at the side walls by applying an uneven interdigital inlet, which greatly reduces the path of diffusion and increases species interfacial area. Staggered tear drop obstructions located along the channel length divide flow while reducing the path of diffusion and promoting the formation of Dean vortices at high Re. Flow visualization is applied to qualitatively assess mixing and flow patterns while micro-induced fluorescence provides quantitative concentration distribution data. An increasing-decreasing trend in mixing efficiency is observed with increasing Re.

4.1 Test Section

4.1.1 Design and Principle of Operation

Increasing the interfacial species area by means of parallel lamination is an effective means to reduce the path of diffusion and increase the degree of mixing. Parallel lamination allows the length of a micromixer to be reduced, as the area available for diffusion increases. Figure 4.1 demonstrates the principle of the

interdigital inlet, using only four lamellae for simplicity. In both cases, species A and B

occupy the same total channel width, i.e. the same amount of each fluid is supplied to

the test section, and a constant number of interfaces exist. This translates to:

$$\dot{m}_A = \dot{m}_B \qquad (4.1)$$

$$4x = 2x_1 + 2x_2 + 2x_3 \qquad (4.2)$$

where $\dot{m}_A$ and $\dot{m}_B$ are the mass flow rates of species A and B, respectively, and x, x_1, x_2

and x_3 are the distances shown in figure 4.1. As shown in figure 4.1a, all lamellae are

the same width, x. It is clear that the path of diffusion, p, at the sidewalls (p_1 and p_3) is

larger than that at the center of the channel (p_2), as diffusion occurs in only one

direction at the sidewalls. As such, when uniform species distribution is obtained at the

center of the channel, regions of unmixed fluid remain at both sidewalls, leading to non

uniform mixing.   It is increasingly difficult to mix species at the sidewalls as the
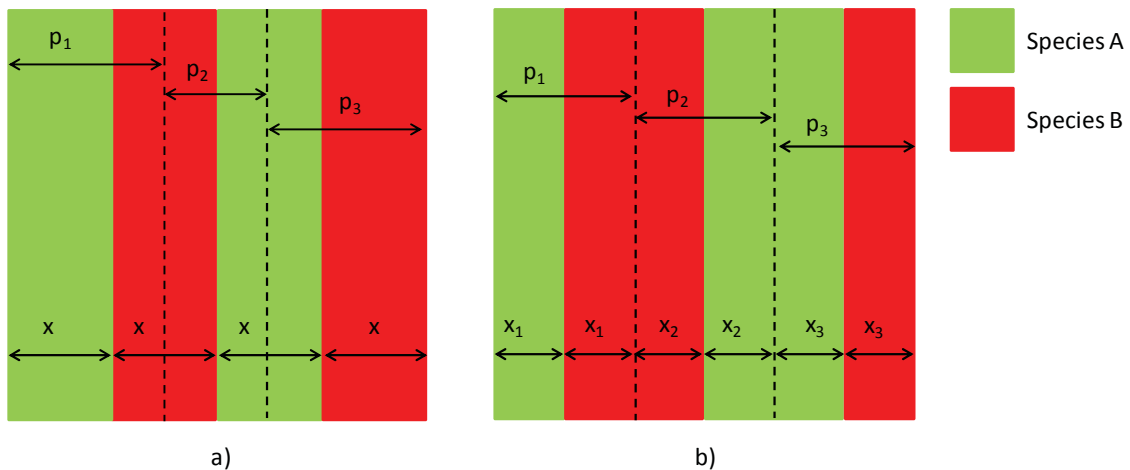
Figure 4.1: Interdigital inlet principle. a) Even lamella width b) Uneven lamella width

concentration gradient decreases along the channel length. To account for the region of
unmixed species at the sidewalls, an uneven interdigital inlet is applied. Though the
total mass flow rate and number of interfaces remain the same, the widths of the
lamellae are modified. As shown in figure 4.1b, the path of diffusion at the sidewall is
reduced when compared to figure 4.1a, allowing for more uniform species distribution
via mass diffusion along the channel length.   In the present work, a seven-lamella
uneven interdigital inlet was applied to increase the species interfacial area and allow
for increased mixing at the sidewalls.
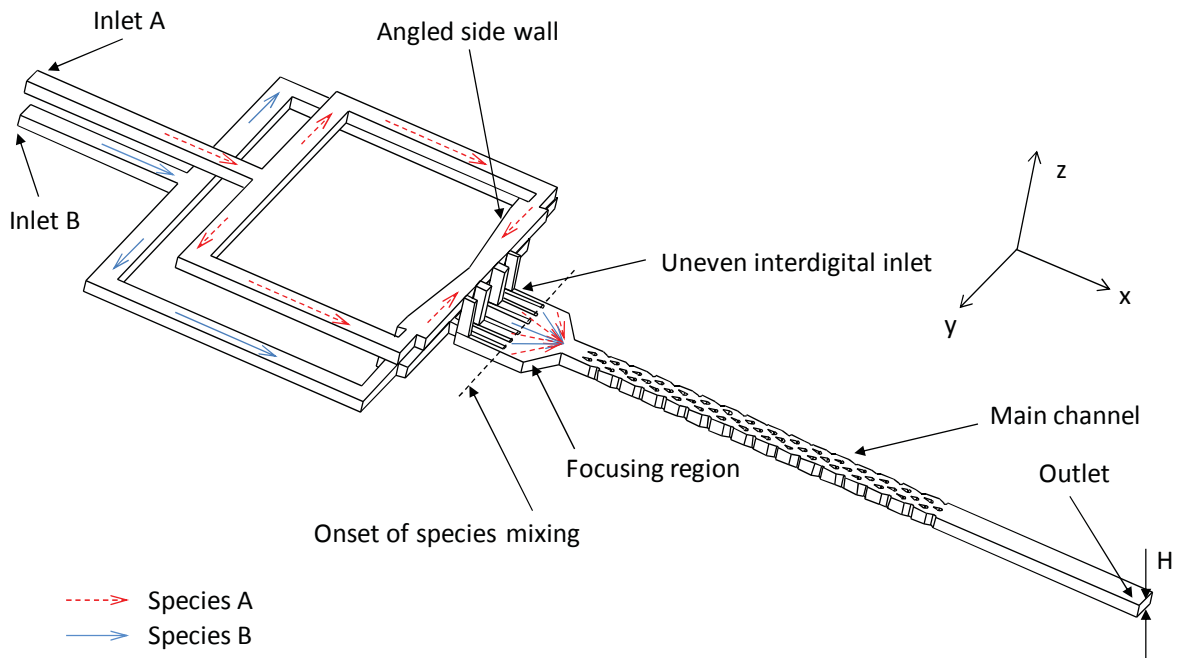
Figure 4.2: Three dimensional view of fluid domain

Figure 4.2 presents the three-dimensional region occupied by fluid. As shown in the figure, species A enters via inlet A where it is divided into 4 substreams of uneven widths and directed towards the main channel via 4 through holes. Species B enters via inlet B, and is divided into 3 substreams of uneven widths. To aid in evenly distributing species in each substream channel, the side walls have been angled. The fluids are directed parallel to each other and form a total of 7 lamellae. Figure 4.3 presents relevant dimensions and locations of measurement (L1-L4). As shown in the figure, lamellae at the side walls are thinner (t_4 = 1 mm) than those in the center, as diffusion occurs only in one direction (toward the center of the channel) at the side walls. A thicker lamella (t_1 = 3 mm) exists at the center of the channel, where diffusion occurs across each interface. The reduction in diffusion length at the side walls leads to increased mass diffusion in this region. Prior to entering the mixing region, the species are converged by a nozzle-like structure, which reduces the width of each substream. Focusing fluid in such a manner helps to improve mixing, as it forces the species to travel in a direction nearly parallel to the diffusion path, which promotes the effects of Taylor dispersion (Hong et al. 2004).

Species are then directed toward a total of 48 staggered pin obstructions. A study by Bhagat et al. (2007) showed that circular pins offered the lowest mixing efficiency amongst tested shapes. The smooth contours of circular pins, however, reduce pressure drop. The same study showed that triangular pins offer good mixing, but create dead zones. Thus, the tear drop shape aims to combine the benefits of triangular and circular elements. At higher flow rates, the curved surfaces of the tear
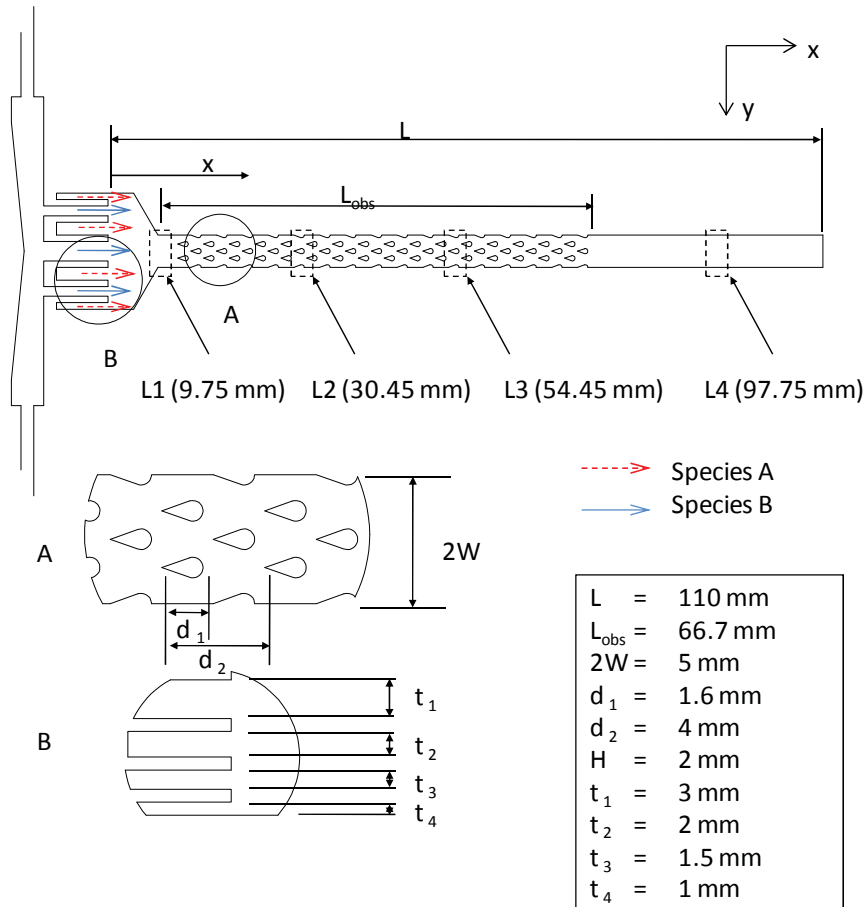
Figure 4.3: Dimensions of test section and locations of measurement.
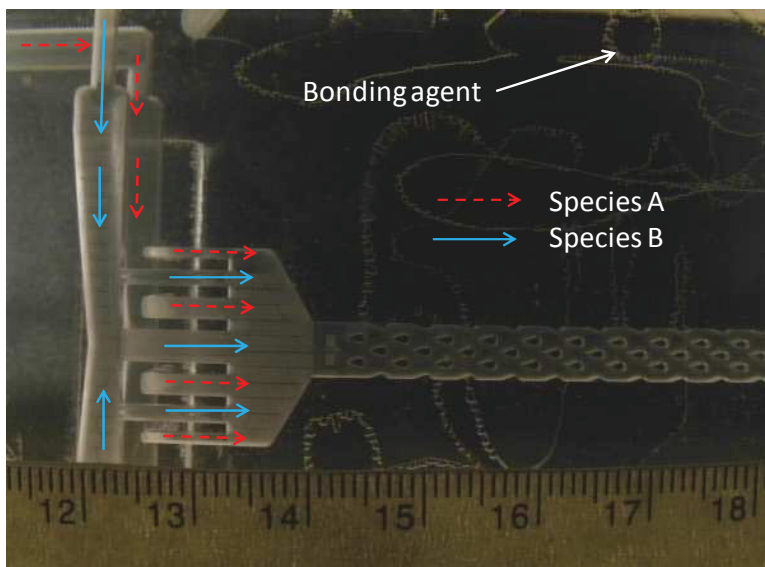
Figure 4.4: Portion of test section fabricated in cast acrylic

drop obstructions promote the formation of Dean vortices. Additional half-obstacles along the channel walls encourage fluids at the side walls to partake in mixing. As the species travel along the channel length, they are repeatedly constricted by the pins, which serve to enhance mixing efficiency.

4.1.2 Fabrication

A portion of the mixer, CNC machined in cast acrylic, is shown in figure 4.4. Three cast acrylic layers, each of which is approximately 9 mm thick, were used to fabricate the test section. Inlet B and the main mixing channel were machined on the bottom layer, while inlet A and four though holes were machined on the middle layer. The base of the middle layer serves as a cover for the bottom layer, while the top layer serves as a cover for the middle layer. Layers were chemically fused by applying di-methyl chloride, supplied via a syringe tipped bottle, to the cast acrylic surfaces. After applying the bonding agent, the test section was pressed with a weight to ensure a proper seal and reduce the amount and size of air bubbles trapped between layers. The inlets and outlet were fit with threaded barbed connections, to which flexible tubing was attached. The device was then tested for leakage by supplying fluid through both inlets, and additional di-methyl chloride was applied to the periphery of the test section, as required. Di-methyl chloride should only be applied to a dry surface to avoid the formation of opaque stains caused by a chemical reaction, as demonstrated in figure 4.4.

4.2 Species Distribution and Flow Phenomena

4.2.1 Details of Induced Fluorescence Operation

To obtain quantifiable results in terms of mixing performance, induced fluorescence experiments were conducted. It should be noted that scratches on the outer surfaces, tool marks and bubbles resulting from bonding product may cause reflections and alter the captured light intensity. As such, areas clear of visible defects were selected as the locations of measurement. These surface defects do not after the flowing domain. Before performing experiments, a test was conducted to determine which species should enter which inlet: first, water was supplied via inlet A, while the fluorescence solution was supplied via inlet B. The process was then reversed and the degree of reflections along the sidewalls was compared qualitatively. Using water as the species in contact with the sidewalls was found to reduce the appearance of reflections. As such, a syringe containing DI water was then attached to inlet A, while a syringe filled with fluorescence solution was attached to inlet B.

An objective lens with 2 × magnification was used, and provided a resultant image resolution of approximately 16.6 μm/pixel. At this magnification, a region of approximately 4.5 mm × 3.4 mm could be captured by the camera. As this is smaller than the width of the test section, half of the mixer was investigated along the symmetric plane. Relatively high concentration solutions (0 – 1400 μg/L) were used to ensure a strong fluorescence signal to account for the thickness of the test section and the fluid volume. Prior to conducting induced fluorescence experiments, calibration was

performed, as described in Chapter 3.2.4. The corresponding calibration curve is presented in figure 4.5. The maximum error associated with the calibration curve in figure 4.5 is 2.46 %, as computed by

$$error = \max \left| \frac{I_{curve} - I_{exp}}{I_{exp}} \right| \times 100 \qquad (4.3)$$

where I_{curve} is the intensity value computed by the linear relation given by eq. 3.6, and I_{exp} is the experimental intensity value at a given data point.
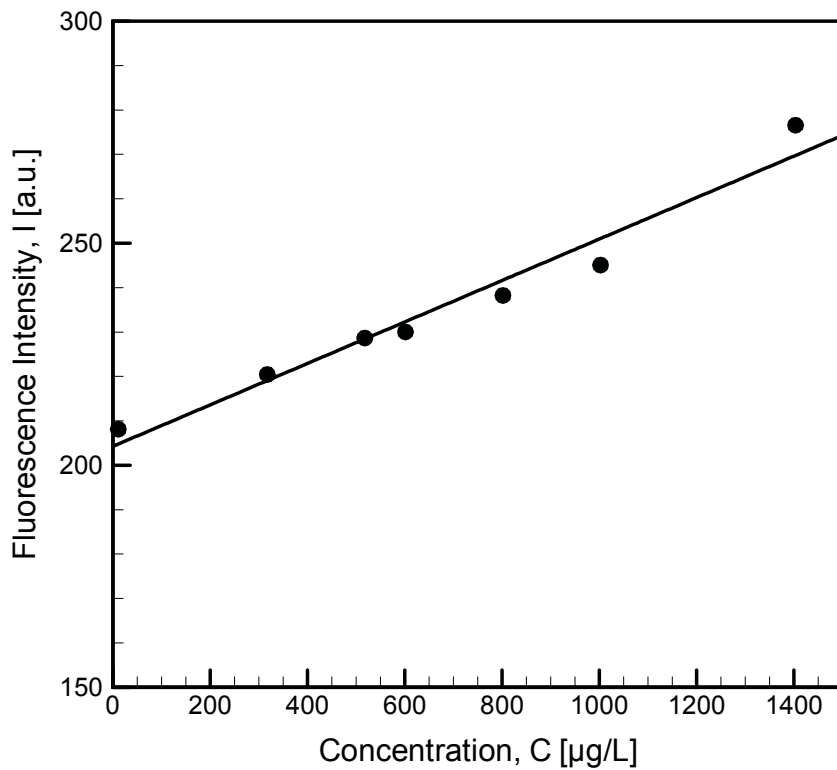
Figure 4.5: Sample calibration curve

4.2.2 Qualitative Analysis

To assess the degree of mixing and investigate flow patterns qualitatively, flow visualization was performed for $1 \leq Re \leq 100$, where the Reynolds number was based on the hydraulic diameter of the main channel, and the total fluid flow. With a diffusion coefficient of 4.0×10^{-10} m^2/s, the corresponding Péclet numbers are $2.5 \times 10^3 \leq Pe \leq 2.5 \times 10^5$, and the Schmidt number is approximately 2.5×10^3. Four locations along the channel length, denoted as *L1*, *L2, L3* and *L4* were selected for investigation, as shown in figure 4.3.

The effect of oscillations was qualitatively evaluated. As two separate syringe pumps were used to supply two individual species, pressure variations inevitably led to oscillations at the fluid interface – an observation also made by other authors (Fan and Hassan, 2010). The use of the present interdigital inlet greatly reduced the effect of the aforementioned oscillations, as fluids were supplied parallel to each other, rather than at an angle (Y-inlet) or head on (T-inlet). In the present design, flow was steady along the channel length at low Reynolds numbers; however, oscillations were visible at Re > 50, particularly along the center of the channel. The amplitude and frequency of these oscillations increased with increasing Reynolds number. As such, induced fluorescence experiments were performed over $1 \leq Re \leq 50$.

Figure 4.6 presents the flow patterns observed for Reynolds numbers 1, 10, 50 and 100 along the channel length. For all Reynolds numbers, seven separate lamellae are clearly identified at the inlet (*L1*). At Re = 1, the species interfaces are not as sharp
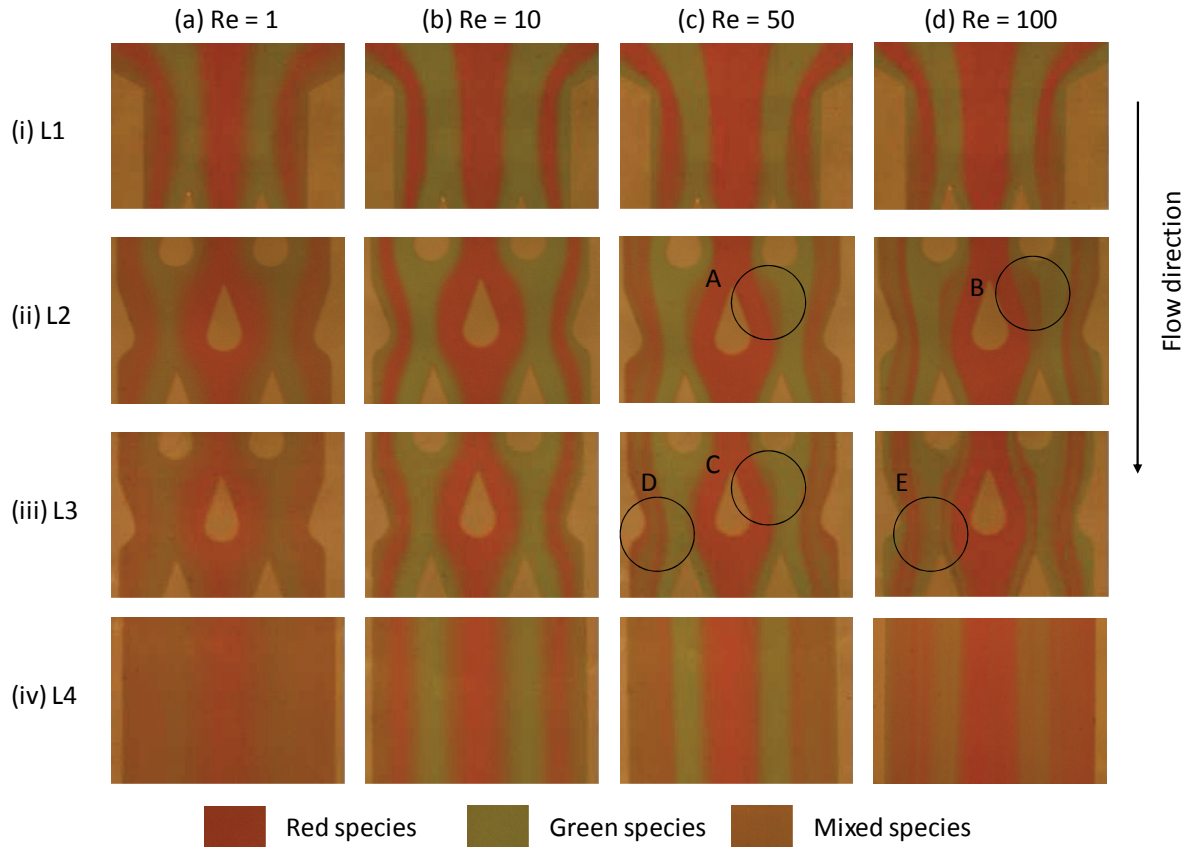
Figure 4.6: Flow visualization images over 1 ≤ Re ≤ 100 at various locations along the channel length.

as those at higher Reynolds numbers, indicating the onset of mass transfer via mass diffusion across the species interface. As expected, a comparison of images along the channel length shows increasingly blurred interfaces and more homogeneous species distribution, indicating an increased degree of mixing. The importance of mass diffusion at low Reynolds numbers is observed at the outlet (*L4*), where Re = 1 provides the most homogenous mixture, and thus the highest degree of mixing compared to other investigated Reynolds numbers. At lower flow rates, the residence time is longer, and

mass diffusion is the dominant mixing mechanism. At Re = 100, one is unable to clearly distinguish sidewall lamellae, and mixing appears to be enhanced compared to the outlets at Re = 10 and 50. At Re = 50, sidewall lamellae are again not clearly identifiable, whereas seven distinct lamella remain at the outlet at Re = 10, indicating poor mixing compared to the other investigated cases. The phenomena responsible for the varying degrees of homogeneity, namely the appearance of well mixed regions at locations A and B, and the formation of additional lamellae at locations C-E, are further explored by comparing flow visualization results with IF data.

To demonstrate the presence of Dean vortices at higher Reynolds numbers, figure 4.7 presents the flow visualization image, concentration map, and corresponding concentration distribution data at Re = 50 at L2. It should be noted that reflections due to manufacturing defects, surface scratches, and proximity to the sidewalls may lead to reflections, which appear as high concentration regions, as shown in the figure. The flow visualization image shows the formation of an apparently well mixed region at location F. From flow visualization alone, it is difficult to distinguish well mixed regions from overlapping fluids, and sharp contrast is not easily observed. The induced fluorescence image confirms the presence of a seemingly well mixed region, as shown by location G. The region of well mixed fluid, in fact, represents a tilted species interface resulting from the formation of a Dean vortex. As fluid flows around the curved wall of the tear drop element, all fluid lamellae are forced to change direction slightly, multiple times along the length of the channel. Higher-momentum species in the center of the channel are forced outward, displacing the remaining fluid in

Side wall
Tear drop obstruction
Symmetry line
Reflection
Line of measurement

F
G
H

a)
b)
c)

Red species
Green species
Mixed species

Concentration [µg/L]

0 100 200 300 400 500 600 700 800 900 1000 1100 1200 1300 1400
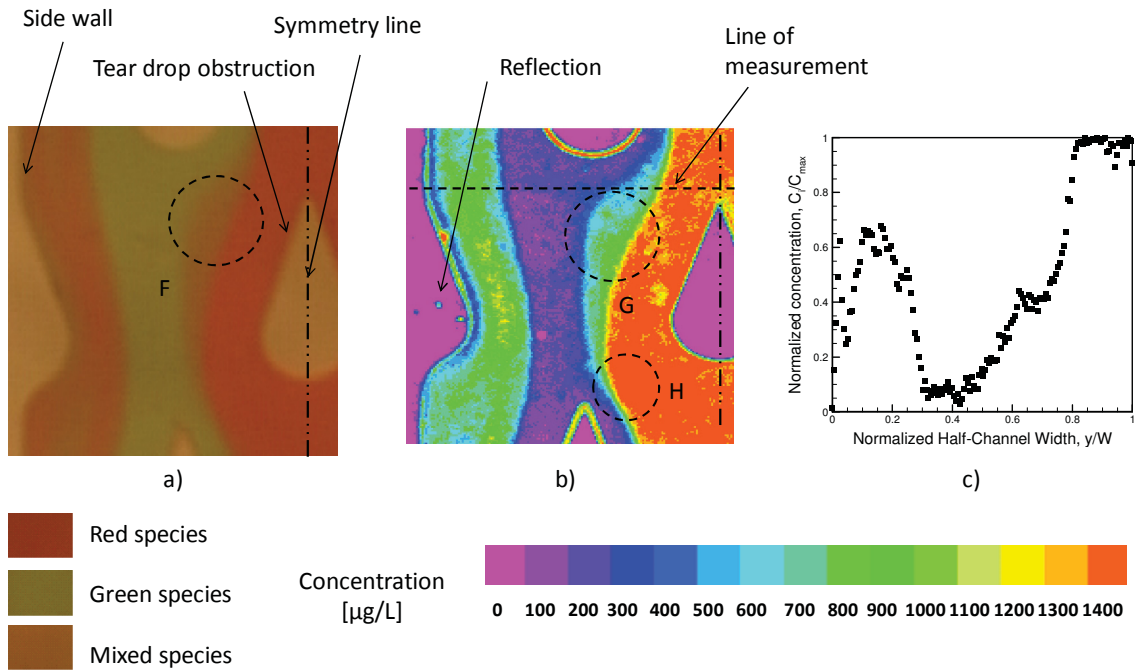
Figure 4.7: Demonstration of Dean vortex formation at Re = 50, L2. a) Flow visualization b) IF images and c) concentration distribution

Symmetry line
Reflections
Line of measurement
Peaks

I
J

a)
b)
c)

Red species
Green species
Mixed species

Concentration [µg/L]

0 100 200 300 400 500 600 700 800 900 1000 1100 1200 1300 1400
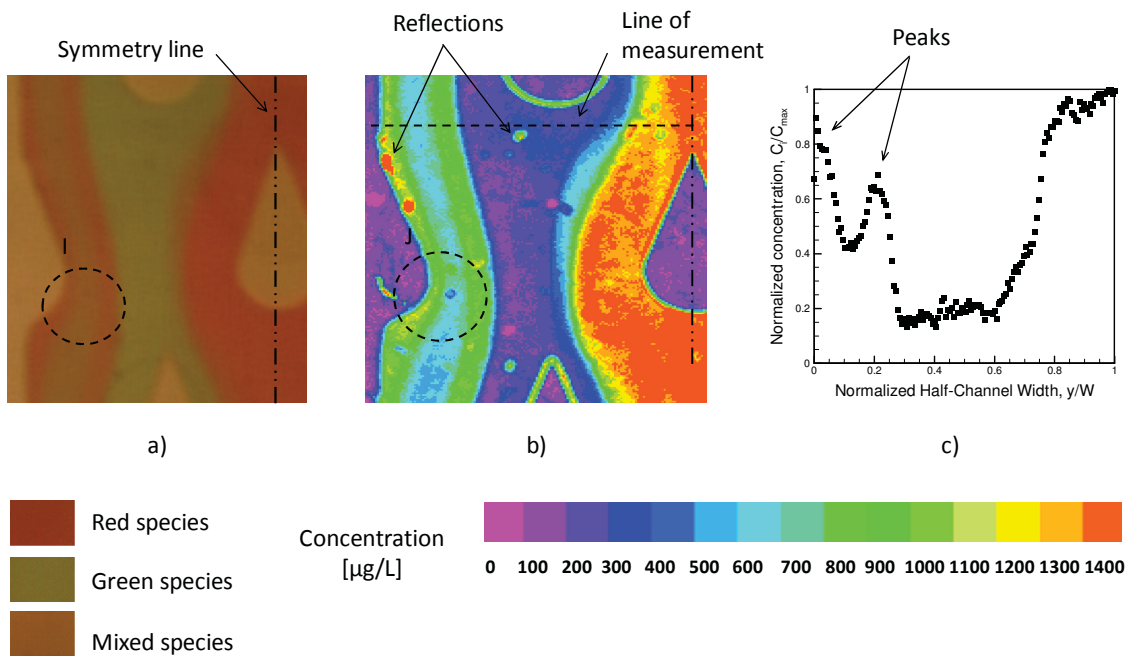
Figure 4.8: L3 at Re = 50. a) Flow visualization b) Concentration map c) Concentration distribution

compensation, and creating a tilted interface. The presence of a Dean vortex at location

G, rather than well mixed fluid, is deduced by the lack of a well mixed region at location

H. If region G was in fact a well mixed region as opposed to a Dean vortex, the mixed

fluid would propagate downstream. The same phenomenon is observed at Re = 100,

where the effect of Dean vortices is stronger. The Dean vortices present at the pin

elements at higher Reynolds numbers stretch the fluid interface, increasing the area

available for mass transfer.

The formation of additional lamellae was observed at the sidewall at Re = 50,

and at both the sidewall and center of the channel at Re = 100, as shown by locations C-

E in figure 4.6. Figure 4.8 presents location L3 at Re = 50. Dye variation at the sidewall

is difficult to distinguish at location I, using flow visualization. Induced fluorescence

measurements show the presence of additional striations at location J, and the

concentration distribution data (figure 4.8c) shows additional peaks and valleys

corresponding to regions of high and low concentration, respectively. At Re = 50, five

lamellae are observed along the channel half-width, whereas four lamellae were

present along the half-width at the inlet. The newly formed lamellae are thinner than

the originals, and are thus subject to faster diffusion, as evidenced by their reduced

amplitude in figure 4.8c. This increase in the number of lamellae and reduction in

striation thickness accounts for the improved mixing observed along the side walls at

the outlet as a result of increased interfacial area and reduced path of diffusion. A

similar phenomena is observed at a higher Reynolds number (Re = 100), but to a greater

extent, as shown by location E in figure 4.6. This phenomenon, namely the formation of

additional lamellae, was also observed by Hessel et al. (2003) at high flow rates (Re ≥ 170) in their triangular shaped interdigital inlet.

Figure 4.9 shows the effect of diffusion on mixing by comparing IF results at Re = 1 and 10 at L2. From the figure, it is clear that the most homogenous species appears at Re = 1 at the sidewalls. This is a result of mass diffusion owing to high residence time and the reduced lamella thickness at the sidewalls. Three, as opposed to four, lamellae are clearly identifiable along the half channel width. The interface is no longer sharply defined, and a more gradual concentration gradient is observed. Concentration distribution data shows a slight peak and valley at the sidewall. A comparison of IF images shows that diffusion at low Re has a significant impact on mixing. Due to a lack of significant residence time and lack of chaotic advection at Re = 10, four distinct regions remain distinctly identifiable in figure 4.9b. Extreme peaks and valleys in concentration distribution demonstrate a lack of effective mixing. Sidewall mixing is negligible, and species flow around the contours of the pins without any notable changes in flow pattern or interface distortion, unlike at higher Reynolds numbers, where Dean vortices and additional lamellae contribute to increased mixing.

To judge performance, one typically focuses on the degree of mixing at the outlet of a mixer. Figure 4.10 shows the concentration maps at the outlet (L4) over 1 ≤ Re ≤ 50. Over all investigated Reynolds numbers, the most uniform concentration distribution appears at the sidewalls, indicating the effectiveness of the reduced lamellae width in enhancing mixing. At Re ≥ 5, high concentration solution remains
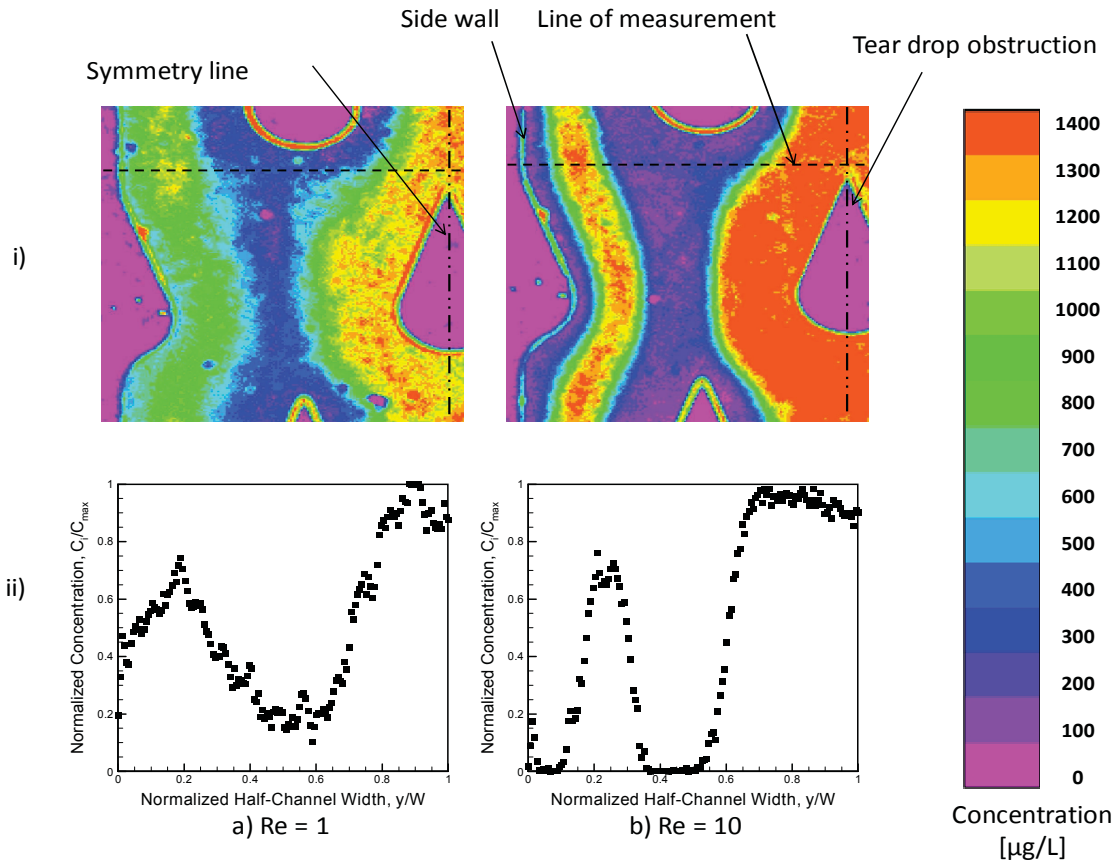
Figure 4.9: (i) Fluorescence concentration maps and (ii) concentration distribution at Re = 1 and 10 at L2.
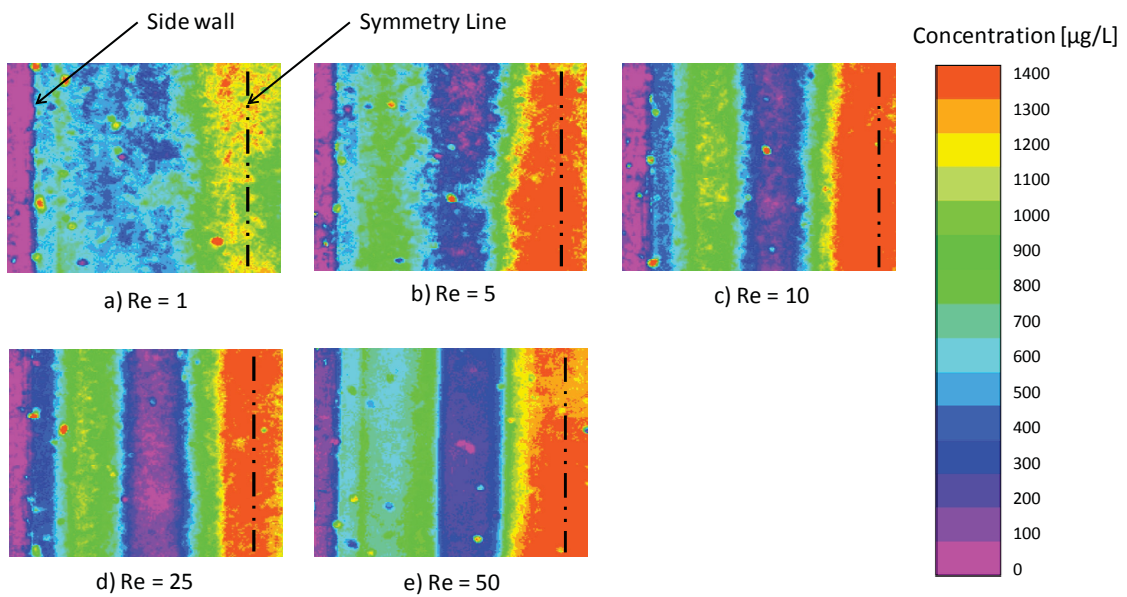
Figure 4.10: Concentration distribution at L4 (outlet) over 1 ≤ Re ≤ 50.

visible along the center of the channel, indicating ineffective mixing at this location; a thinner center lamella would allow for enhanced mixing.

4.2.3 Quantitative Analysis: Mixing Performance

To assess the degree of mixing at various Reynolds numbers, figure 4.11 presents the variation in mixing index along the normalized mixing length for $1 \leq Re \leq 50$. From this figure, a steep increase in mixing is observed close to the inlet, while the rate of increase in mixing decreases along the channel length. This is attributed to the larger concentration gradient at the inlet. Initially, the species are unmixed, such that the concentration difference is at a maximum.
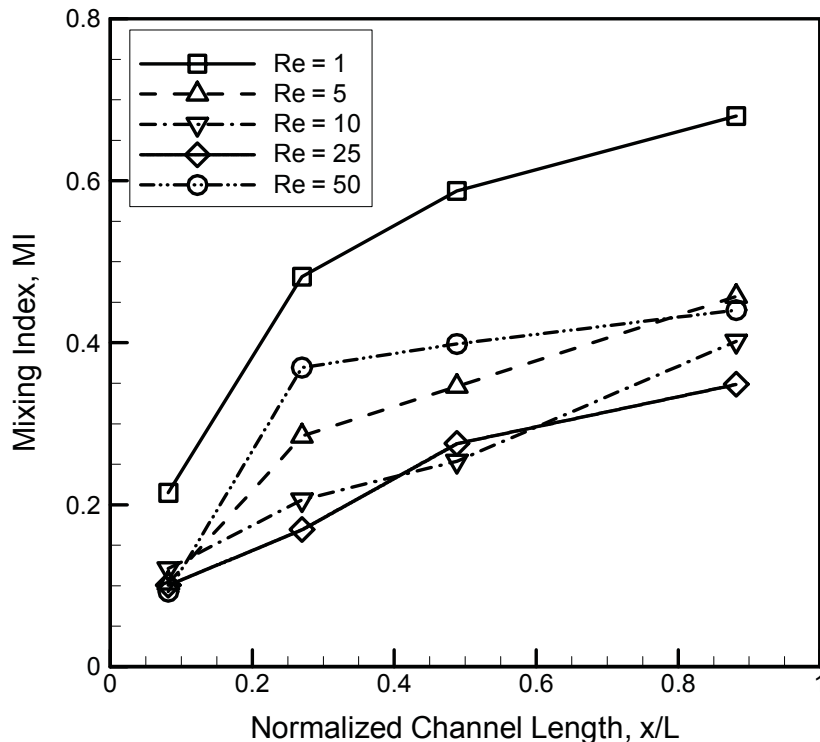
Figure 4.11: Mixing index along the channel length for $1 \leq Re \leq 50$.

At Re = 1, where residence time is highest and mass diffusion across species interfaces dominates, a rapid increase in mixing is especially noticeable. A reduction in concentration gradient results in a continual reduction in the rate of mixing increase. At Re = 50, a sharp initial increase in mixing efficiency is also observed. However, the high rate of increase in mixing is a result of the formation of additional lamellae along the sidewalls, which further reduce the path of diffusion. Once the additional lamellae have been formed, the rate of mixing increase decreases, as the additional surface area available for diffusion relies mainly on the formation of Dean vortices and interfaces meandering around the pin obstructions. From this quantitative data, the highest mixing index, 0.68, is reported at Re = 1.

Figure 4.12 presents the variation in mixing index at the outlet with increasing Reynolds number. As shown in the figure, a decreasing-increasing trend in the degree of mixing is observed with increasing Reynolds number. This trend represents the transition of the dominant mixing mechanism from mass diffusion to advection. Based on the Reynolds numbers tested, the critical value is Re = 25. Diffusion is the dominant mixing mechanism at Re < 25, whereas at Re > 25, advection dominates. At Re = 25, residence time is insufficient to promote good mixing, and the formation of additional lamellae; Dean vortices were observed only beyond Re = 25. The formation of additional lamellae increases mixing efficiency at high Re by increasing the species interfacial area and reducing the path of diffusion. Although advection dominates at higher Re, it is important to note that diffusion continues to plays an important role in enhancing sidewall concentration uniformity. The center of the channel, however, did
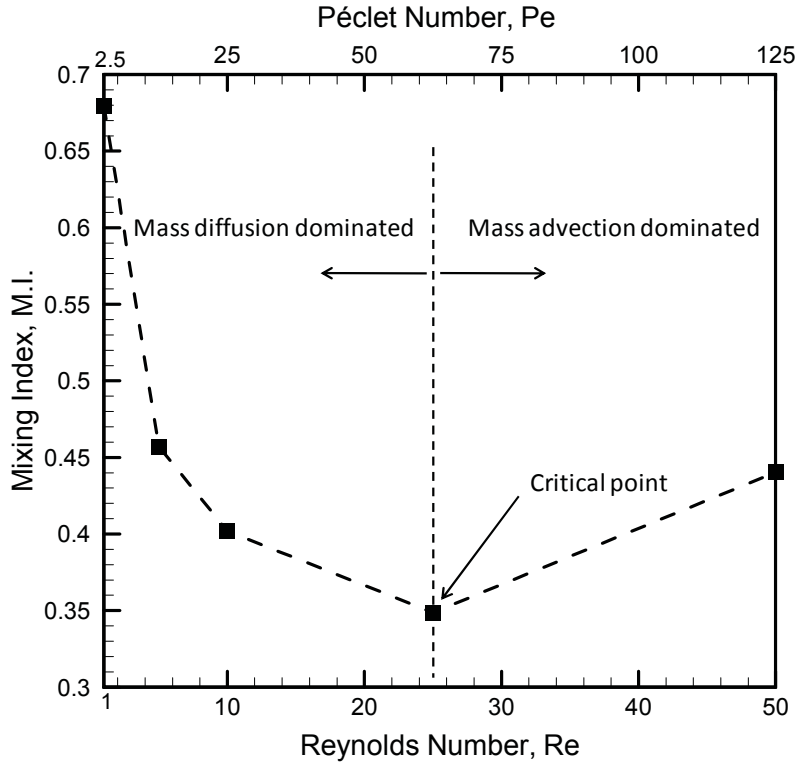
Figure 4.12: Mixing efficiency at outlet over 1 ≤ Re ≤ 50.

not experience a high degree of mixing. As the Péclet number defines the ratio of mass

advection to mass diffusion, it is an important parameter to consider. A Péclet number

of 6.25×10^4 marks the transition point in this device. The outlet mixing indices

reported for Re = 1, 5, 10, 25 and 50 are MI = 0.68, 0.46, 0.40, 0.35 and 0.44,

respectively. The concentration distribution at all positions over 1 ≤ Re ≤ 50 is shown in

Appendix A.

4.3 Comparison of Device

Numerous parameters have been defined in the literature to assess the mixing

performance of micromixers. It is important to note that the definitions of such

parameters as well as the statistical approaches used to compute these efficiencies vary from author to author, rendering accurate comparison challenging. To compare the mixing performance of devices, one must manipulate one's own data to reflect equations used by other authors. A variety of factors, including number of data points, location of measurement plane/line, and reference concentration values affect results. Values of reference concentration, C_{ref}, may be based on experimental data, given by

$$C_{ref} = \sum_{i=1}^{N} \frac{C_i}{N} \qquad (4.4)$$

or may be based on the requirements of perfect mixing, i.e. $C_{ref} = 0.5$. Mixing values obtained may vary greatly based on the reference values used.
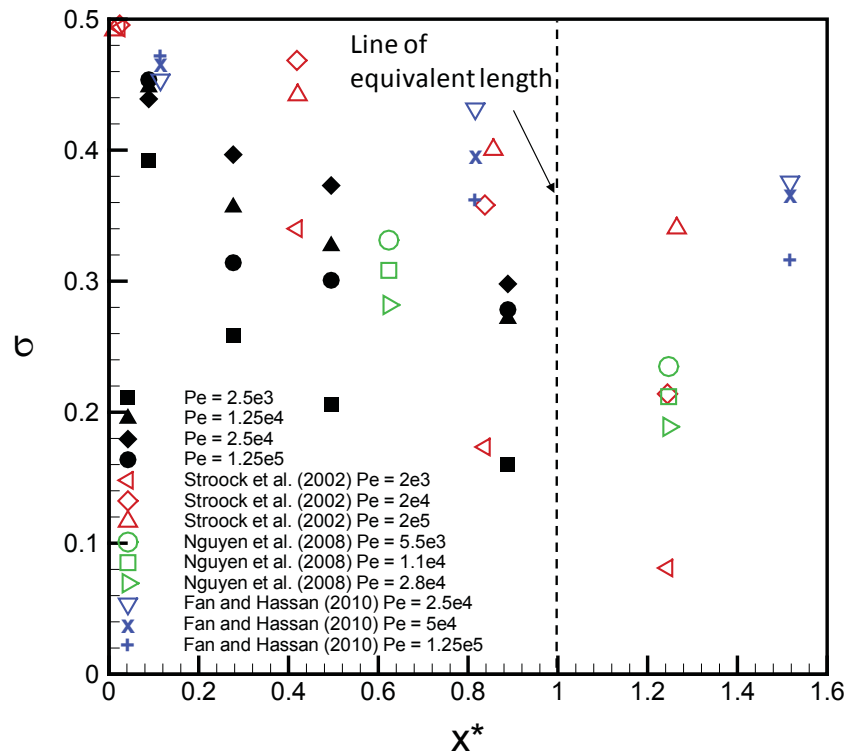
Figure 4.13: Variation in standard deviation along the comparable mixing length for various Péclet numbers.

For comparison purposes in figure 4.13, the standard deviation (eq. 3.11) was computed, and C_m or C_{ref}, was computed according to eq. 4.4, rather than using a value of 0.5. This was done to allow for consistency in comparing with published work. Figure 4.13 presents the variation in standard deviation along the equivalent mixing length for four mixers at comparable Péclet numbers. The equivalent mixing length provides a means to compare the degree of mixing of micromixers at different scales, as described in Chapter 3.6. The present mixer is used as a reference (micromixer A) in this section. Note that the equivalent length, x^*, is slightly less than 1. This is a result of outlet data being taken prior to the outlet. As shown in the figure, the present design shows the lowest values of standard deviation (i.e. higher mixing) at Pe = 2.5 × 10^3. In the vicinity of x^* = 1, mixing is comparable to the herringbone design of Stroock et al. (2002) at Pe ≈ 2 × 10^3. The herringbone of Stroock et al. is dependent on repeated helical flow patterns, and thus achieves high mixing at extended mixer lengths. Both designs showed better performance at lower Péclet numbers on the order of 10^3. The square-wave mixer designed by Nguyen et al. (2008) shows increased mixing with increasing Péclet number, and is based on chaotic advection. As such, it operates best at higher Péclet numbers (on the order of 2 × 10^4) whereas the current design outperformed that of Nguyen et al. at the lowest tested Péclet number. The scaled up cross omega mixer by Fan and Hassan (2010) operates most effectively at higher flow rates, where fluid overlap and recirculation are responsible for increased mixing. At comparable Péclet numbers, the current mixer shows improved mixing performance compared to the previous design. Note that the total channel length, taking into

account the length of the mixing units, was considered for comparison of this device. The present design exhibits a steep initial decrease in standard deviation along the mixing length; this is attributed to the interdigital inlet, which allows for a reduction in diffusion path and a sharp initial concentration gradient.

Figure 4.14 presents the mixing indices (eq. 3.13) of various mixers at similar equivalent lengths over a wide range of Reynolds numbers. To allow for more reasonable comparison, only mixers with data presented at relatively similar equivalent lengths and Reynolds numbers are shown. At a given Reynolds number, the optimal design would have both a mixing index and low comparable mixing length (i.e. be
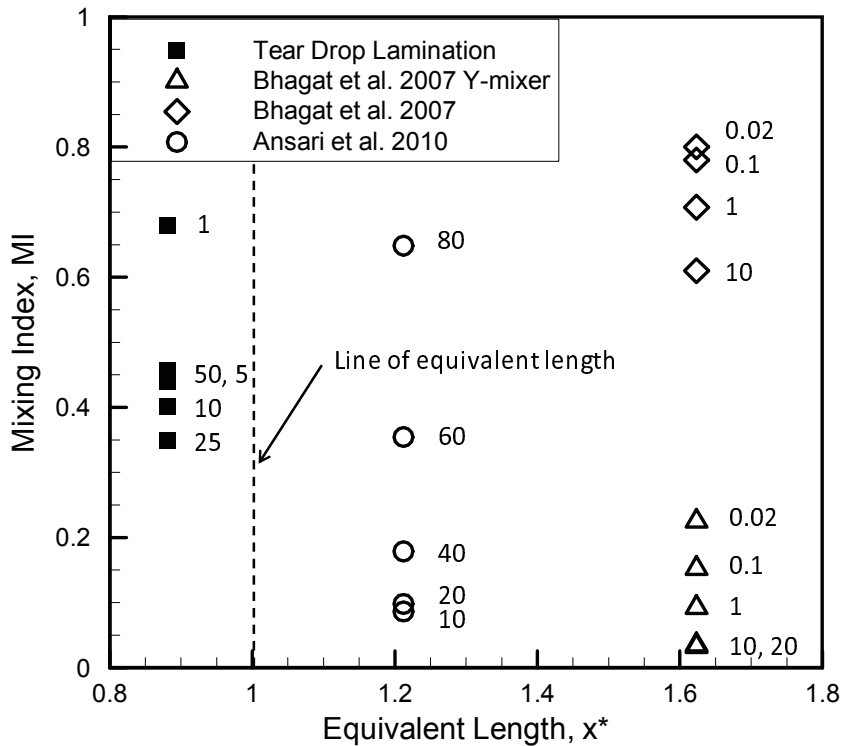
Figure 4.14: Mixing indices of various micromixers at similar equivalent lengths. Numbers next to data points indicate the corresponding Reynolds number.

located close to the top left corner of the graph). In contrast, a device with lower mixing and increased mixing length would be located at the bottom right corner of the graph. The Y-mixer of Bhagat et al. (2007) is included to demonstrate the degree of mixing obtained in a basic device, free from geometric enhancements. The diamond-obstruction based mixer of Bhagat et al. (2007) shows an increased degree of mixing at lower Reynolds number, as the device is diffusion dominant. The advection-based mixer proposed by Ansari et al. (2010), which uses unbalanced fluid collisions in curved sub-channels, also shows better mixing with increasing Reynolds numbers, and showed its highest performance at Re = 80, of the tested values. Although it is difficult to judge the difference in performance at higher Re, one may infer that at Re ≤ 50, the present device shows more thorough mixing, which is credited to the increased number of lamellae. At lower flow rates, however, the present design is preferable. Of the devices compared in figure 4.14, the present is the only one which exhibits a decreasing-increasing trend in mixing with increasing Reynolds number. This suggests its applicability for a wider range of operating conditions.

4.4 Summary

A passive micromixer based on parallel lamination and the application of tear-drop obstructions was experimentally investigated over 1 ≤ Re ≤ 100. Flow visualization was used to demonstrate flow patterns and qualitatively assess mixing, while induced fluorescence was applied to obtain quantified concentration distribution information. The uneven interdigital inlet allowed for enhanced mixing at the side walls, while the

curved portion of the tear-drop obstructions promoted the formation of Dean vortices at higher Reynolds numbers. The formation of additional lamellae, which further enhanced the degree for mixing, was observed at Re $\geq$ 50. A decreasing-increasing trend in mixing efficiency was observed with increasing Reynolds number, with a critical value of Re = 25. This critical value marks the transition from diffusion dominant mass transfer to advection dominance. The highest mixing index, 0.68, was obtained at Re = 1.

Chapter 5

Groove-Enhanced Serpentine Micromixer

A groove-enhanced serpentine micromixer based on fluid overlap and rotation is proposed and evaluated experimentally and numerically over $0.5 \leq Re \leq 100$ ($0.18 \leq K \leq 36.5$, $1.25 \times 10^3 \leq Pe \leq 2.5 \times 10^5$). As the formation of minor Dean vortices was observed in the previous investigation, a mixer integrating a meandering curved channel is proposed, allowing for the formation of Dean vortices with alternating directions of rotation. To promote flow rotation at lower Reynolds numbers, grooves are added to the bottom surface. To qualitatively assess flow patterns and species distribution along the entire channel length, flow visualization is employed. Micro-induced fluorescence is applied to quantify concentration distribution at five measurement locations over $1 \leq Re \leq 50$. Numerical simulations, validated by experimental work, allow for the highly rotational flow fields to be described and analyzed.

5.1 Test Section

5.1.1 Design and Principle of Operation

Fluid rotation and overlap have been shown to improve mixing by dramatically increasing interfacial area. Two common means exist to achieve a high degree of fluid rotation in micromixers: the use of curved channels and the application of grooves. Curved channels make use of fluid momentum at higher Reynolds numbers to promote

the formation of Dean vortices, while grooves create helical fluid flow as a result of anisotropic pressure gradients. The proposed micromixer makes use of a serpentine channel embedded with grooves to maximize the degree of fluid overlap over a wider range of Reynolds numbers.

The fluid volume occupied by the test section is shown in figure 5.1, and important dimensions are presented in figure 5.2. The main channel width and depth are 3000 and 750 µm, respectively, while the slanted grooves measure 450 µm in depth. The groove width ranges from 1310 µm to 1830 µm at the shortest and longest ends, respectively. Assuming the length of each curved portion is equal to $\pi \cdot R$, where $R = (R_{in}+R_{out})/2$, the total channel length measures 155.8 mm. To simplify the calibration process, a calibration tank, which has the same depth as the main channel, has been introduced, as shown in figure 5.2. As fluorescence results are affected by sidewall
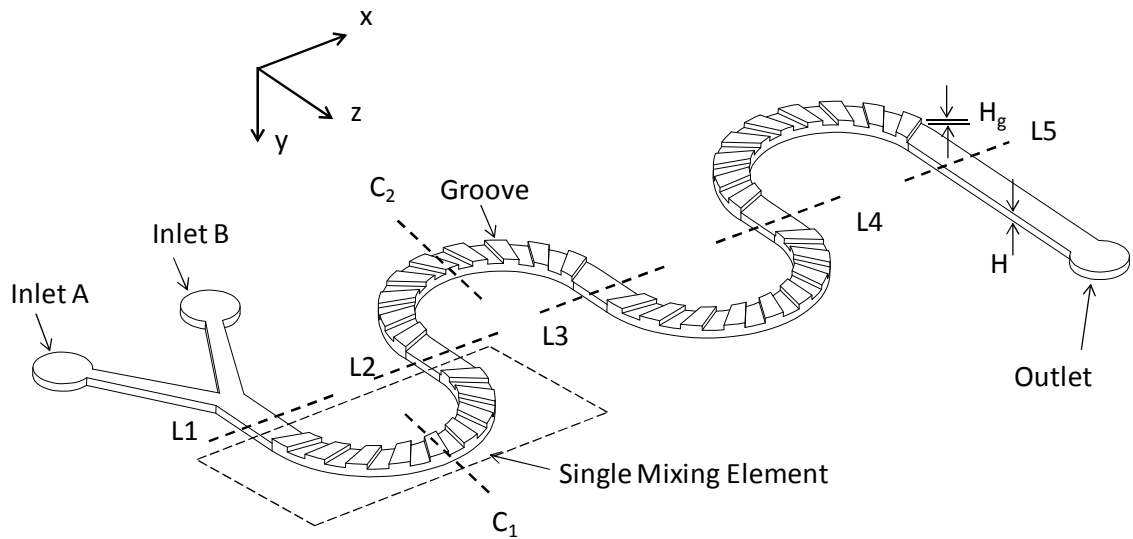
Figure 5.1: Three dimensional fluid domain showing locations of measurement.

H	0.75 mm
H_g	0.45 mm
W_{in}	1.62 mm
W	3 mm
L_{in}	7.5 mm
L_{out}	21.70 mm
R_{in}	7.5 mm
R_{out}	10.5 mm
ω	10°
Θ	20°
ϕ	20°
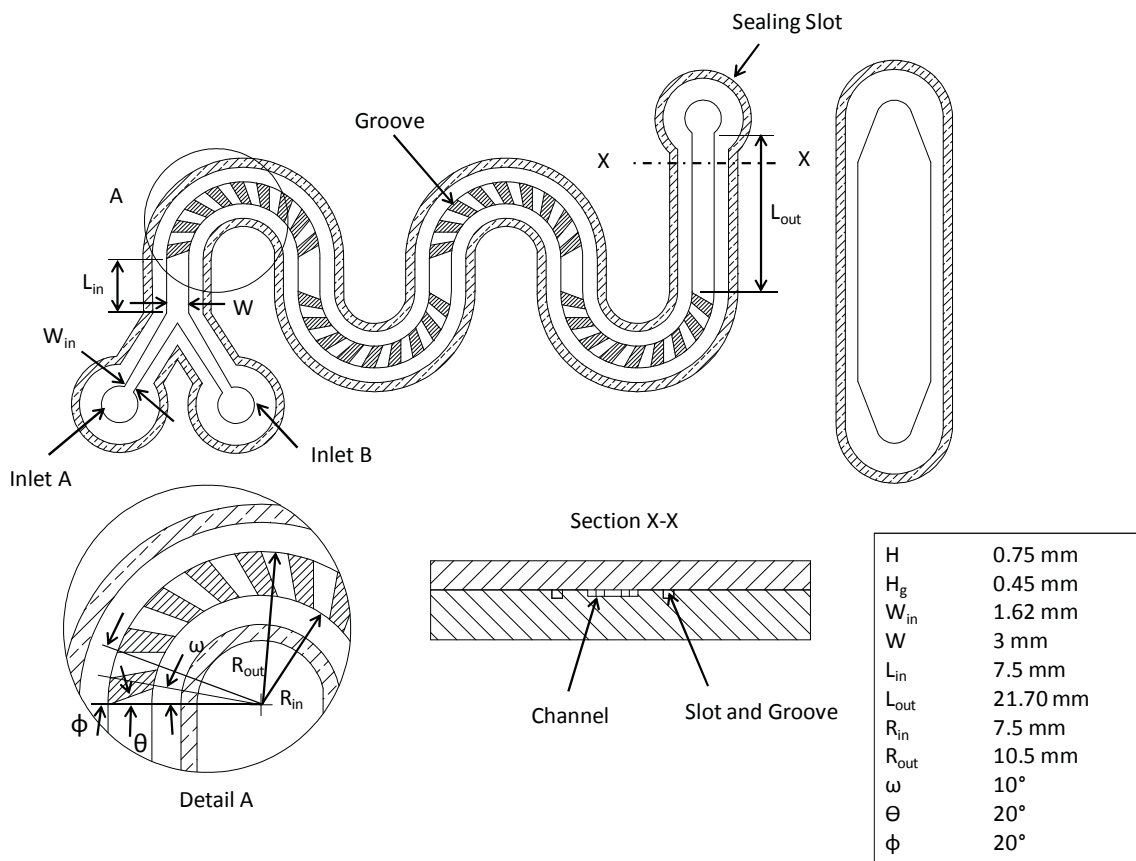
Figure 5.2: Three dimensional fluid domain showing locations of measurement.

reflections, the calibration tank is considerably larger than the channels to ensure that uniform and unaffected fluorescence intensity values are achieved. However, slight alterations in the flatness and tooling marks in the test section required calibration to be performed at each location of measurement; the calibrations tank was not used.

As shown in figure 5.1, species A and B enter via inlets A and B, respectively, in a Y-type inlet. Species are then directed toward a series of slanted grooves, located along

the serpentine channel. There are four curved channel portions, each containing 9 grooves. The sign of curvature the of channel alternates to change the direction of fluid rotation. The grooves serve to promote helical rotation due to the anisotropic pressure gradient generated along the channel. This helical motion increases interfacial species area and reduces the striation thickness, thus enhancing the degree of mixing. The curved portions of the channel serve to promote the formation of Dean vortices at higher Reynolds numbers. It is worth noting that at Re = 0.5 and 100, oscillations prevented IF measurements. The use of two separate syringe pumps supplying fluids through a Y-inlet resulted in visible oscillations at these Reynolds numbers.

5.1.2 Fabrication

To reduce fabrication costs and allow for facilitated manipulation of the device, a dimensionally similar scaled up test section was produced. The device, shown in figure 5.3, was fabricated in cast acrylic using CNC micro-machining. To obtain a flat surface, the mating surfaces of the top and bottom plates were polished. The inlets and outlet were fit with threaded barbed fittings to allow for easy tube attachment. To form a proper seal between layers, a slot and tab were machined in the lower and upper layers, respectively, as shown in figure 5.2. The tab was pressed into the slot, which was filled with transparent silicone (GE Company) via a syringe to create a leak proof seal. Thin metal clips were then placed along the perimeter of device. The mixer was easily repeatedly disassembled for cleaning by removing the clips, running a pin along the perimeter of the mixer, and gently opening the device.
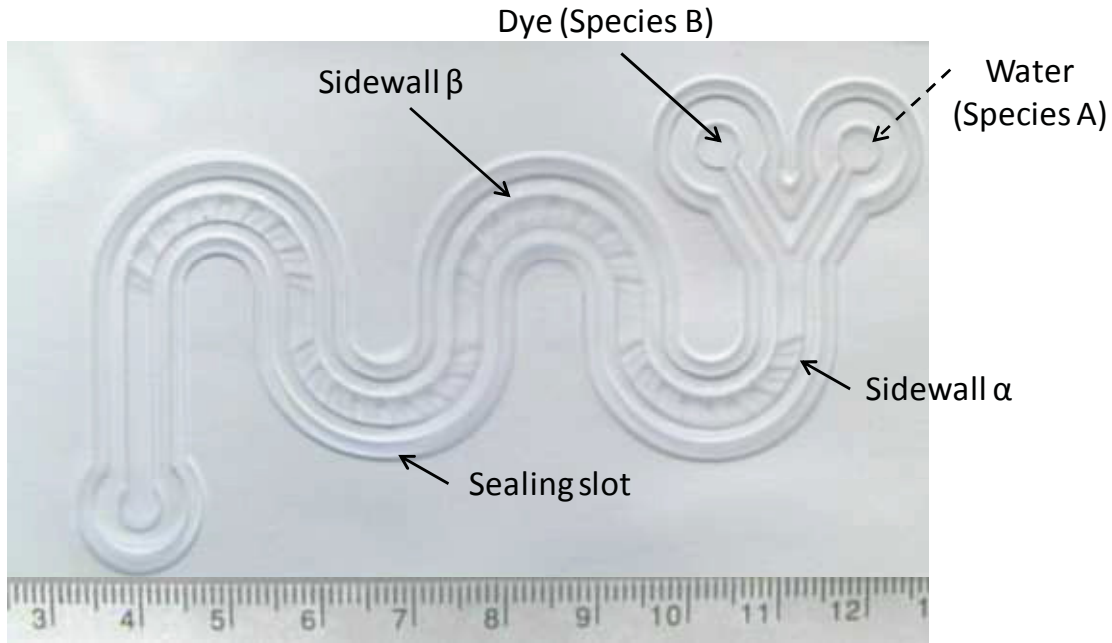
Figure 5.3: Base plate fabricated in cast acrylic (dimensions cm).

5.2 Numerical Analysis

Numerical simulations were performed to describe the highly rotational flow in the channels, as described in chapter 3.4. Quadrilateral grids were applied in the x-z plane, and the fluid volume was created by extending the plane vertically in the y-direction, as shown in figure 5.4. A refined mesh was applied to the curved, groove-enhanced channel portions, where flow patterns were expected to be complex. In the straight channel portion, a more coarse mesh was applied. To reduce computational time, grid independence was performed at Re = 100 on a single mixing element (one semi-circle) along with the inlet to determine the appropriate grid system. Figure 5.5 presents the normalized concentration distribution and the velocity distribution along the normalized channel width for a variety of grid numbers. The grid distribution

Groove

Z

X

Y

Straight Channel Portion
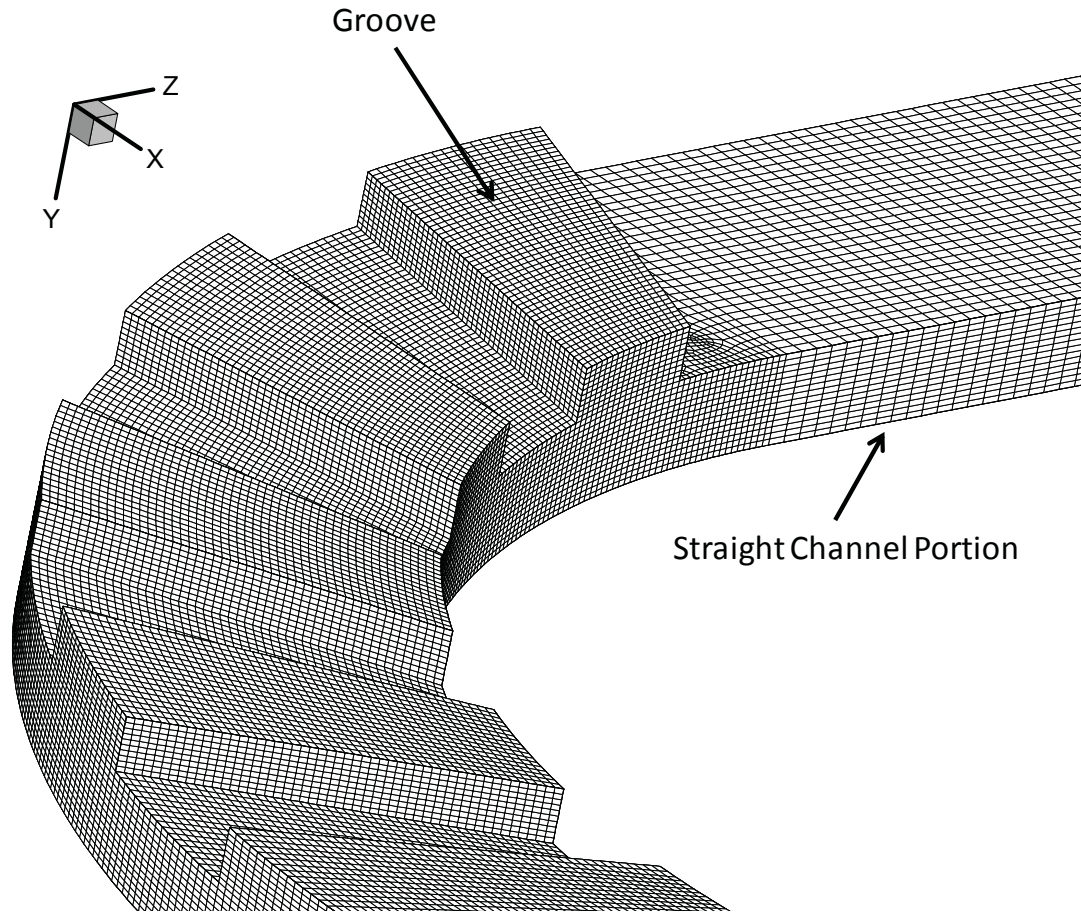
Figure 5.4: Grid system used for numerical simulation.

resulting in 0.34 M grids for a single mixing element and inlet structure was determined

as optimal; increasing the number of grids beyond this value resulted in negligible

variations in concentration and velocity distribution. This mesh size was then selected

to model the entire mixer, where the total number of elements was 1.42 M.
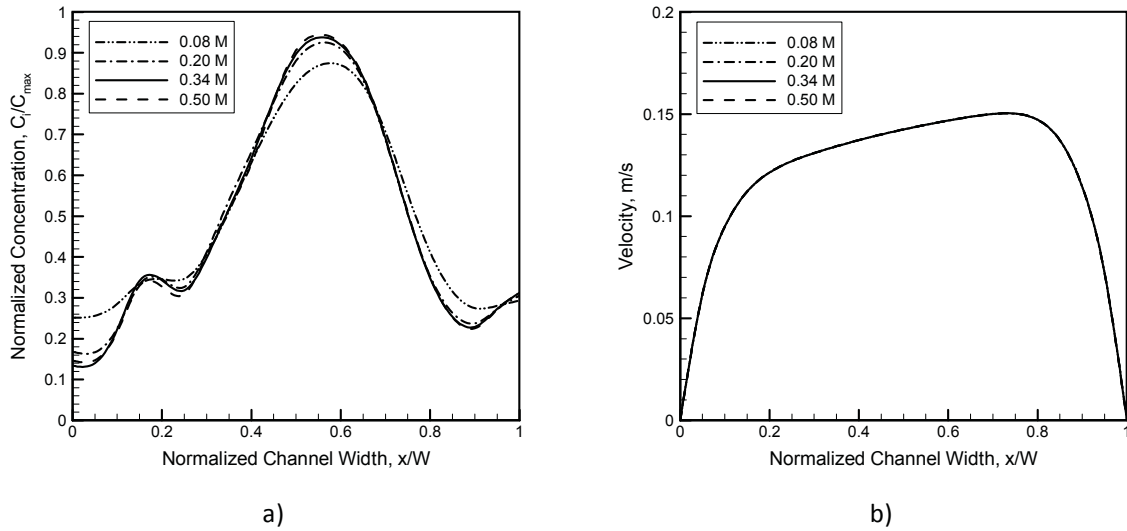
Figure 5.5: Grid independence study showing a) normalized concentration and b) velocity along normalized channel width.

5.3 Validation of Numerical Results

Prior to using numerical simulations to describe flow patterns and phenomena observed through experiment, it is necessary to validate the numerical work. Qualitatively, numerically obtained concentration distribution maps are compared to flow visualization images. Figure 5.6 presents the species distribution obtained via numerical simulation and flow visualization in the first cycle (first two mixing elements) of the mixer at Re = 50. Figure 5.6a presents rotation observed through flow visualization. Species appear as semi-transparent liquids, and remain visible throughout the channel depth. As such, fluids closer to the top surface appear to be predominant, and it is challenging to distinguish well mixed regions from curved interfaces and overlapping fluids. As a single plane is insufficient to accurately compare the flow

83
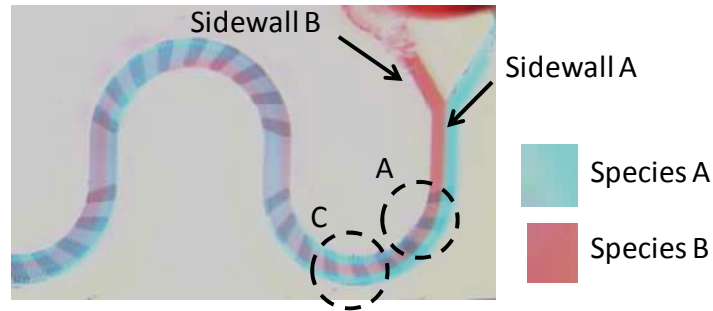
a) Flow Visualization
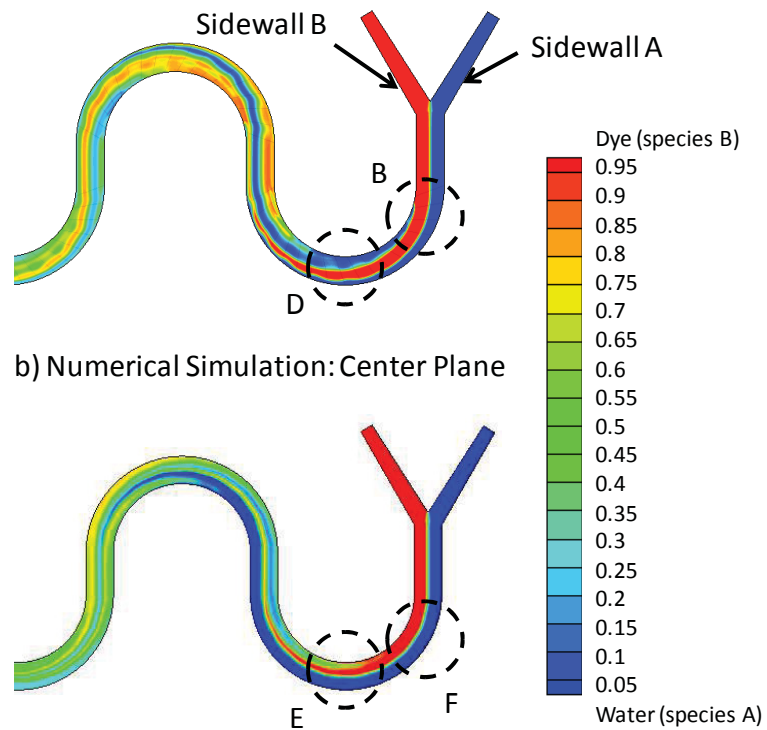
b) Numerical Simulation: Center Plane

c) Numerical Simulation: Top Plane

Figure 5.6: Comparison of flow visualization and numerical work at Re =50.

visualization and numerical results, figures 5.6 b and c present the concentration

distribution maps at the center and top planes, respectively. The onset of species

rotation is observed upon entering the groove-enhanced curved channel, at locations A

(experiment) and B (numerical). At locations C and D, species B occupies the center of the channel, while species A is in contact with both sidewalls as a result of fluid rotation. The species in contact with sidewall α appears thinner at location D than at location C due to the curved nature of the species interface and the selected plane. Location E, taken at the top plane, shows a considerably thicker striation at the sidewall. A comparison of locations B and F show an apparent lack of rotation at location F; rotation is more apparent at planes closer to the bottom of the channel. This indicates that rotation is highly affected by the grooves. The effect of grooves on species distribution is also noted along the channel length – smoother concentrations distributions are noted at the top plane, whereas the center plane shows an interface disturbance (location G).

Concentration distribution data, obtained from IF experiments, is used to quantitatively compare numerical and experimental findings. Induced fluorescence experiments are carried out under the *bino* mode at a magnification of 2 ×, with a re-sampled image size of approximately 16.6 μm/pixel. A sample calibration curve used for the evaluation of this mixer is shown in figure 5.7. The error associated with calibration, according to equation 4.3, is 0.86%.

To quantitatively compare numerical and experimental results, figure 5.8 presents the concentration distribution data obtained through numerical simulation and IF experiments at Re = 1 and 10 at L1 and L2, and demonstrates good agreement. The
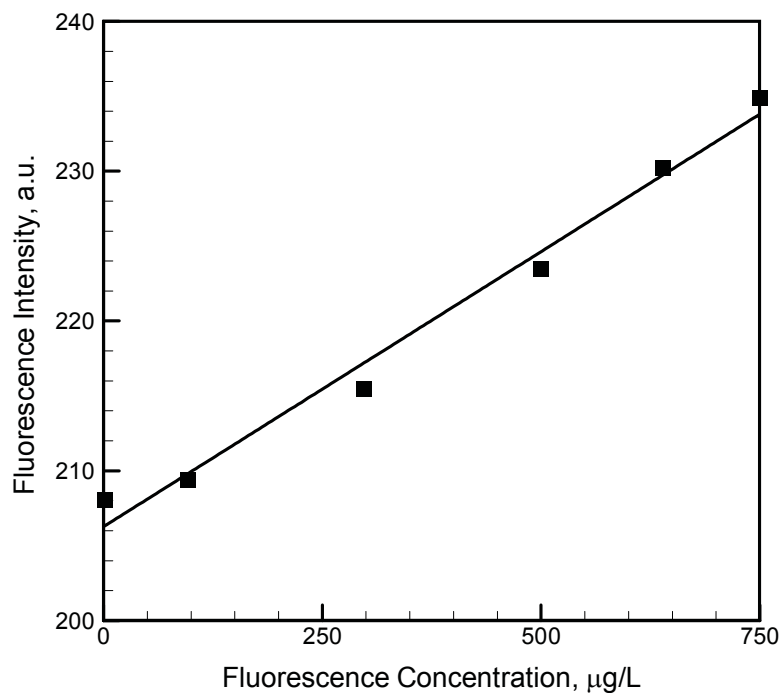
Figure 5.7: Sample calibration curve.

first two locations were selected for comparison as the concentration gradient is highest, allowing for easier comparison and more distinguishable fluids. It is worth noting that the IF technique employed is of a whole-volume nature, meaning that the fluorescence signal is captured throughout the channel volume. The signal, however, is clearer at the focus plane, which was set to the center of the channel. To replicate the experimental data as closely as possible, the numerical concentrations were averaged in the y direction for each x position (see axis on figure 5.1). Low concentration solutions (C = 0) are slightly higher than the expected value as a result of reflection. In figure 5.8c, the experimentally obtained interface diverges slightly from the numerical results, likely due to minor oscillations which arise from the use of two individual syringe pumps. As

good agreement exists between experimental and numerical work, the numerical work

is further used to evaluated the three dimensional flow within the channel.

5.4 Species Distribution and Flow Phenomena

5.4.1 Qualitative Analysis

Figure 5.9 presents the flow visualization images taken along the entire channel

length over $0.5 \leq Re \leq 100$. As shown, the strength of rotation increases with increasing

a) Re = 1 L1

b) Re = 1 L2

c) Re = 10 L1

d) Re = 10 L2
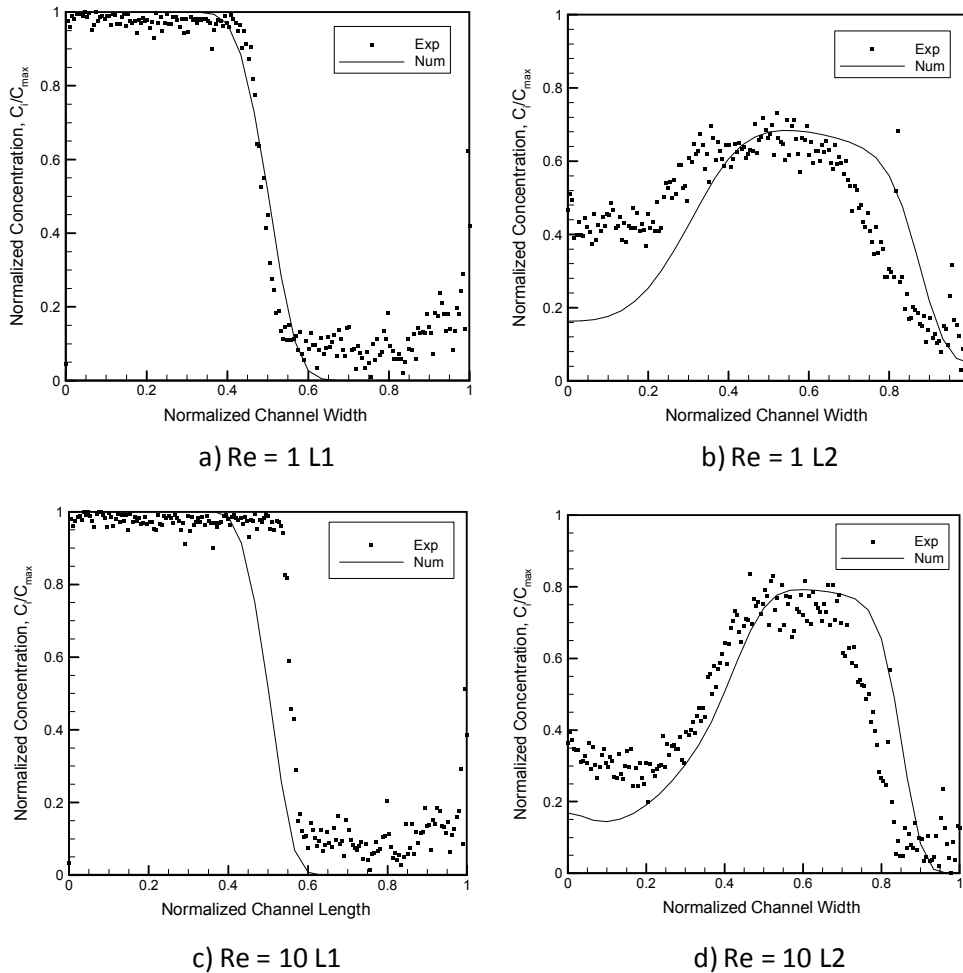
Figure 5.8: Quantitative comparison of numerical and experimental (IF) data.
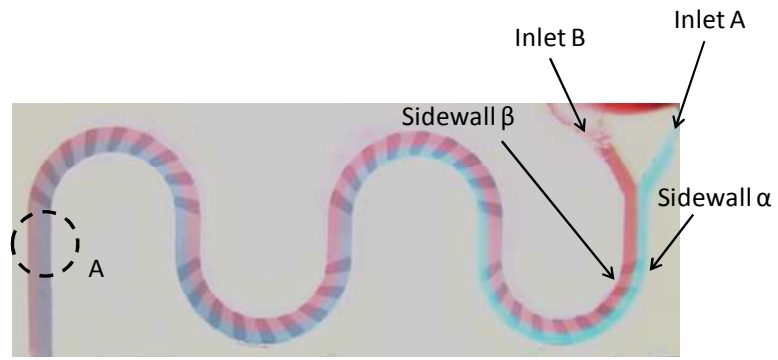
a) Re = 0.5
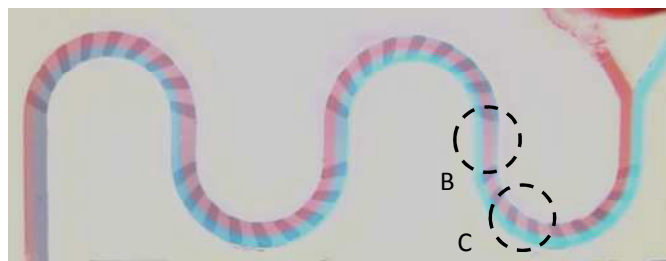
b) Re = 1
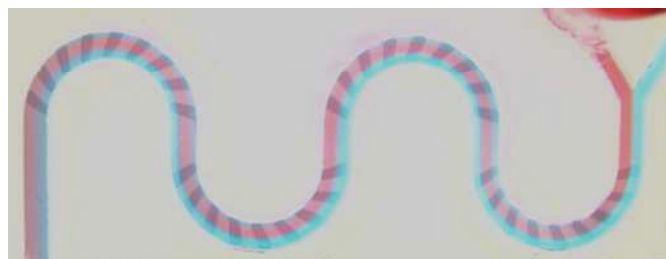
c) Re = 5
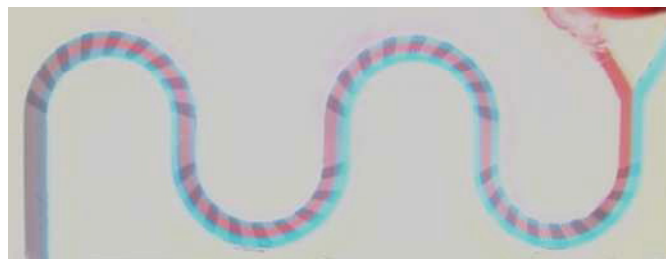
d) Re = 10

Figure 5.9: Flow visualization over 0.5 ≤ Re ≤ 100.

e) Re = 25

f) Re = 50

g) Re = 100
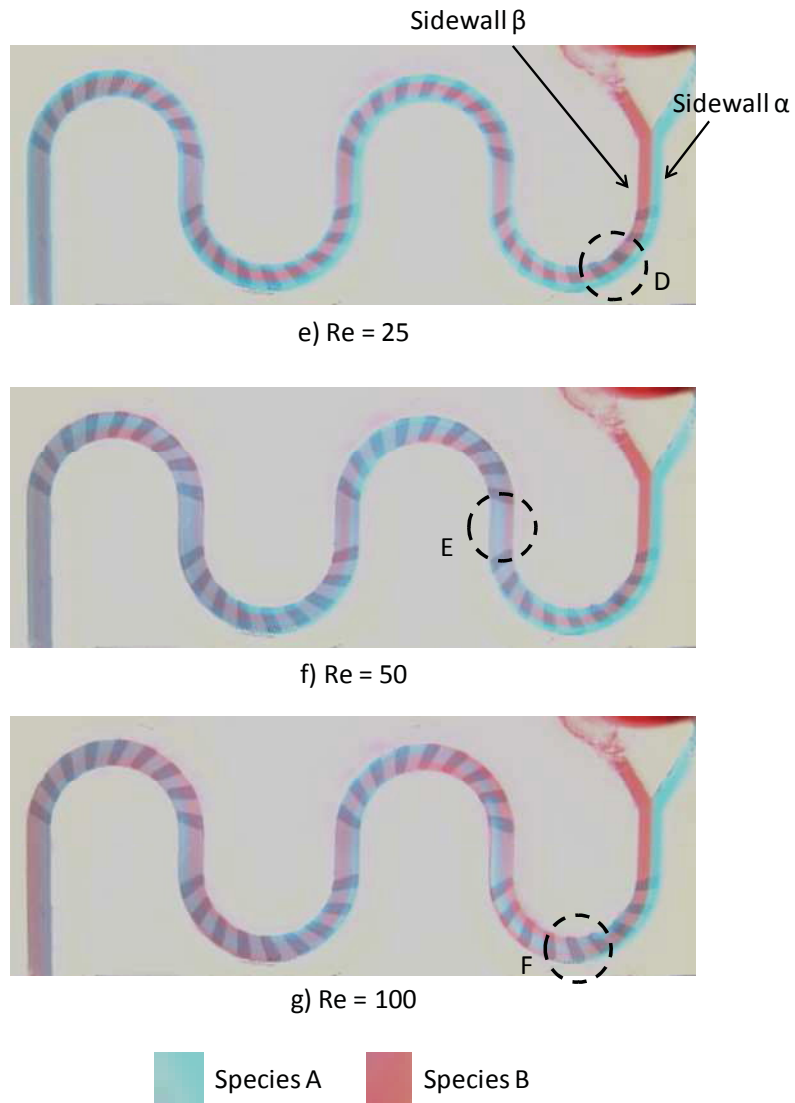
Species A   Species B

Figure 5.9 cont'd: Flow visualization over 0.5 ≤ Re ≤ 100.

Reynolds number. The flow pattern, governed by the geometry of the test section, is periodic. A repetition is noted from one cycle (L1 to L3) to the next (L3 to L5). At Re = 0.5, Species A (from inlet A) appears to remain in contact with sidewall α along the channel length, whereas species B remains in contact with sidewall β - rotation is difficult to identify. A close-up of location L2 (figure 5.10a), however, shows that

species A has migrated toward sidewall β, indicating that rotation has occurred. Mass diffusion is credited with the relatively uniform species distribution observed at the outlet, at location A (figure 5.9a). Qualitatively similar flow patterns are observed for Re ≤ 25. Location B (L2) shows species A in the center of the channel, with species B on either side. This phenomena is observed at all Reynolds numbers up to Re = 25, and is a result of species A being entrained into the grooves and directed from wall α to wall β. The onset of rotation occurs earlier at higher Reynolds numbers, as shown by comparing locations C and D, which point out an identifiable striation of species A in contact with sidewall β.
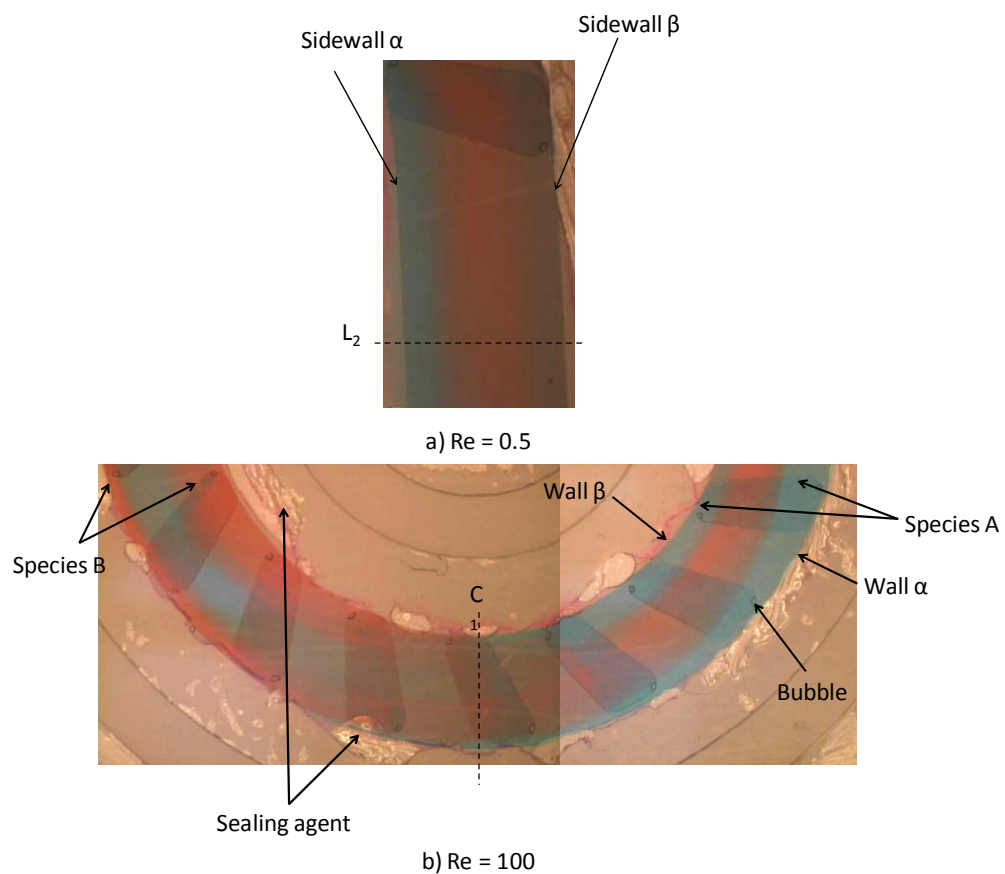
Figure 5.10: Flow visualization over 0.5 ≤ Re ≤ 100.

At Re ≥ 50, a considerable change in flow pattern is noted. Fluid layers are no longer easily identifiable, and a high degree of fluid overlap is noted, as shown by locations E and F (figure 5.9 f and g). To demonstrate the highly rotational nature of the fluid at Re = 100, figure 5.10b shows a close-up of the first mixing element. As shown, at the entrance of the first mixing element, species A is in contact with both sidewalls as a result of the grooves directing species A from sidewall α to sidewall β. Towards the center of the mixing element, a strong degree of fluid overlap is observed.   At the exit of the element, a complete reversal in species location is observed: species B is in contact with both sidewalls.

a) Re = 0.5
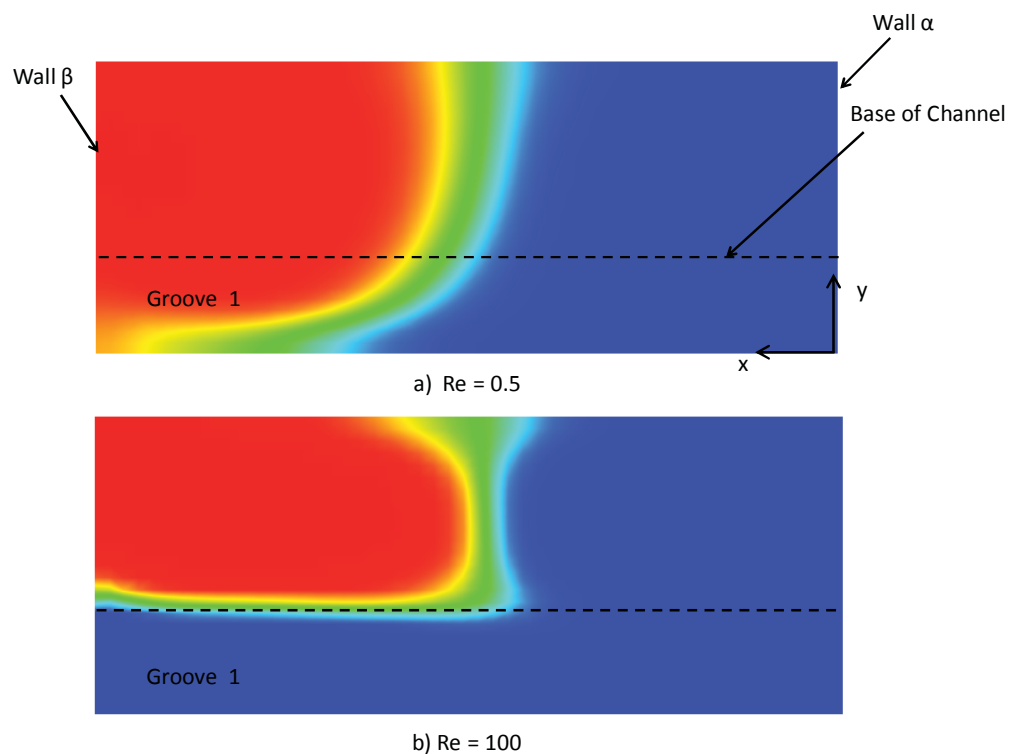
b) Re = 100

Figure 5.11: Concentration distribution at the first groove.

Figure 5.11 shows the difference in rotation at the first groove at Re = 0.5 and Re = 100. In both cases, species A is guided into the grooves and directed toward sidewall β. At Re = 100, the groove is completely filled with species A, leading to increased fluid transport. As shown, the degree of fluid transport resulting from the grooves increases with increasing Reynolds number.

To further describe the highly rotational flow within the channel, figure 5.12 shows the concentration distribution over the channel cross section at C_1 and C_2, as identified in figure 5.1. Streamlines are superimposed on the concentration contours at Re = 0.5, 25, 50 and 100. These Reynolds numbers were selected as they demonstrate notable changes in flow phenomena; qualitatively similar streamlines were observed for Re ≤ 10. Figures 5.12 a and b present the concentration distribution and streamlines at Re = 0.5. At lower Reynolds numbers, residence time is high and diffusion dominates. Grooved structures lead to an increase in interfacial area; species A is entrained into the grooves, travelling from the outer wall toward the inner wall of the channel, in a manner similar to that shown in figure 5.11a. Along the channel length, species are continually directed along the grooves from the outer to inner wall, and a helical motion results from an anisotropic pressure gradient. A lack of strong fluid rotation does not allow for significant interfacial area to be available for mass transfer at Re = 0.5. At Re ≤ 25, fluid rotation is a result of the grooves on the channel base. Beyond this value, flow rotation is a result of not only the grooved structures, but also of the formation Dean vortices. At Re = 25 (figure 5.12 c and d), the formation of a single vortex is noted near the middle of the top wall of the mixer. Beyond this value, two counter rotating vortices, known as

Dean vortices, are observed in the curved portion of the channel. Fluid at the center of

the channel is forced toward the outer wall, while fluid at the outer wall is forced

upward and downward in compensation. At Re = 100 (K = 36.5), the strength of the

vortices is increased compared to Re = 50 (K = 18.25), and the species interfacial
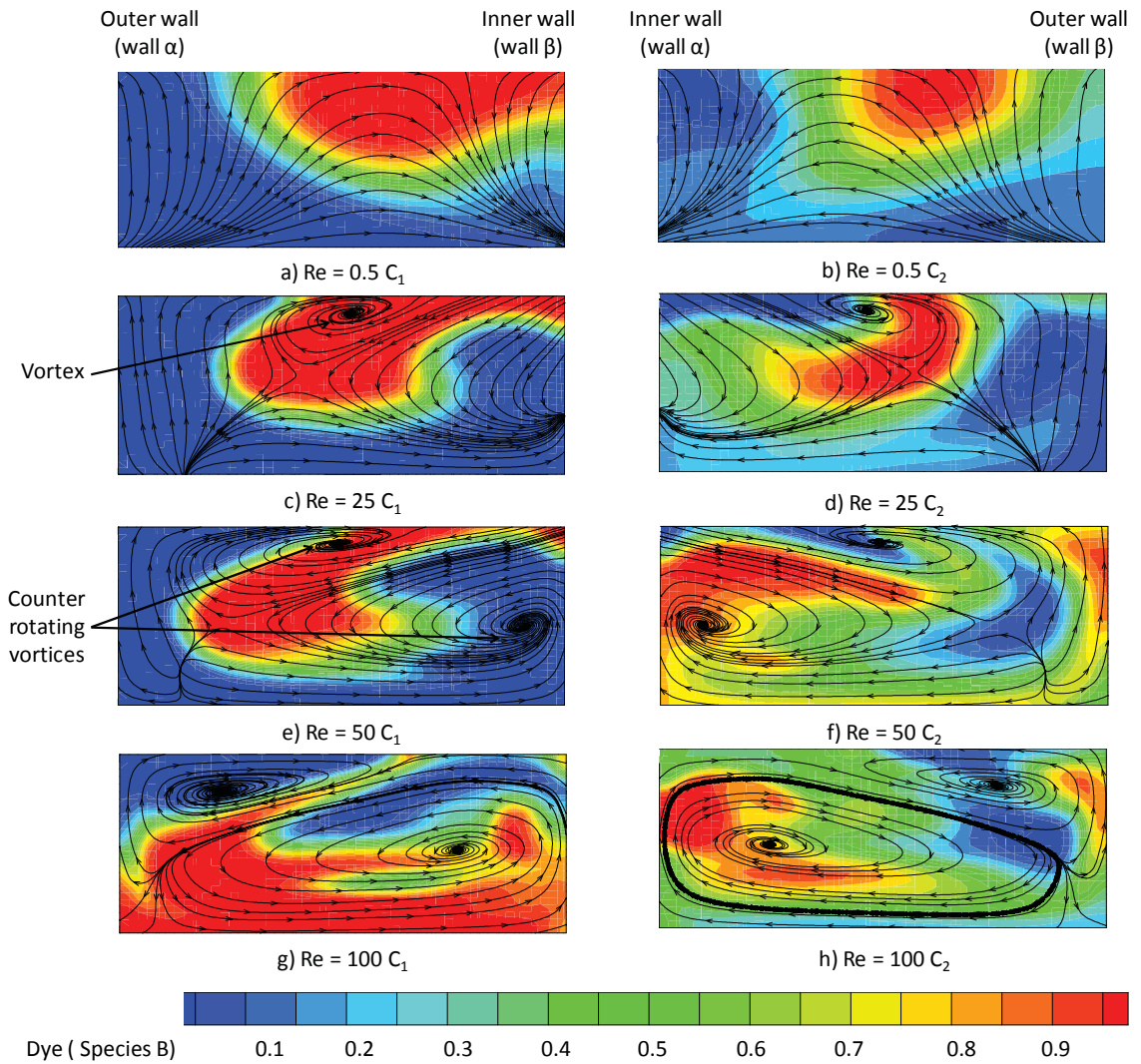
Figure 5.12: Concentration distribution and streamlines at C1 and C2.

area is dramatically increased. This enlargement in surface area allows for increased mass transfer to occur across the interface, further increasing the degree of mixing. With increasing Re, the vortex cores shift toward the outer wall, a phenomenon also observed by Jiang et al. (2004).

Figure 5.13 compares results obtained from experimental and numerical investigations at Re = 10 at location L2. Figure 5.13a shows the flow visualization image, depicting species A in contact with both sidewalls, and species B occupying the center of the channel. The concentration distribution is clearly noted in the IF image, shown in figure 5.13b. At this location, three fluid striations appear to exist. From these experimental techniques, it is challenging to distinguish overlapping or horizontally
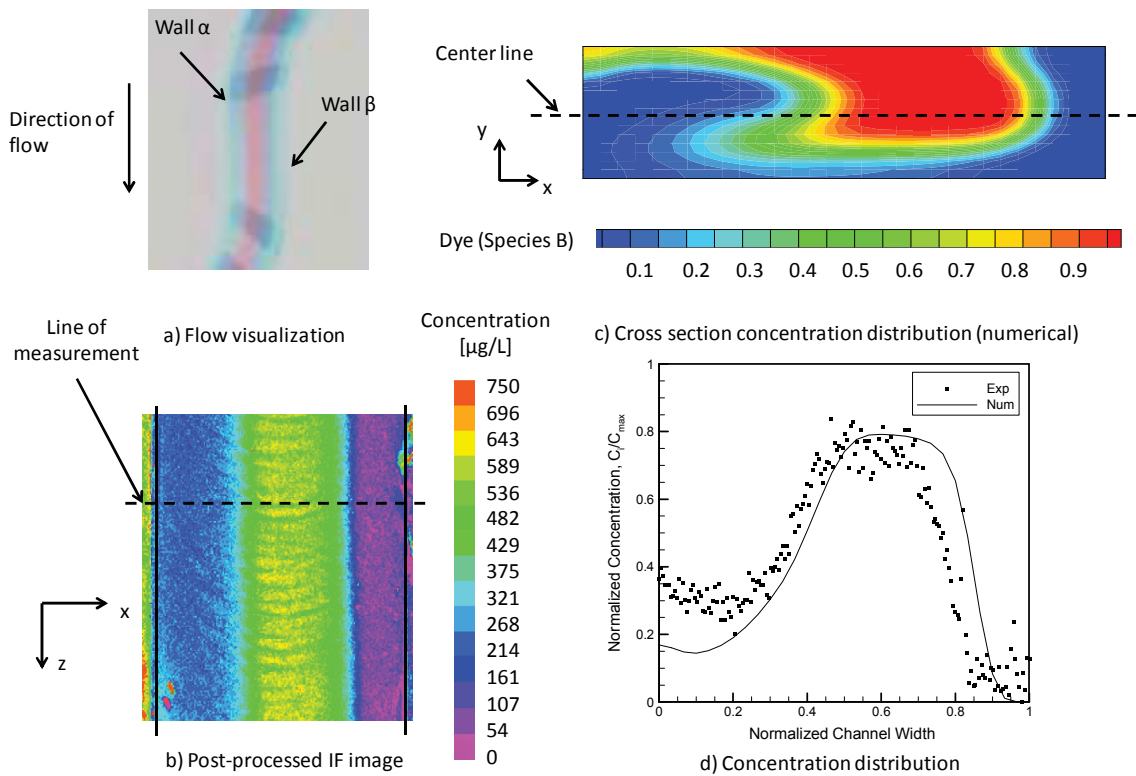
Figure 5.13: Species distribution at location L2 at Re = 10.

stacked fluids from well mixed regions. As shown in figure 5.13c, the striations observed

experimentally are not, in fact, separate fluid layers. Rather, species A has traveled

from wall α to the base of the channel, through the grooves, toward wall β. In

compensation, species B travels toward wall α. This rotation increases the interfacial

area available for diffusion. To allow for reasonable comparison with IF data, the

average concentration obtained numerically in the y-direction was taken at all x

locations. Figure 5.13d shows a comparison of numerical and IF experimental data, and

shows good agreement.

A similar data presentation is shown in figure 5.14 at Re = 50, where rotation is

stronger. Figure 5.14a shows the flow visualization image at L2, where multiple streams

of species A and B in varying concentrations are visible. The corresponding post

processed IF image is shown in figure 5.14b. An increase in the complexity of the flow

pattern is noted, and is further clarified by the numerically obtained cross section view.

The combination of Dean vortices and helical flow lead to significant rotation. The

appearance of striations in the experimental work is a result of regions occupying

primarily one species. In contrast to the species distribution at L2 at Re = 10, species B

primarily occupies the base of the channel. Comparison of numerical and experimental

results shows good agreement (figure 5.14d). The concentration distribution obtained

via IF at all investigated locations and Reynolds numbers is presented in Appendix B.

Wall α   Wall β

Center line

Direction of flow

y

x

Dye (Species B)

0.1 0.2 0.3 0.4 0.5 0.6 0.7 0.8 0.9

a) Flow visualization

c) Cross section concentration distribution (numerical)

Concentration [µg/L]

750
696
643
589
536
482
429
375
321
268
214
161
107
54
0

Line of measurement

x

z

b) Post-processed IF data

d) Concentration distribution
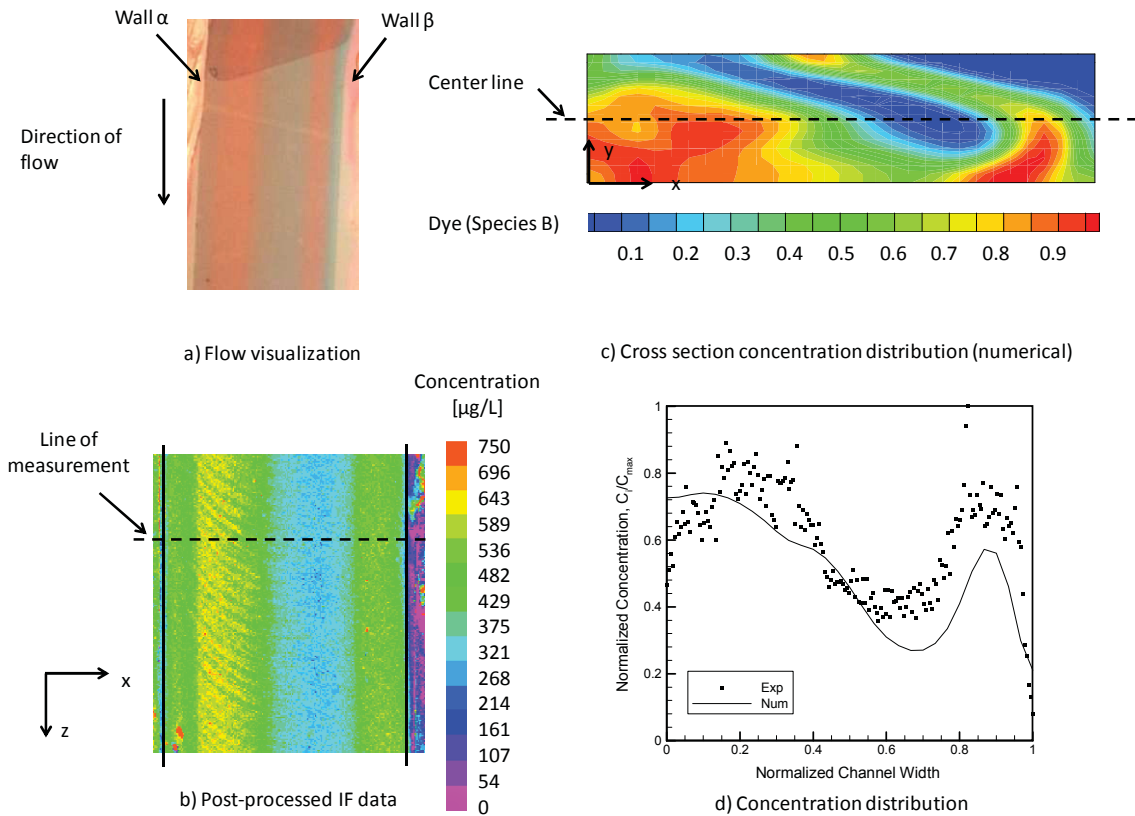
Figure 5.14: Species distribution at location L2 at Re = 50.

5.4.2 Quantitative Analysis

Figure 5.15 presents the numerically obtained variation in mixing index along the channel length, as described by equation 3.13, along the channel length for 0.5 ≤ Re ≤ 100. In computing the numerical mixing index, the concentration at each point in the x-y cross section is considered, allowing for increased accuracy. As shown, the highest degree of mixing, MI ≈ 0.90, is achieved at Re = 100. Repeated fluid overlap and strong rotation allow for increased species interfacial area, and improved mixing. Following Re = 100, Re = 50 and 0.5 offer extremely similar mixing performances, as do Re = 1 and 25.
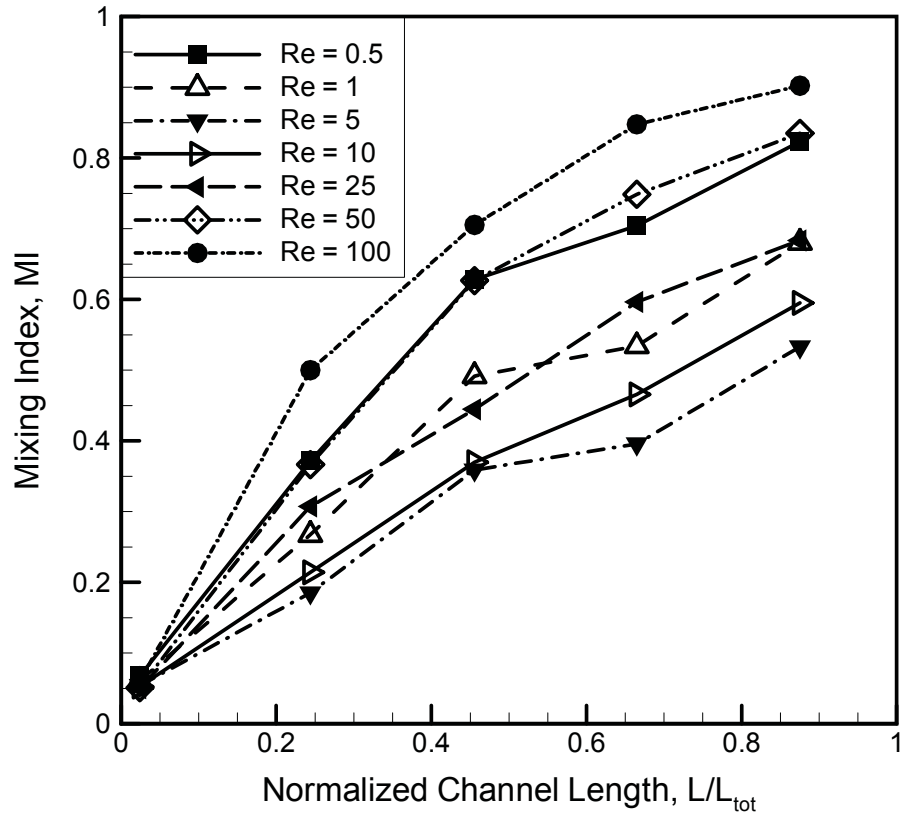
Figure 5.15: Numerically obtained variation in mixing index along channel length.

However, the dominant mixing mechanism differs; diffusion dominates at lower Re, whereas strong rotation promotes advection-dominant mixing at higher Re. This is clarified upon inspection of mixing performance at the outlet.

Figure 5.16 presents the mixing indices obtained from numerical and IF results at the outlet. A decreasing-increasing trend in mixing performance is noted with increasing Reynolds number. An inflection point is noted at Re = 5, which marks the transition from diffusion dominant mixing to advection dominant mixing. At lower Reynolds numbers, the residence time is high, and mass diffusion dominates. With increasing Reynolds numbers, strong rotation is observed, leading to an increase in the

interfacial area available for mass transfer. Note that while values above Re = 5 are considered to be advection dominant, mass diffusion across the rapidly increasing interfacial area remains crucial. At the outlet, the maximum error between numerically and experimentally obtained MI values is 7.32%. The error is computed by:

$$error = 100 \times \left| \frac{MI_{num} - MI_{exp}}{MI_{num}} \right| \tag{5.1}$$

where the MI_{num} and MI_{exp} denote numerically and experimentally obtained mixing indices, respectively.
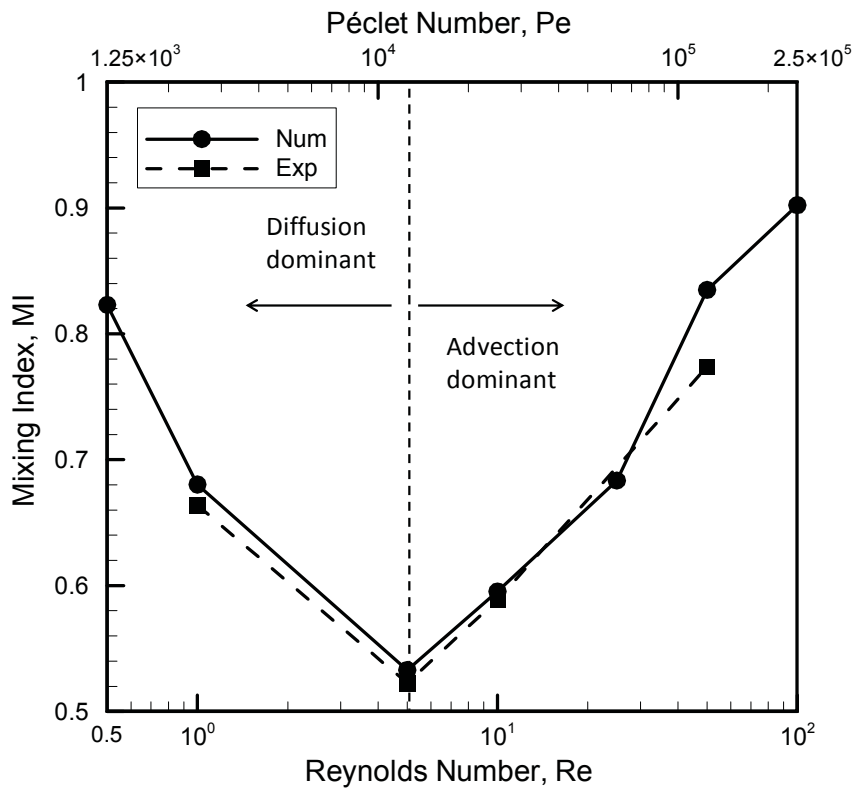
Figure 5.16: Numerically and experimentally obtained mixing indices at the outlet (L5).

5.5 Comparison of Device

Figure 5.17 shows the experimentally obtained mixing indices for several micromixers at similar equivalent lengths, as described in chapter 3.5. Note that only devices with similar operating ranges and equivalent lengths are included. Lu et al. (2010) proposed a four-inlet micromixer with four butterfly-shaped elements. To account for the total length, butterfly elements were assumed to be 120 μm × 120 μm squares, and the length of the pre-mixer was estimated based on figures. For consistency, the Reynolds numbers based on the main channel hydraulic diameter are presented in the figure. It is noted that their device exhibits increased mixing with increasing Reynolds number, as the fluid interface becomes distorted. The present device offers superior mixing in the lower Reynolds number range, however it is difficult to predict the difference in performance at Re > 50, as the design of Lu et al. operates on a slightly smaller footprint area. Ansari et al. (2010) proposed a T-inlet mixer based on uneven fluid collisions which operates most effectively at higher Reynolds numbers. It is noted that the present mixer provides a higher degree of mixing at Re ≈ 50 in a shorter channel length. For comparison with a scaled up device, the cross-omega mixer (Fan 2009) is included. While a decreasing-increasing trend is also noted in this device, signifying the transition from mass diffusion dominance to mass advection dominance, higher degrees of mixing are achieved in the present device at a shorter equivalent length.
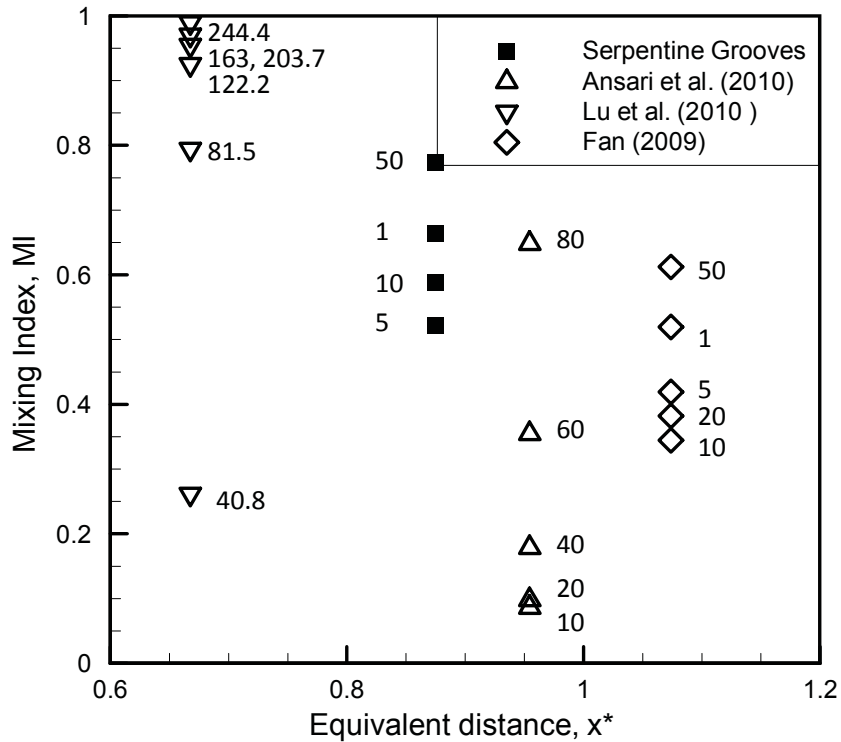
Figure 5.17: Mixing indices of various micromixers at similar equivalent lengths. Numbers next to data points indicate Reynolds number.

The present mixer shows a high degree of mixing compared to several recently proposed devices at similar equivalent lengths. Fluid rotation and overlap is credited with increasing the interfacial area available for mass transfer at higher Re, whereas mass diffusion dominates at lower Re.

5.6 Summary

A passive micromixer based on fluid rotation was designed, fabricated and tested over $0.5 \leq Re \leq 100$. Slanted grooves were applied to a four-element serpentine channel to promote flow rotation over a wide range of Reynolds numbers. Flow visualization was used to qualitatively assess flow patterns, while induced fluorescence was used to provide quantitative concentration distribution data. Numerical

simulations provided further clarification regarding the complex nature of the species distribution. Good agreement was reported between experimental and numerical results. Flow rotation was observed at all investigated Re, and the degree of rotation increased with increasing Re. At all investigated Reynolds numbers, grooves produced helical flow and guided species from one wall to the other. Beyond Re ≥ 50, the formation of Dean vortices was observed as a result of the serpentine channel. A decreasing-increasing trend in mixing efficiency was observed as the dominant mixing mechanism changed from mass diffusion to mass advection, with a critical Reynolds number of Re = 5. Oscillations resulting from the use of two separate syringe pumps and a Y-type inlet rendered IF experimental measurements inaccurate at Re = 0.5 and 100. The highest mixing index, MI_{num} = 0.90, was reported at Re = 100 where a high degree of fluid overlap was observed. A mixing index of MI_{num} = 0.82 was reported at Re = 0.5, where diffusion dominates.

Chapter 6

Micromixer with Groove-Enhanced Division

Elements

The investigation of the groove-enhanced serpentine micromixer has shown that the application of grooves in a curved channel promotes considerable flow rotation over a range of Reynolds numbers. Additionally, the application of an interdigital inlet allowed for enhanced mixing by reducing the path of diffusion and increasing the species interfacial area. Thus, a novel micromixer incorporating these geometric enhancements is proposed and evaluated over $0.5 \leq Re \leq 100$ ($0.15 \leq K \leq 30.15$). In the groove enhanced division element mixer, flow visualization is applied to qualitatively assess mixing and flow patterns along the entire channel length, while micro-induced fluorescence is applied to quantitatively assess concentration distribution. As the aforementioned experimental techniques are limited by their two-dimensional nature, numerical simulations are applied to describe three-dimensional flow rotation. Numerical results are validated by experimental data.

6.1 Test Section

6.1.1 Design and Principle of Operation

Increasing the species interfacial area enhances mixing by allowing for increased mass diffusion. Creating helical motion in fluid not only increases surface area, but reduces the path of diffusion by reducing species thickness. At lower Reynolds numbers, grooves along the channel surface have been shown to induce helical flow as a result of an anisotropic pressure gradient. At higher Reynolds numbers, curved channels promote flow rotation in the form of Dean vortices as a result of increased fluid momentum. The proposed micromixer combines these geometric concepts to promote flow rotation over a wide range of Reynolds numbers.
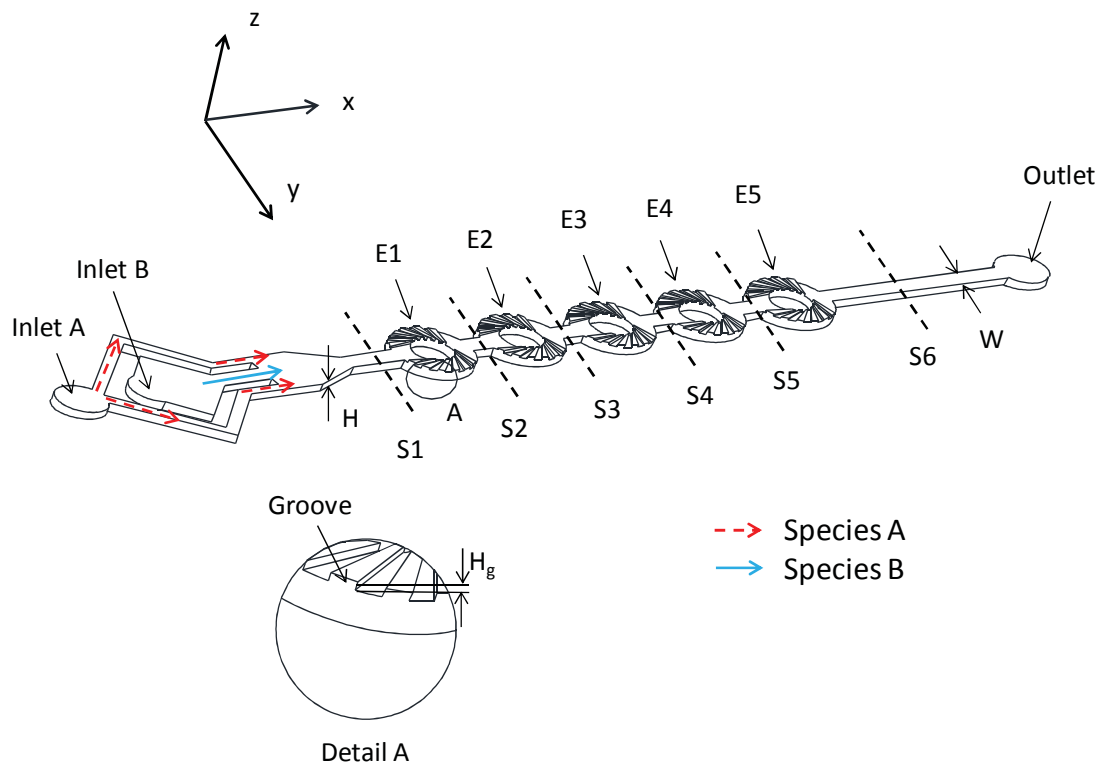
Figure 6.1: Three-dimensional view of fluid domain indicating locations of measurement.

Figure 6.1 presents the 3-dimensional view of the mixer. To reduce the path of diffusion and increase species interfacial area, two species, A and B, are supplied to the test section via a simple interdigital type inlet, which was previously shown to reduce the occurrence of oscillations. Species A is divided into two substreams, producing a total of three lamellae. Prior to entering the main mixing channel, species are converged slightly to further reduce the path of diffusion. This also creates a fluid velocity component along the path of diffusion. A total of five equidistant mixing

H	0.75 mm
H_g	0.25 mm
W_A	1.0 mm
W_B	2.0 mm
W	2.0 mm
L	82.0 mm
s	2.25 mm
L_{out}	19.5 mm
R_{in}	2 mm
R_{out}	4 mm
φ	20°
ω	30°
ϕ	40°
θ	25°
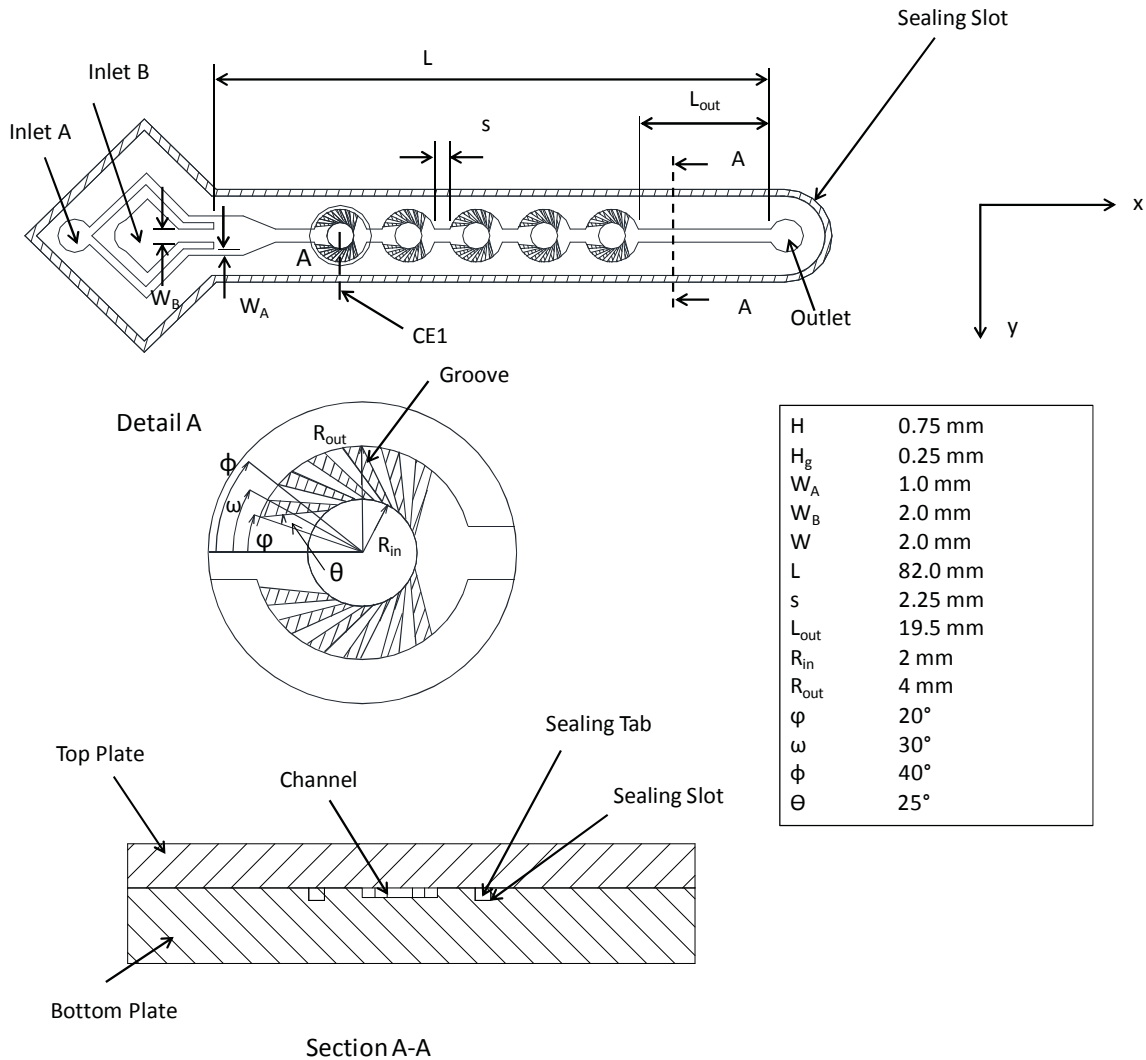
Figure 6.2: Dimensions of test section.

elements, which serve to divide and recombine the flow, are located along the channel length. Each semi-circular sub-channel contains six equally spaced slanted grooves. The grooves promote helical flow, and at higher Re, the semi circular curved channels produce Dean vortices. As shown in figure 6.2, the width of each substream of species A, W_A, is 1.00 mm, and the width of species B, W_B, is 2.00 mm. The channel depth, H, is 0.75 mm, the main channel width, W, is 2.00 mm and the depth of the grooves, H_g, is 0.25 mm. The inner radius of curvature of the dividing element, R_{in}, is 2.00 mm, and the outer radius of curvature, R_{out}, is 4.00 mm. The linear mixing length of the device is 82 mm. The total mixing length, taking the length of each element to be $2 \cdot \pi \cdot R$, where $R = (R_{in}+R_{out})/2$, is approximately 137.5 mm.

6.1.2 Fabrication

The device, shown in figure 6.3, was fabricated in cast acrylic using CNC micro-machining. To obtain a flat, level surface, the mating surfaces of the top and bottom plates were polished. A sealing slot and tab were machined around the perimeter of the test section. To assemble the mixer, thread seal tape, which prevents leakage, was placed within the sealing slot of the bottom plate, and the top plate was pressed onto the bottom plate. Thin metal clips were placed along the perimeter of device. The high pressure drop resulting from the slot and tab prevented leakage around the perimeter of the mixer. The mixer was easily disassembled for cleaning by running a pin along the perimeter of the mixer and gently opening the device.
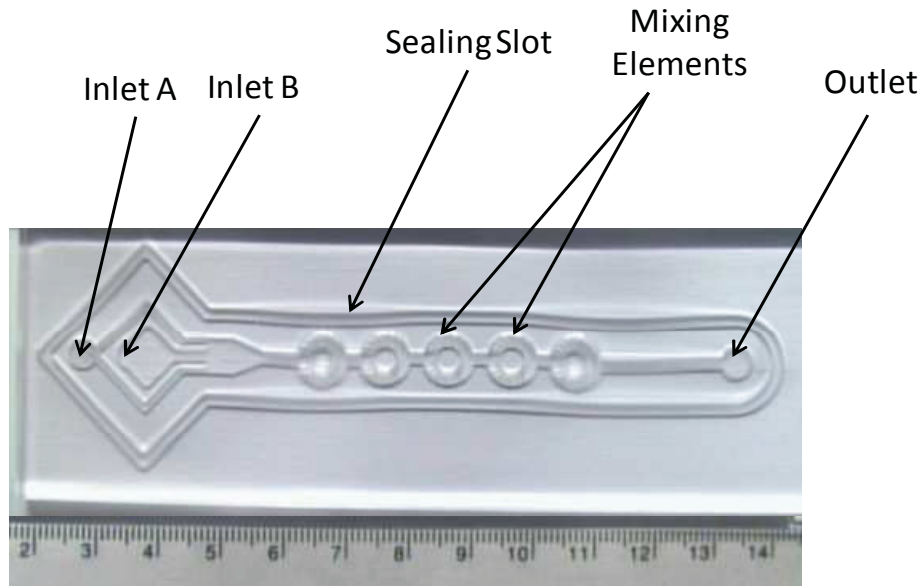
Figure 6.3: Bottom layer of manufactured test section.

6.2 Numerical Analysis

To aid in describing the highly rotational flow fields in the mixer, numerical simulations were conducted. Owing to symmetry about the x-z, simulations were conducted on half the mixer. The grid system used is shown in figure 6.4. In the x-y plane, quadrilateral grids were applied to the straight segments of the mixer and the grooved sub-channels, while triangular grids were applied in curved portions between the latter two regions. Refined grids were used in the groove-enhanced areas, as flow was expected to be more complex. The model's volume was created by extending the x-y plane vertically in the z-direction. To reduce computational time, grid independence was performed at Re = 100 on a half of a single mixing element along with the inlet to determine the appropriate grid system. The boundary conditions and solution methods
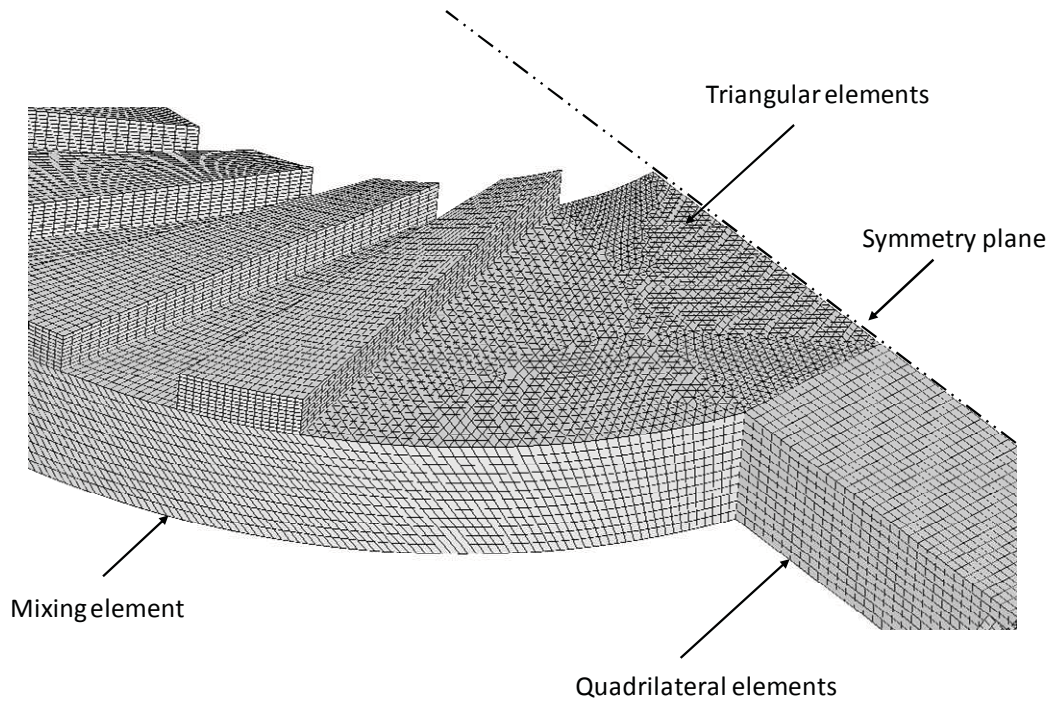
Figure 6.4: Grid system used in simulation.

applied for grid independence were the same as those described in chapter 3.4. Figure 6.5 presents the normalized concentration distribution and the velocity distribution along the normalized half-channel width for a variety of grid numbers. The grid distribution resulting in 0.25 M grids for half of a single mixing element and inlet structure was determined as optimal; increasing the number of grids beyond this value resulted in negligible variations in concentration and velocity distribution, as shown in the figure. This mesh size was then selected to model the entire half-mixer, where the total number of elements was 1.0 M.
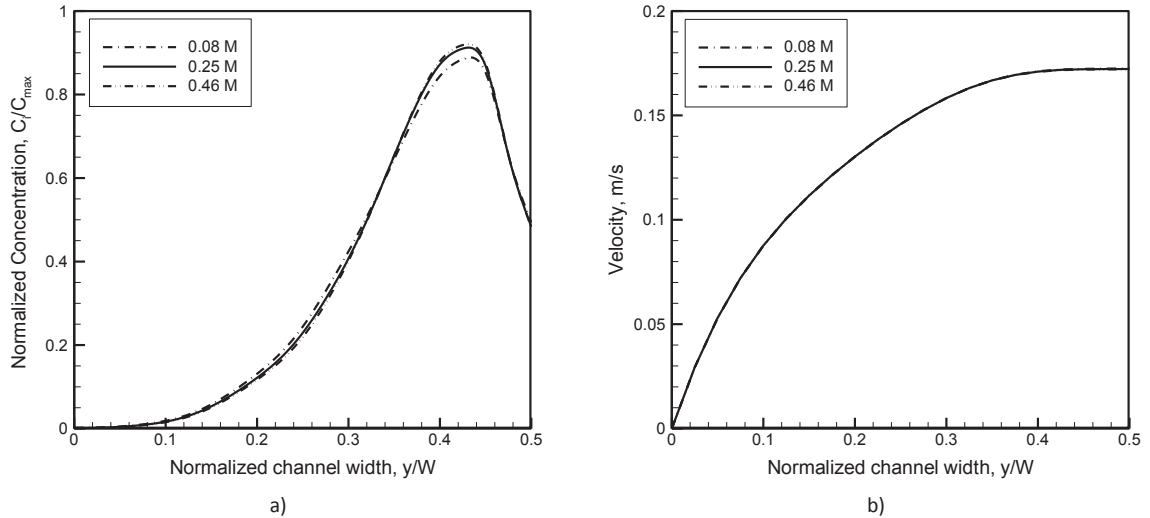
Figure 6.5: Grid independence performed at outlet of first mixing element a) concentration distribution and b) velocity distribution

6.3 Validation of Numerical Results

As numerical simulations are used to assist in the description of the mixing phenomena and flow patterns in the mixer, it is first essential to validate the numerical work against experimentally obtained data. Note that the Reynolds number is based on the total velocity and hydraulic diameter of the main channel, whereas the Dean number is based on the hydraulic diameter and Reynolds number of the semicircular sub-channel and the mean radius of curvature.

To quantitatively compare experimental and numerical results, IF data is compared to numerically obtained results. Induced fluorescence experiments are carried out under the *bino* mode at a magnification of 4 ×, with a re-sampled image size of approximately 8 μm/pixel. A sample calibration curve used for the evaluation of this mixer is shown in figure 6.6. The maximum error associated with this calibration curve, as described by equation 4.3, is 1.49 %.
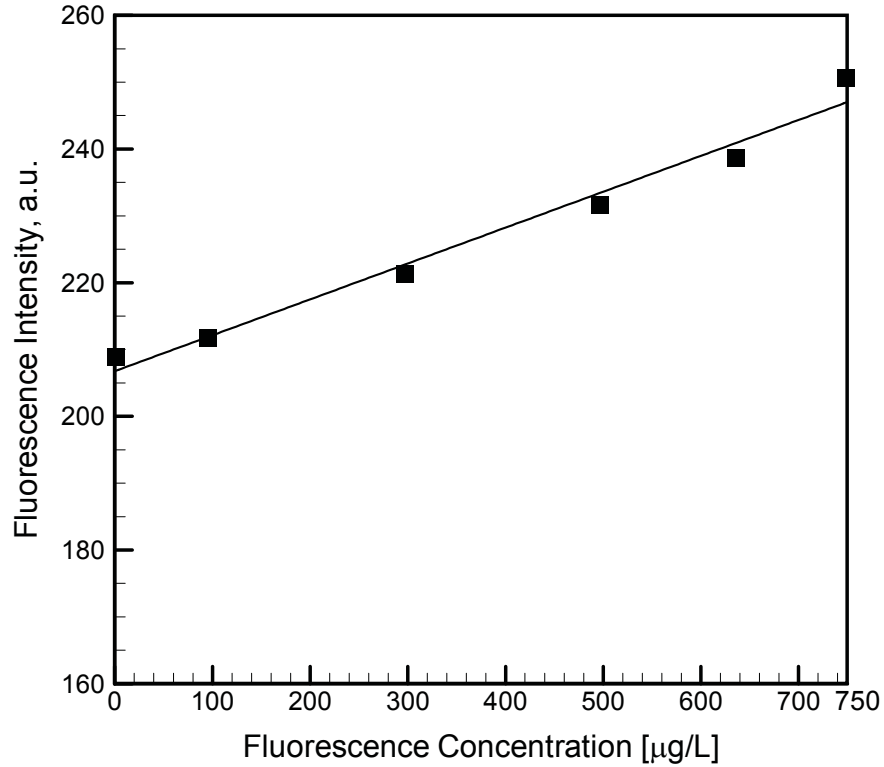
Figure 6.6: Sample calibration curve

The normalized concentration distribution in the vicinity of the first mixing element is presented along the normalized channel width in figure 6.7 for Re = 0.5 and 50. For consistency in comparing numerically obtained data with data obtained through IF, the average concentration in the z-direction was taken. Data is presented in the vicinity of the first mixing element (E1), where concentration gradients are highest, allowing for lamellae to be easily distinguished. As shown, the numerical and experimental concentration distributions offer very good agreement at low Reynolds numbers (Re = 0.5, K ≈ 0.15) as well as at the inlet. At higher Re (Re = 50, K ≈ 15.1), where momentum becomes important, a slight asymmetry in concentration distribution
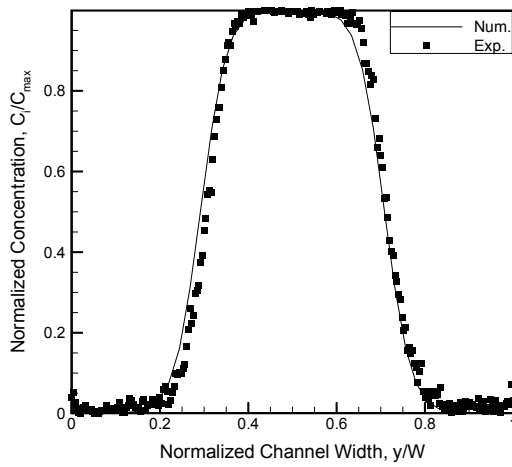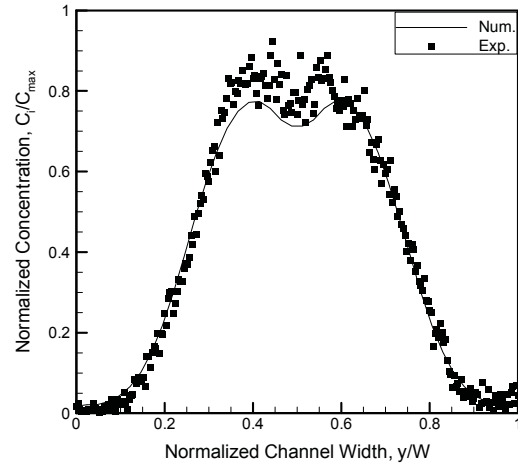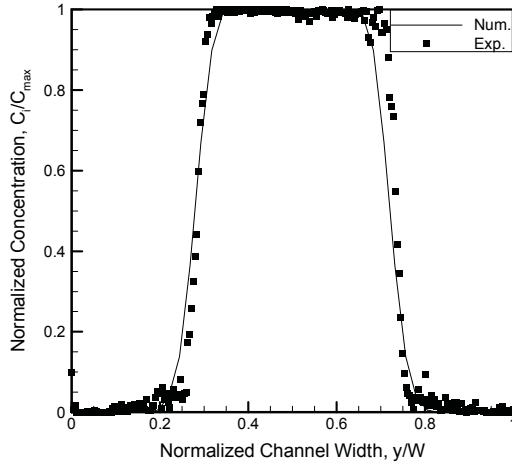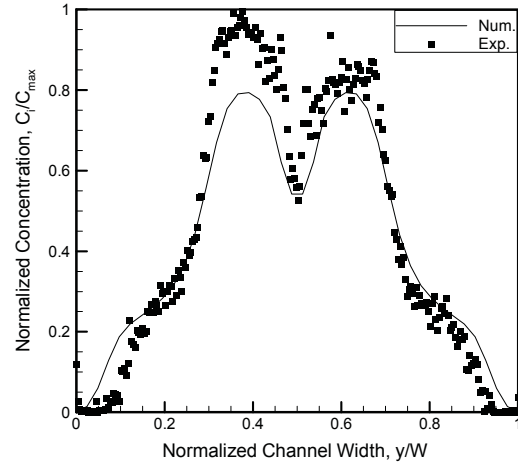
Figure 6.7: Numerically and experimentally (IF) obtained concentration distribution at Re = 0.5 and 50 at the inlet (S1) and exit (S2) of the first mixing element.

is noted (figure 6.7) as a result of a slight manufacturing defect. An image of the test section (figure 6.8), taken at 2 × magnification with a re-sampled resolution of approximately 16.6 μm/pixel, shows that the sidewall on the left side of the device is approximately 160 μm higher than that on the right.

The defect, however, does not prevent reasonable comparison between experimental and numerical results. To qualitatively compare flow visualization and numerical simulation results, figure 6.9 presents the first mixing element, E1, at Re = 100. The first mixing element was chosen due to the high degree of contrast between species. Very good agreement is observed; locations A and B show a portion of species B in the first groove, whereas locations D and E show the apparent formation of additional lamellae. Location C in the flow visualization image shows a region of apparently well mixed fluid. However, inspection of the cross section of the channel (figure 6.9c) shows that this is a result of fluid overlap rather than mixing.
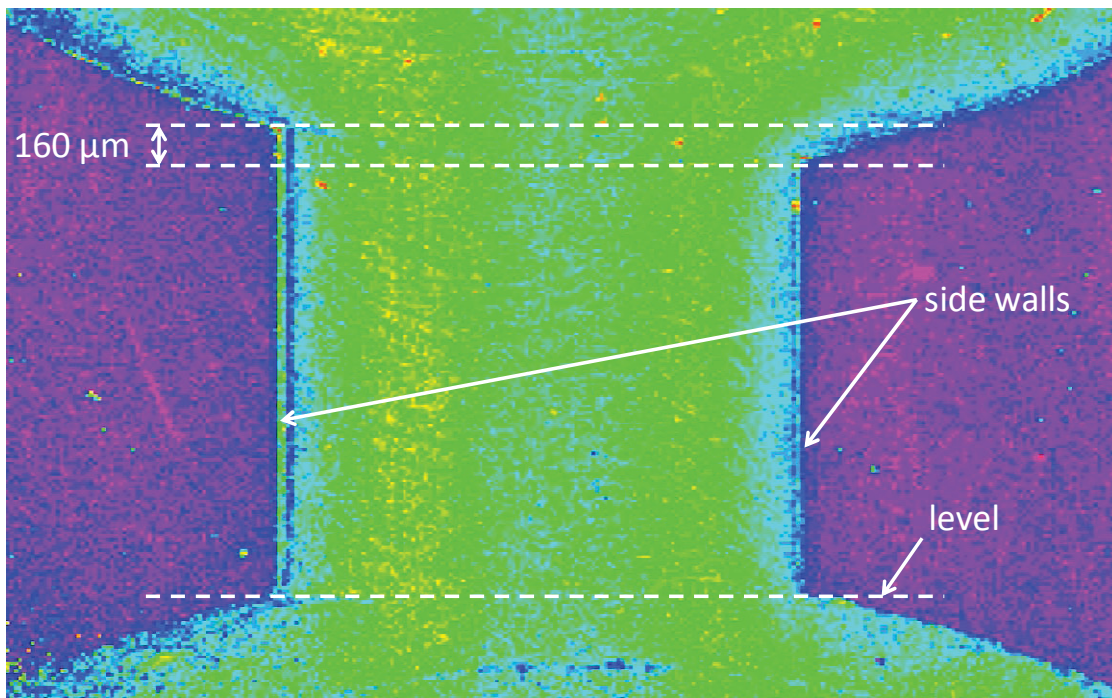
Figure 6.8: Slight asymmetry in manufactured device.
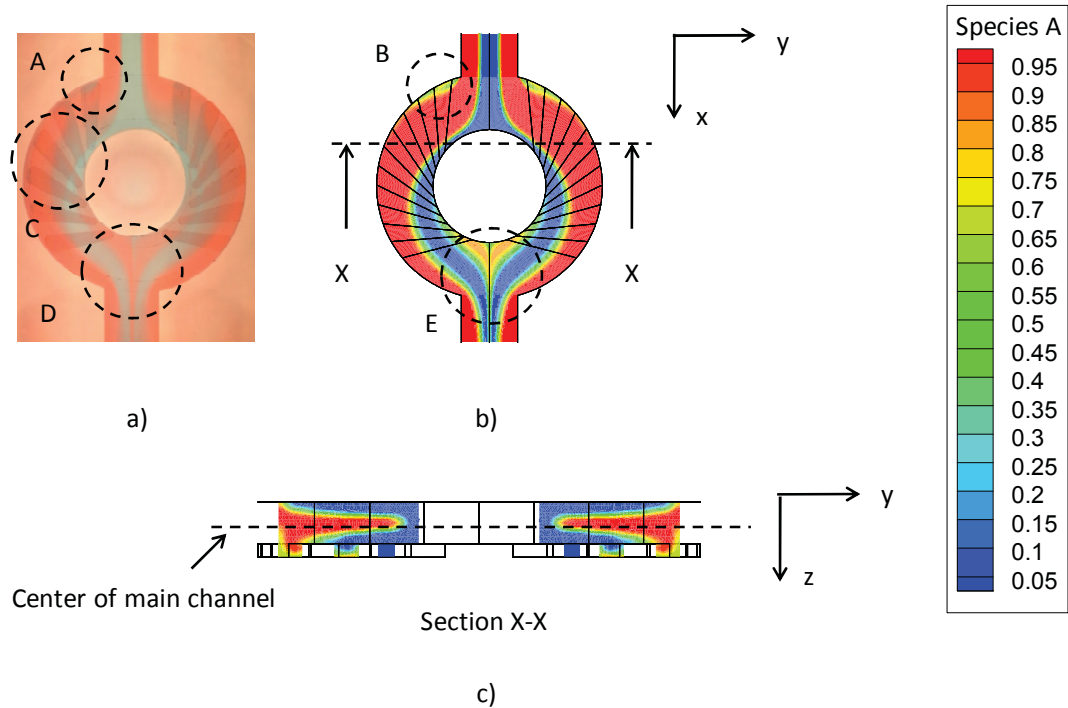
Figure 6.9: Comparison of E1 at Re = 100. a) flow visualization image b) concentration distribution along center of channel c) section view of mixing element

It is worth noting that the average concentration at S1 is less than 0.5, as shown in figure 6.7. This is a result of the velocity distribution within the channel. The velocity of fluid at the walls is zero (no-slip), whereas the fluid velocity increases toward the center of the channel, as shown in figure 6.10. A viscous drag is exerted on the fluid layers, causing a velocity distribution. According to the conservation of mass,

$$\dot{m} = \rho A U = constant \tag{6.1}$$

where *A* is the cross section area, the lamella thickness (or cross sectional area) of the center lamella must decrease slightly to account for the increased velocity at the center of the channel. This reduction in center lamella thickness leads to an average
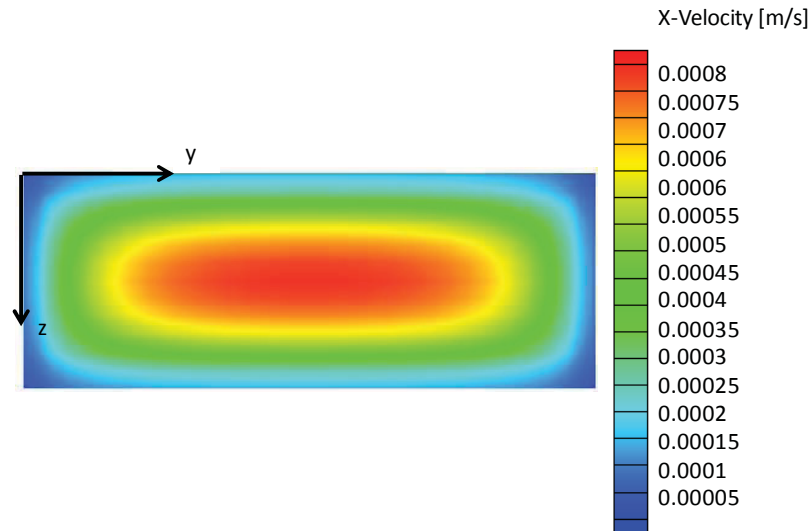
Figure 6.10: Cross section velocity distribution at S1 at Re = 0.5.

concentration of less than 0.5. Further along the channel, as fluid rotation causes a reversal in species location, the average cross section concentration is slightly higher than 0.5.

6.4 Species Distribution and Flow Phenomena

6.4.1 Qualitative Analysis

Figure 6.11 presents the flow visualization images along the channel length for $0.5 \leq Re \leq 100$. At the inlet, three distinct lamellae are noted at all Reynolds numbers. At low Reynolds numbers (Re = 0.5 and 1), the onset of molecular diffusion is evidenced by the blurred species interface, as shown by location A, for example. Location B shows a region of seemingly well mixed fluid. However, as previously described by figure 6.9, this is a result of fluid overlap and rotation. Location B also shows a portion of species B
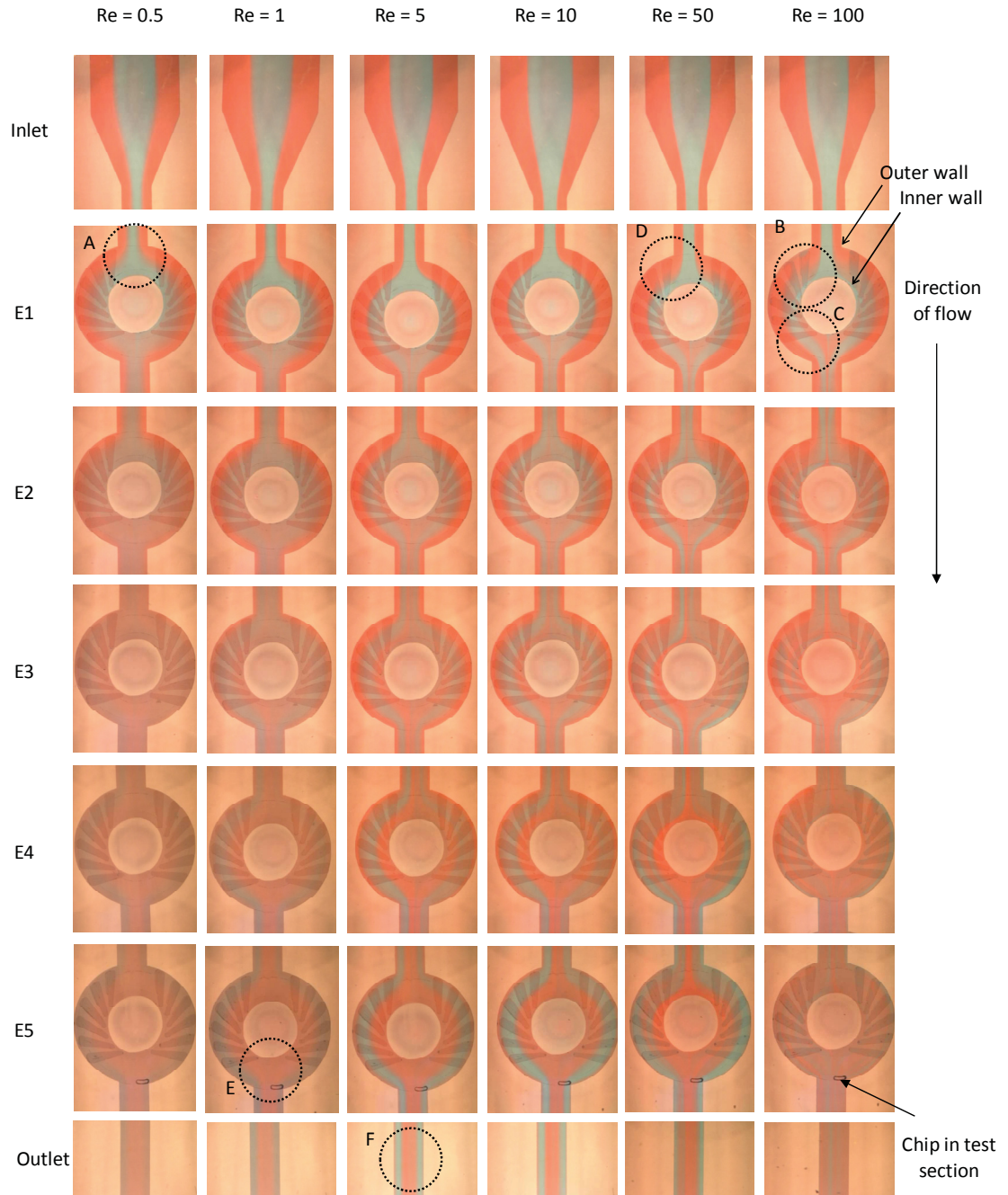
Figure 6.11: Flow visualization over $0.5 \leq Re \leq 100$.

in contact with the sidewall. A similar trend is observed at location D, though to a lesser extent, as the degree of fluid rotation increases with increasing Re. The high degree of curvature in that region forces species A (red) toward the center of the channel, while species B (blue) is forced toward the top and bottom portions of the channel as a result of fluid momentum. Additional striations form in the center of the channel (location C) as a result of the joining of the highly rotational fluids from the substreams. At the outlet, evidence of flow rotation is clear. Locations E and F, for example, show the complete reversal of species location. Species A shifted from the sidewalls to the center of the channel.

Figure 6.12 presents sample IF images at S1, S3 and S6 at Re = 0.5, 10 and 100. In agreement with flow visualization images, the onset of mass diffusion is evident at the inlet (S1) at Re = 0.5, owing to the high residence time of the fluids (location A). Location B presents the formation of additional lamellae at the center of the channel, as a result of rotating substreams. Location C shows the complete reversal of species as a result of fluid rotation. At Re = 10, it is clear that the degree of mixing appears quite low. At the outlet (S6), Re = 0.5 and Re = 100 appear to offer relatively uniform concentration distribution, indicating good mixing. However, the mass transfer mechanisms differ considerably. The concentration distribution data obtained over 0.5 ≤ Re ≤ 100 at all six measurement locations is presented in Appendix C.

To demonstrate the rotation over 0.5 ≤ Re ≤ 100, figure 6.13 presents the concentration iso-surfaces in the first mixing element, E1. At all Reynolds numbers, the
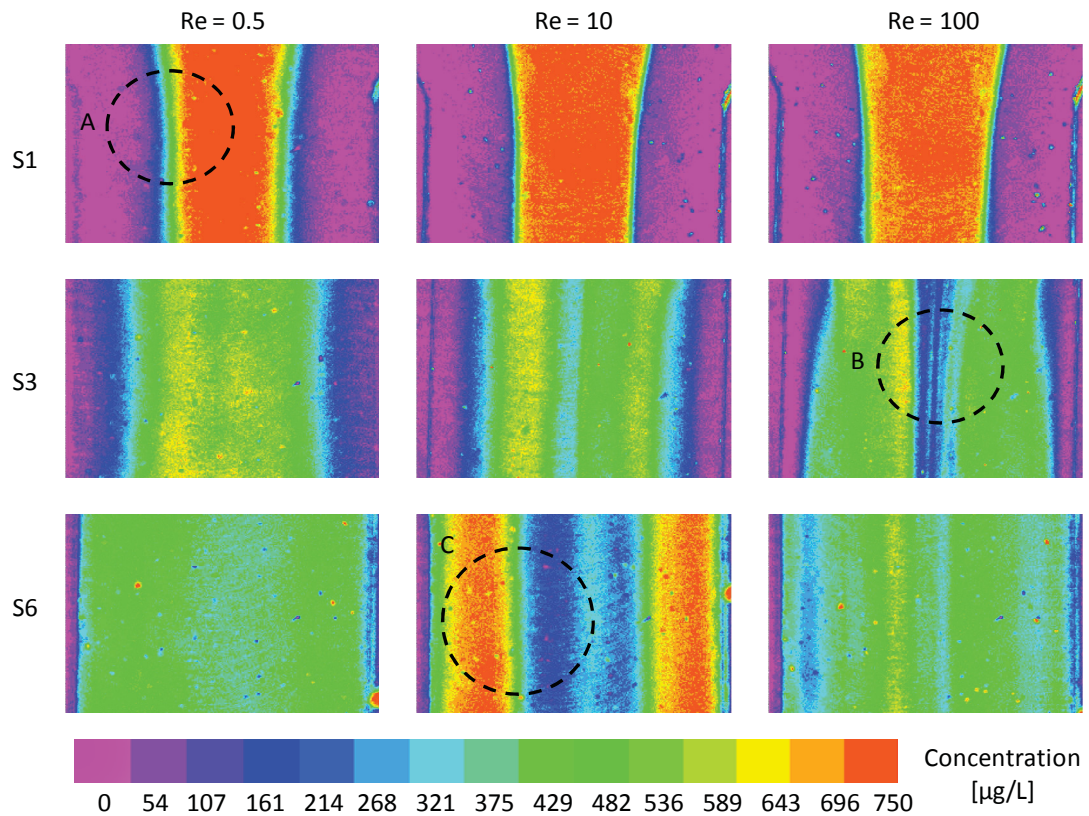
Figure 6.12: Induced fluorescence images at the inlet (S1), center (S3) and outlet (S6) of the mixer.

lamellae are vertically aligned at the inlet, and undergo rotation upon entering the first mixing element. The onset of species rotation at Re = 0.5 is shown by location A, whereby low concentration species in contact with the side wall is rotated toward the grooved surface, and occupies the grooves. The degree of fluid rotation may be qualitatively judged by the quantity of low concentration solution in contact with the grooved surface. As shown in figure 6.13, the degree of fluid overlap increases with increasing Reynolds number. Location B shows a region of well mixed fluid exiting the
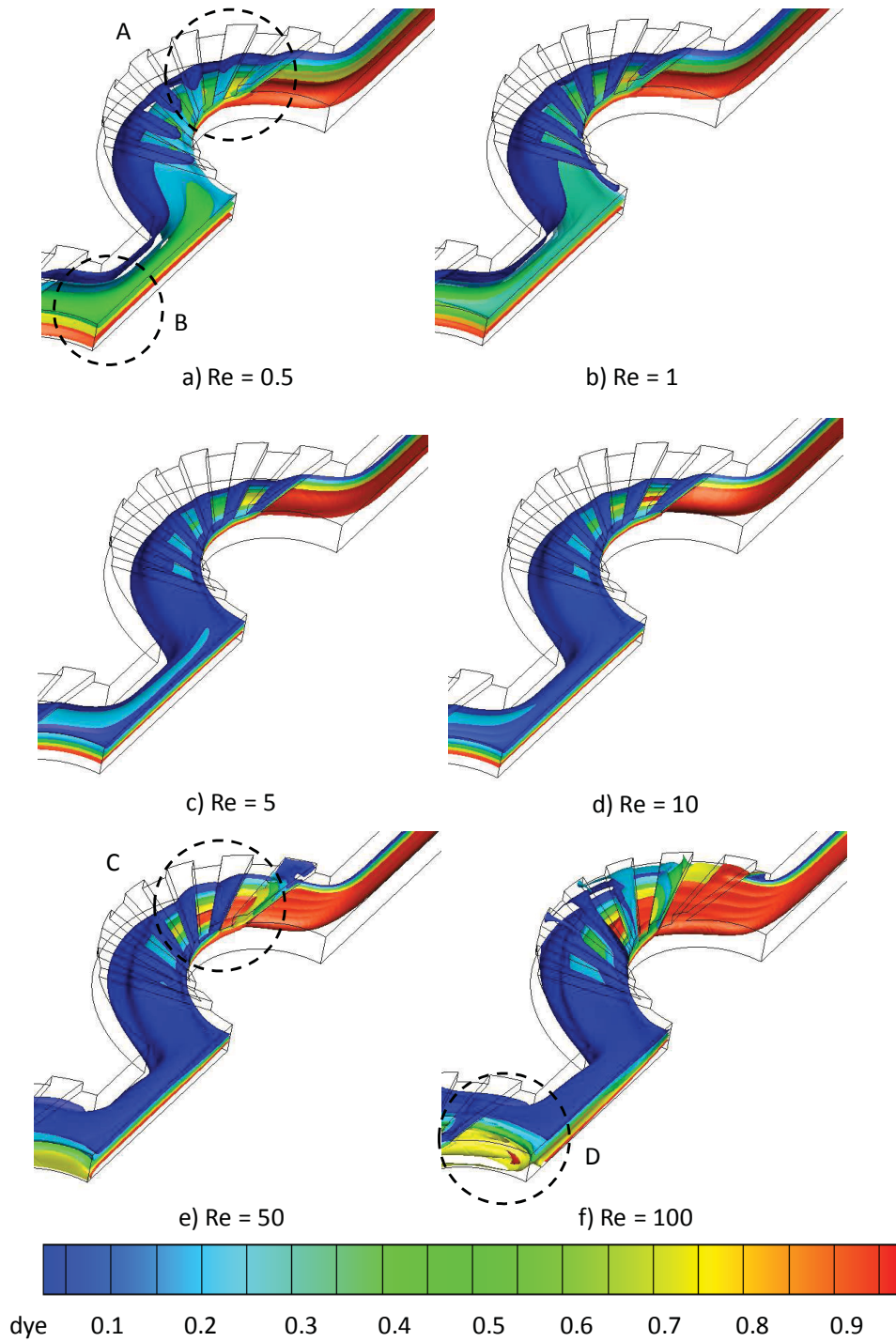
Figure 6.13 : Concentration iso-surfaces at the first mixing element over 0.5 ≤ Re ≤ 100.

first element, as well as a reduced amount of distinguishable low concentration species. This is a result of the increased residence time, allowing for increased mass diffusion. Increasingly larger regions of low concentration species remain visible with increasing Reynolds number, as a result of the reduction of residence time allowing for mass diffusion. At Re > 50, a discernible change in rotation is noted at the entrance of the first mixing element. Locations C and D show a high degree of fluid rotation resulting from not only the grooves, but also from the curved channel shape. To further exhibit the effect of the grooves on flow through E1, figure 6.14 shows the concentration-coded streamlines at Re = 0.5 and Re = 100. At Re = 0.5, low concentration solution is guided from the outer wall toward the inner wall as a result the pressure variation caused by the grooved structures. A similar phenomenon is observed at Re = 100, however greater fluid rotation is noted. In the first groove, location A presents a high degree of fluid rotation, where high concentration fluid is directed from the center of the channel toward the outer wall. The resultant increase in interfacial area results in enhanced mixing.

To demonstrate the flow patterns within a mixing element, figure 6.15 shows the streamlines superimposed on the species distribution contours in the center of the first mixing element, as shown by CE1 in figure 6.2. As shown, similar concentration distributions and streamlines are observed over $0.5 \leq Re \leq 10$. At Re = 50 (K ≈ 15.1), the formation of a pair of counter-rotating vortices, or Dean vortices, is observed as a result of the curved sub-channel. A similar phenomena is observed at Re = 100 (K ≈ 30.15), though to a greater extent. Fluid in the center of the channel has a higher momentum

118

a) Re = 0.5

b) Re = 100
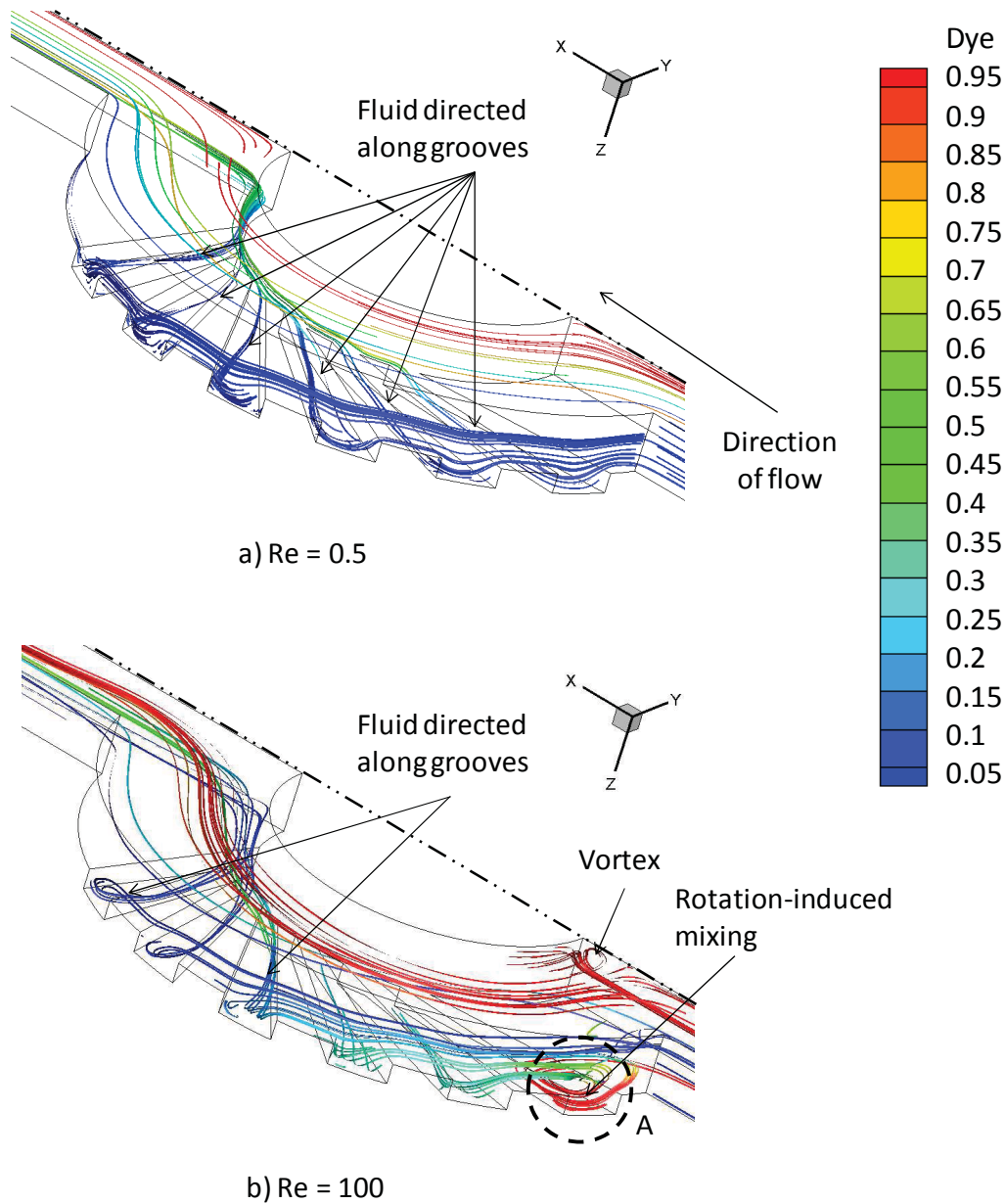
Figure 6.14: Concentration-coded streamlines at E1.

than fluid at the side walls. Thus, upon entering the curved channel, fluid at the center

of the channel is forced toward the outer wall, while fluid at the outer wall is displaced

in compensation. While the Dean numbers in the present investigation are quite low (K

$\approx$ 15 at Re = 50, Pe $\approx$ 1.25 $\times$ 10^5; K $\approx$ 30.15 at Re = 100, Pe $\approx$ 2.5 $\times$ 10^5), the formation of
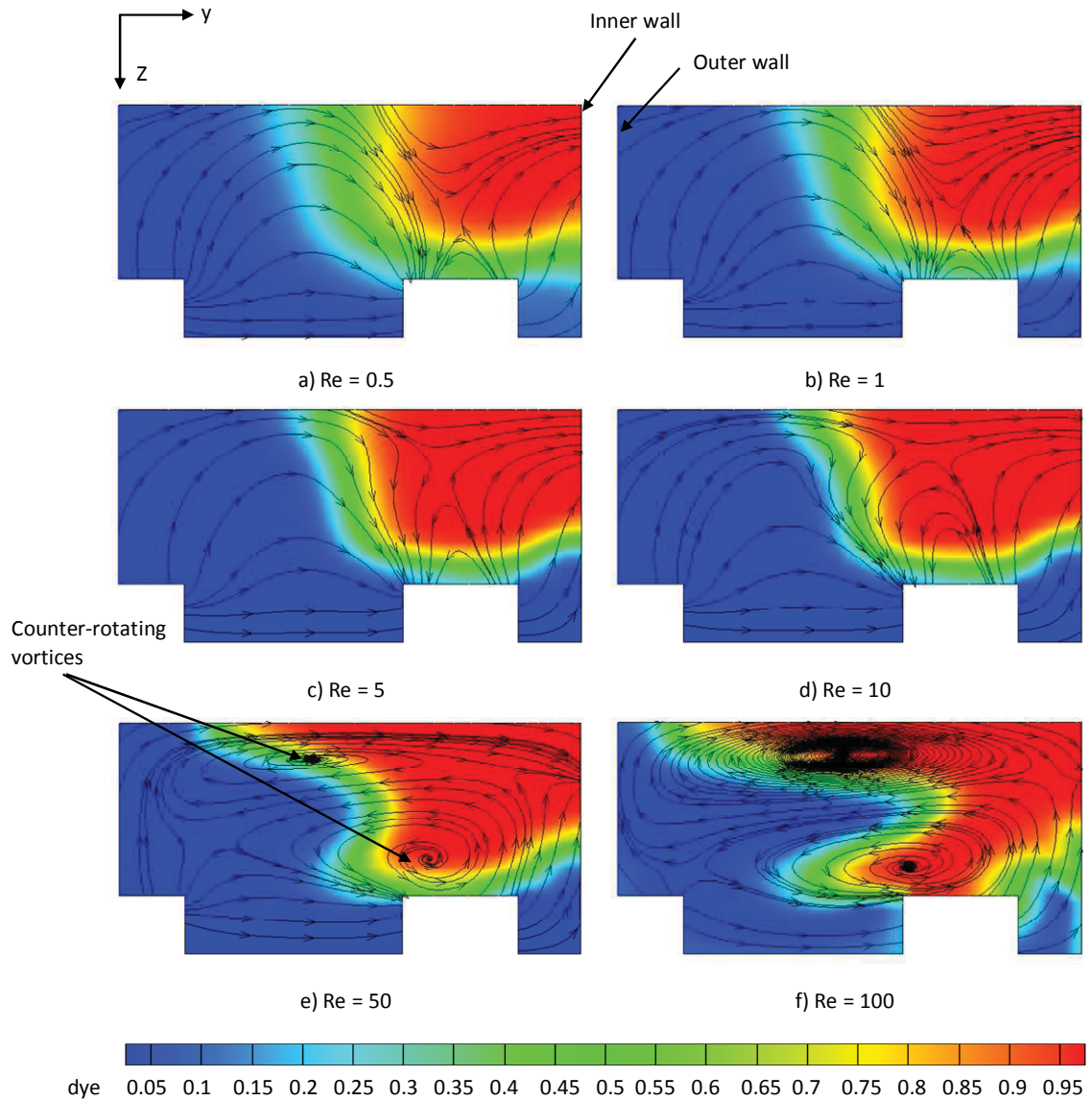
Figure 6.15: Concentration distribution and streamlines at the center of the first mixing element

Dean vortices has been reported by researchers at similar values. Jiang et al. (2004), for example, reported a curved interface at K = 10. At K ≈ 8, Howell et al (2004) reported a shift in the position of fluids in contact with the inner and outer walls in a curved channel. They also reported fluid stripes at Re = 30 (K ≈ 15.1) due to formation of

whorls and fluids folding into one another. At a Péclet number of Pe $\approx 2.5 \times 10^5$, Stroock et al. (2002) reported helical flow in their straight groove micromixer. In the present device, fluid rotation at higher Reynolds numbers is due to the combination of both Dean vortices and groove-induced helical flow.

In typical curved channels, the centers of the counter rotating vortices are aligned in the vertical direction. However, as a result of the grooves located on the bottom surface of the channel, an offset in the center of the vortices is observed in figure 6.15. At Re = 50 and 100, the formation of Dean vortices leads to an increase in species interfacial area, and thus an increase in the surface area available for mass transfer. It is worth noting that the vertical distance between the center of vortices decreases with increasing Re (figure 6.15 e and f). The spatial position of the vortices beings to more closely resemble positioning observed in a typical curved channel. The absence of Dean vortices at lower Re (Re < 10) demonstrates the ability of grooves to enhance mixing and promote flow rotation.

Figure 6.16 presents the concentration distributions obtained numerically and through induced fluorescence at S3 at Re = 50 (K = 15.1). The cross section of the channel is presented figure 6.16a, where the streamlines are superimposed on the concentration map. Two pairs of counter rotating vortices are clearly noted – each pair is a result of the curved sub-channel. The presence of four counter-rotating vortices is thus observed at values considerably lower than the critical Dean number (K $\approx$ 140). In the absence of the grooves (straight channel portions), the vortex cores become

vertically aligned. To compare with IF data, figure 6.16b presents the concentration distribution along the channel length. Results show good agreement, particularly on the right side of the channel. Fluorescence results on the left side of the channel were slightly skewed by the aforementioned defect.
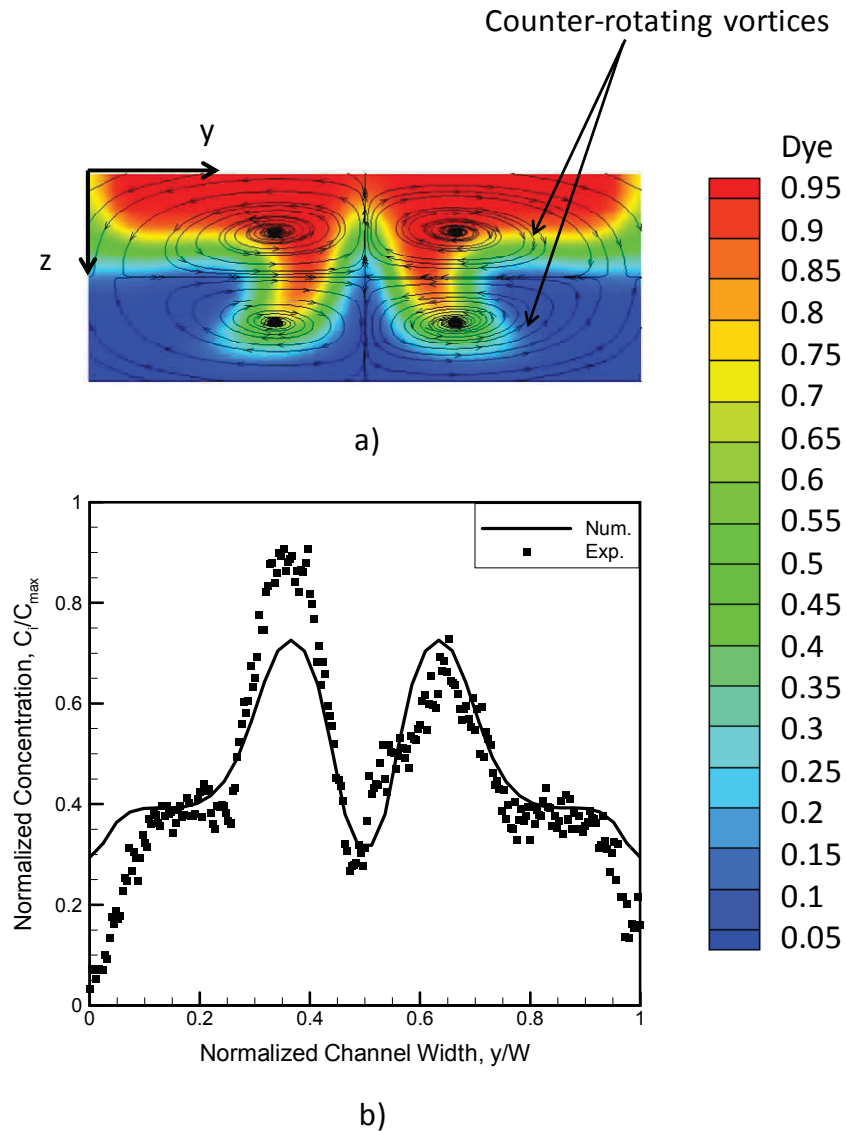
Figure 6.16: Re = 50, S3 a) cross-section streamlines and concentration distribution b) IF concentration distribution.

6.4.2 Quantitative Analysis: Mixing Performance

Figure 6.17 shows the numerically obtained variation in mixing index along the channel length. As shown in the figure, the highest degree of mixing occurs at Re = 0.5, followed by Re = 100. The steep gradients represent a higher rate of mixing due to diffusion at Re = 0.5 and vortex formation at Re = 100. A decrease in the rate of mixing from S5 to S6, is particularly notable at Re = 0.5 and Re = 100, where the concentration gradient is decreased. Figure 6.18 presents the concentration distribution at the outlet (S6) over $0.5 \leq Re \leq 100$. From this figure, it is clear that the most complete mixing
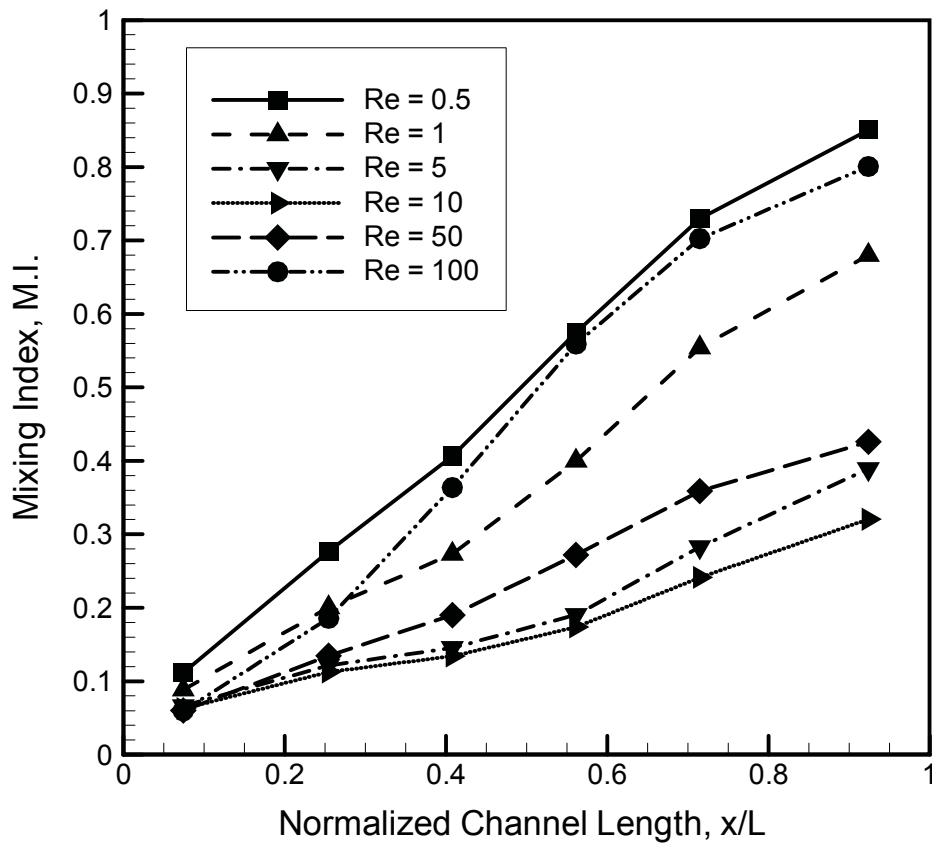
Figure 6.17: Variation in mixing index along normalized channel length at select measurement locations, S1-S6.
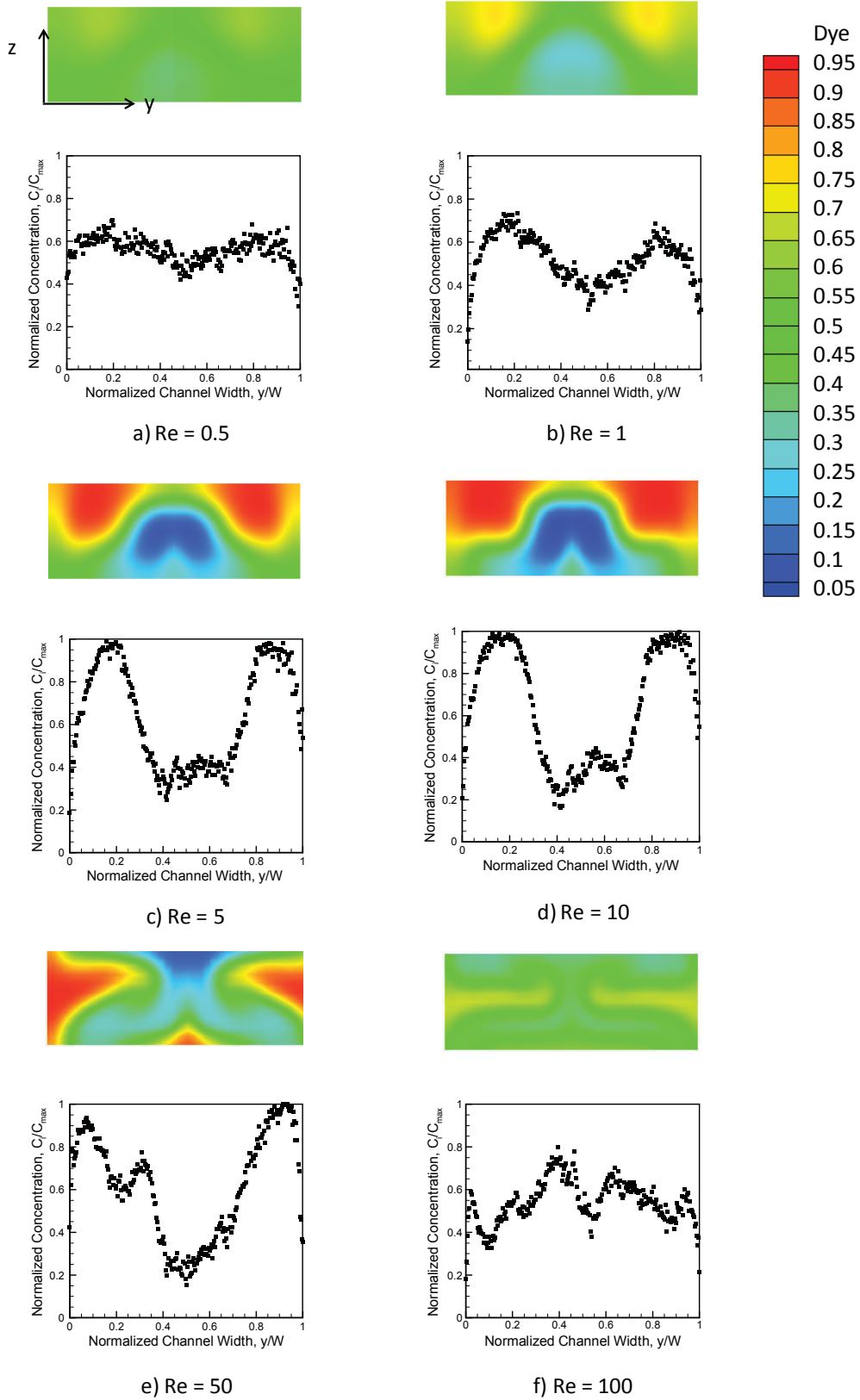
Figure 6.18: Concentration distribution at outlet S6 over 0.5 ≤ Re ≤ 100.

occurs at Re = 0.5, where the concentration distribution appears nearly uniform. Large

concentration gradients represent incomplete mixing, which is most notable over 5 ≤ Re

≤ 50. Figure 6.19 presents the numerically and experimentally obtained mixing indices

at the outlet over 0.5 ≤ Re ≤ 100. A decreasing-increasing trend in mixing is observed

with increasing Reynolds number, with an inflection point at Re = 10. The minimum in

the curve in figure 6.19 represents the change in dominant mixing mechanism from

mass diffusion to mass advection. At low Reynolds number, where residence time is
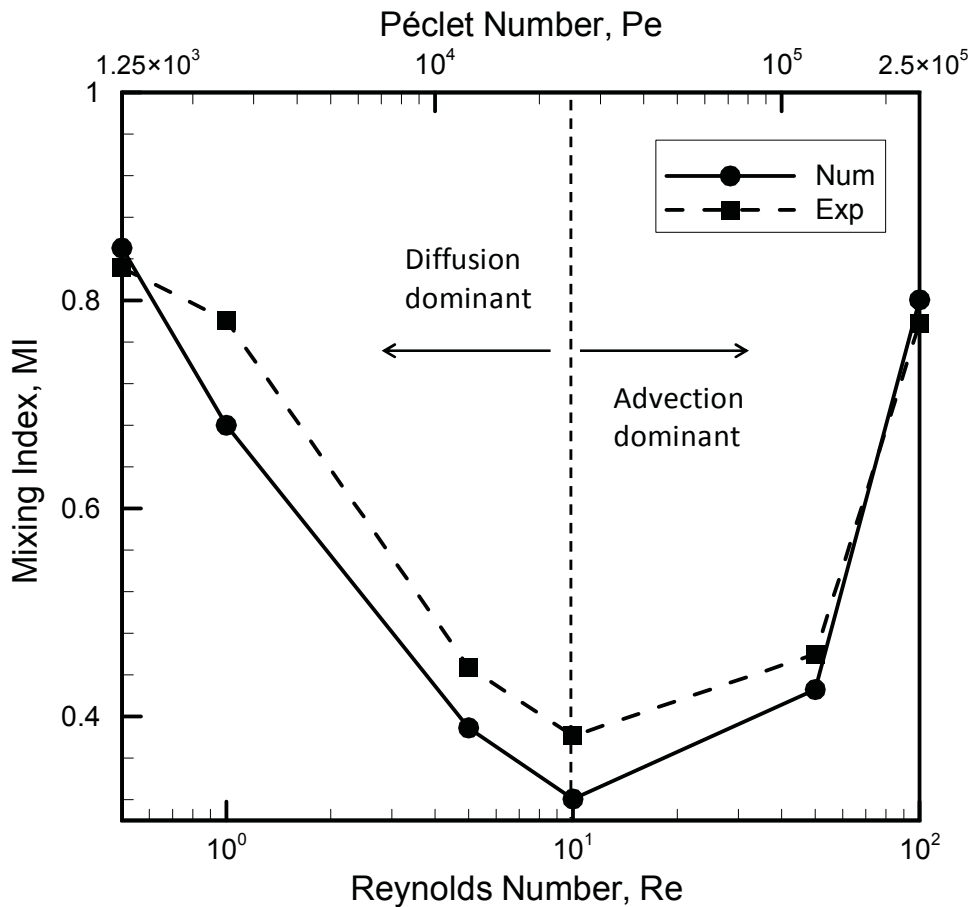
Figure 6.19: Numerically and experimentally obtained mixing indices at the outlet.

high, mass diffusion dominates. Values of MI_{exp}= 0.83, 0.78 and 0.44 are reported for Re = 0.5, 1 and 5, respectively. Helical flow resulting from the grooved sub-channels is responsible for increasing the species interfacial area and promoting mixing. At Re = 10 (MI_{exp} = 0.38), where the lowest degree of mixing is reported, residence time is insufficient to allow for thorough mixing. Additionally, insufficient momentum forces are unable to promote the formation of Dean vortices. At higher Reynolds numbers (Re = 50 and 100) advection dominates. The onset of Dean vortices promotes additional fluid overlap and rotation, increasing the species interfacial area and reducing the path of diffusion.   Induced fluorescence data provides MI_{exp}= 0.46 and 0.78 for Re = 50 and 100, respectively. The error between numerically and experimentally reported mixing indices at the outlet, as calculated by equation 5.1, is within 19 %.

6.5 Comparison of Device

To allow for more reasonable comparison with other experimental data published within the last few years, the total mixing length of the present device, taking into account the length of the curved sub channels, was used. The total mixing length, $L_{tot} \approx$ 137.5 mm, was used for comparison.

Chen et al. (2011a) used an alternate equation to determine the degree of mixing. Their mixing parameter, denoted here as *MP*, is defined according to the equation

$$MP = 1 - \frac{\int\limits_{A} \left| I - I_{avg} \right| dA}{\int\limits_{Ai} \left| I - I_{avg} \right| dA} \qquad (6.2)$$

where A is the area at a given location, A_i is the area at the inlet, at the onset of mixing, and I_{avg} is the average intensity. In the present device, the mixing index was calculated based on the length, dy, rather than area, dA, as the IF technique used in the present study presents the whole field concentration distribution 2 dimensionally. Figure 6.20 shows the comparison between the present device and the staggered Dean vortex
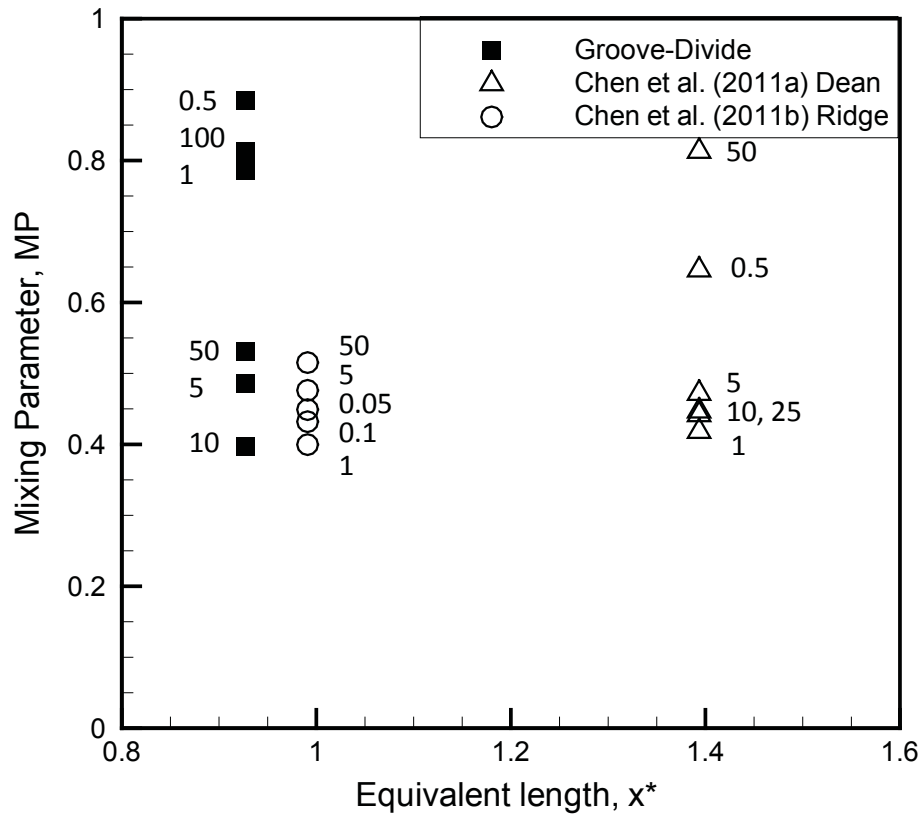
Figure 6.20: Comparison of the present device with the crosswise ridge and staggered Dean vortex micromixers (Chen et al. 2011 a,b). Numbers next to data points indicate Reynolds number.

micromixer (Chen et al. 2011a) and the crosswise ridge micromixer (Chen et al. 2011b). Data from published work was selected at locations as close to $x^* = 1$ as possible. In this chapter, the present micromixer was selected as a reference for x^* calculations. As shown, the present device offers comparable performance to the crosswise ridge design at Re = 5 and 50 in the vicinity of $x^* = 1$. At low Reynolds numbers (Re = 0.5, 1) superior mixing performance is noted in the current mixer compared to both designs, likely owing in part to the additional inlet lamella as well as the combined effects of the grooves and circular division elements.

6.6 Summary

A novel passive micromixer was designed, fabricated and tested over 0.5 ≤ Re ≤ 100. Slanted grooves and circular division elements were applied to promote flow rotation over a wide range of Reynolds numbers. Flow visualization provided qualitative information regarding flow patterns and mixing, while induced fluorescence provided quantitative mixing information and concentration distribution data. Numerical simulations were applied to describe complex three dimensional flow patterns. Good agreement was reported between experimental and numerical results. Flow rotation was observed at all investigated Re; at low Re, grooves produced helical flow as a result of anisotropic pressure gradients, while at Re ≥ 50, the formation of Dean vortices were observed. Four counter-rotating vortices were observed in the main channel at Re ≥ 50 as a result of the joining of two Dean vortices from each substream. The present device presents an alternate means to generate four counter-rotating vortices while

maintaining lower Dean numbers. A decreasing-increasing trend in mixing efficiency was observed as the dominant mixing mechanism changed from mass diffusion to mass advection, with a critical Reynolds number of Re = 10. The highest degree of mixing, MI_{exp} = 0.83, was reported at Re = 0.5, followed by MI_{exp} = 0.78 at Re = 100.

Chapter 7

Conclusions and Future Directions

7.1 Summary and Contributions

Three novel passive scaled-up micromixers were fabricated and experimentally and numerically evaluated in this study over 0.5 ≤ Re ≤ 100. All mixers were evaluated experimentally; flow visualization was employed to assess flow patterns and provide qualitative concentration distribution data along the channel lengths, while μ-induced fluorescence was applied at select locations along the channel lengths to quantify species distribution. To complement experimental findings and assess complex three dimensional flow, numerical simulations were applied to the mixers based on significant flow rotation.

The first design, the parallel lamination micromixer with tear drop obstructions, was evaluated experimentally over 1 ≤ Re ≤ 100. This device increased the interfacial species area and reduced the path of diffusion by employing a 7-lamellae uneven interdigital inlet. Tear drop obstructions acted as focusing structures and repeatedly reduced the path of diffusion along the channel length. Half-pins along the channel sidewalls along with a reduced lamellar width encouraged sidewall mixing. The formation of Dean vortices was noted in the vicinity of the tear drop obstructions at

higher Reynolds numbers, while the formation of additional lamellae was observed at Re ≥ 50. A decreasing-increasing trend in mixing efficiency was reported, with an inflection point at Re = 25, representing the change in dominant mixing mechanism from mass diffusion to mass advection. Diffusion remains an important mechanism at all Reynolds numbers; the increase in the number of lamellae allowed for increased surface area to be available for mass transfer. A maximum outlet mixing index of 0.68 was obtained at Re = 1.

A Y-inlet serpentine mixer embedded with slanted grooves on the bottom surface was evaluated experimentally and numerically over 0.5 ≤ Re ≤ 100. Grooves caused helical fluid motion, guiding species from one sidewall to the other. The formation of Dean vortices was observed at Re ≥ 50 as a result of the curved channel. An increase in the degree of fluid overlap was observed with increasing Reynolds number. A decreasing-increasing trend in the degree of mixing was observed with increasing Reynolds number with an inflection point at Re = 5, marking the transition from diffusion dominance to advection dominance. The highest mixing index, 0.90, was obtained numerically at Re = 100.

Based on the benefits observed through investigation of the two aforementioned micromixers, the micromixer with groove-enhanced division elements was designed and evaluated experimentally and numerically. A simple three-lamella inlet was used to increase the area available for mass transfer while maintaining a more simple fabrication process. Species were supplied parallel to each other, rather than

head on (T-inlet) or at an angle (Y-inlet), as this was found to reduce the occurrence of oscillations resulting from the use of two separate syringe pumps. Curved portions were included to promote the formation of Dean vortices at higher Reynolds numbers, while grooves allowed for helical flow to develop. Recombining rotating species through use of the dividing elements allowed for the formation of additional striations, increasing the interfacial area available for mass transfer. Four counter-rotating vortices were observed at Re ≥ 50 (K ≥ 15.1) as a result of the joining of two of Dean vortices in two substreams. Again, a decreasing-increasing trend in the degree of mixing was observed, with a critical point at Re = 10, marking the shift from diffusion dominance to advection dominance. The highest degree of mixing, MI_{exp} = 0.83, was observed at Re = 0.5.

To reasonably compare the mixing performance of micromixers of various scales, a comparison technique was introduced. The equivalent length, x^*, scales devices to the same hydraulic diameter, and allows for mixing efficiency comparison at comparable lengths. The devices presented typically offered good mixing at similar equivalent lengths and Reynolds numbers compared to devices presented in the literature.

Figure 7.1 presents the experimentally obtained mixing indices at the outlet for the all three proposed micromixers. The length to hydraulic diameters of the parallel lamination micromixer with tear drop obstructions, groove-enhanced serpentine micromixer, and micromixer with groove-enhanced division elements are approximately 38.5, 129.8 and 126, respectively. The latter two designs, with similar equivalent
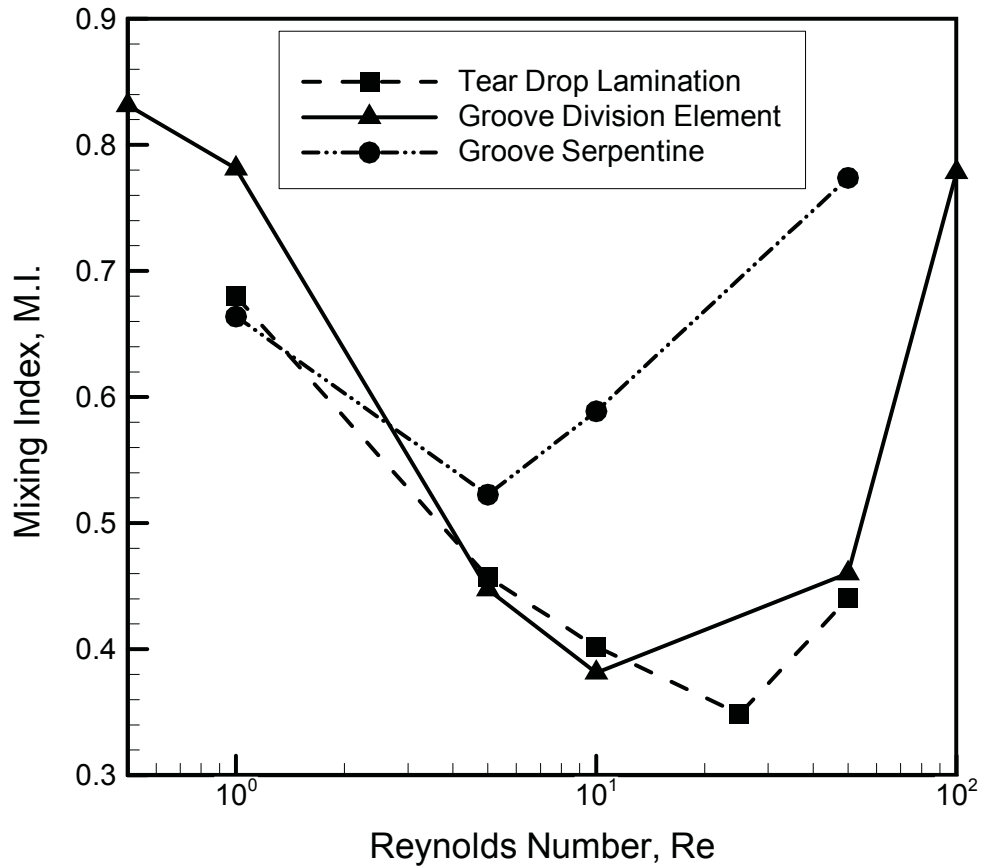
Figure 7.1: Outlet mixing indices for three proposed micromixers.

lengths, may be reasonably directly compared at the outlet. As shown, the groove-enhanced serpentine mixer shows better mixing than the groove-enhanced division element mixer at Re ≥ 5, as a result of stronger rotation allowing for increased interfacial surface area. At lower flow rates, the groove enhanced division element mixer outperforms the serpentine mixer owing to the multi-lamella inlet, which allows for increased mass diffusion. At Re = 1, the parallel lamination mixer with tear drop obstructions produces the same mixing index as the groove-enhanced serpentine mixer. At Re = 5 and 50, the parallel lamination micromixer shows a mixing performance

comparable to that of the groove-enhanced division element mixer. As the length to hydraulic diameter of the parallel lamination mixer is several times smaller than the other two devices, it may be deduced that the parallel lamination mixer offers superior performance at the aforementioned Reynolds numbers. This is attributed primarily to the seven-lamella inlet. Increased residence time and fluid rotation render the groove-enhanced division element micromixer suitable for operation at low (Re = 0.5) and high (Re = 100) Reynolds numbers.

7.2 Challenges

A variety of challenges exist with regards to experimental evaluation. Leakage is the primary challenge, and techniques must be employed to prevent leakage at the inlets and outlet, as well as along the channel lengths. When filling the channel, it is difficult to avoid the presence of trapped air bubbles. Although their effect is minimal given the relative size of the bubbles compared to the channel, they are undesirable. Manually filling and rotating the test section (parallel lamination tear drop mixer) to avoid air bubbles is time consuming and challenging, and small air bubbles in the grooves of the serpentine channel were unavoidable. The filling and emptying process must be repeated from calibration to experiment. Additionally, to allow for use a calibration tank, the test section must be perfectly flat and machined in a similar manner at all investigated locations. Tool marks, scratches and stains resulting from bonding agents led to reflections during IF experiments.

7.3 Future Directions

A continuation of the present work could include some of the following improvements and areas of investigation:

- To improve the performance of the proposed micromixers, numerical optimization should be performed. Investigating parameters including channel height and width, as well as groove depth, width and angle, and groove spacing would lead to improved mixing performance.

- Grooves located on both sides of the channel would lead to improved mixing. In this work, grooves were applied to a single side due to the potential for increased experimental complications, namely, the formation of large air bubbles. The presence of air bubbles in microscale mixers is also of concern. Degassing the working fluid prior to filling the channels may help to avoid trapped air bubbles, and allow for further investigation.

- As the induced fluorescence technique applied is whole volume in nature, the concentration distribution along the cross section may not be determined experimentally. Confocal scanning induced fluorescence would allow for the species distribution along the cross section to be determined and more accurately compared to numerical work.

- For scaled up devices, a modification to the sealing slot should be made: the sealing slot and tab should form a channel wall, avoiding space between the channel and sealing slot.

- Water was used in the present investigation. To more closely replicate industrial applications, solutions with different physical properties may be investigated, including solutions which generate chemical reactions.   In these applications, reaction time is of concern, and temperature variations may be produced. For bio-medical applications involving blood components, for example, the shear generated must be considered to avoid damaging biological samples.

Publications

Journal

Cook, K. J., Fan, Y. F., Hassan, I. G., "Experimental Investigation of a scaled-up passive micromixer with uneven interdigital inlet and tear-drop obstruction elements" (In Press, available online – DOI 10.1007/s00348-011-1246-4) *Experiments in Fluids, 2011*

Cook, K. J., Hassan, I. G., "Experimental and Numerical Evaluation of a Scaled-up Micromixer with Groove Enhanced Division Elements", submitted to *Experiments in Fluids*

Cook, K. J., Fan, Y. F., Hassan, I. G., "Mixing Evaluation of a Passive Scaled-up Serpentine Micromixer with Slanted Grooves", submitted to *ASME Journal of Fluids Engineering*

Conference

Cook, K. J., Fan, Y. F., Hassan, I. G., "Experimental Investigation of a scaled-up passive interdigital micromixer with tear drop obstruction elements", *Proceedings of the 2nd European Conference on Microfluidics - Microfluidics 2010*, Toulouse, France, December 8-10, 2010

Cook, K. J., Fan, Y. F., Hassan, I. G., "Experimental Investigation of a scaled up passive interdigital micromixer with circular-sector mixing elements", *Proceedings of the ASME/JSME 8th Thermal Engineering Joint Conference (AJTEC-11)*, Honolulu, USA, March 13-17, 2011

Cook, K. J., Hassan, I. G., "Experimental Investigation of a Scaled-up Passive Curved Channel Micromixer with Slanted Grooves", *Proceedings of* the *ASME 2011 9th International Conference on Nanochannels, Microchannels, and Minichannels*, Edmonton, Canada, June 19-22, 2011

Cook, K. J., Hassan, I. G., "Experimental and Numerical Investigation of a Scaled-up Passive Micromixer with Groove-Enhanced Division Elements and Interdigital Inlet", Proceedings of the ASME 2012 10th *International Conference on Nanochannels, Microchannels, and Minichannels*, Rio Grande, Puerto Rico, July 8-12, 2012.

References

Adeosun, J. T., Lawal, A., 2009, "Numerical and experimental mixing studies in a MEMs-based multilaminated/elongated flow micromixer", *Sensors and Actuators*, **B 139**, 637-647

Affanni, A., Chiorboli, G., 2010, "Development of an enhanced MHD micromixer based on axial flow modulation", *Sensors and Actuators*, **B 147**, 748-754

Ahmed, D., Mao, X., Juluri, B. K., Huang, T. J., 2009a, "A fast microfluidic mixer based on acoustically driven sidewall-trapped microbubbles", *Microfluid Nanofluid*, **7**, 727-731

Ahmed, D., Mao, X., Shi, J., Juluri, B. K., Huang, T. J., 2009b, "A millisecond micromixer via single-bubble-based acoustic streaming", *Lab on a Chip*, **9**, 2739-2741

Ansari, M.A., Kim, K.Y., Anwar, K., Kim, S.M., 2010, "A novel passive micromixer based on unbalanced splits and collisions of fluid streams", *Journal of Micromechanics and Microengineering*, **20**, 10pp

Ansari, M. A., Kim, K.-Y., 2010, "Mixing performance of unbalanced split and recombine micromixers with circular and rhombic sub-channels", *Chemical Engineering Journal*, **162**, 760-767

Aubin, J., Ferrando, M., Jiricny, V., 2010, "Current methods for characterising mixing and flow in microchannels", *Chemical Engineering Science*, **65**, 2065-2093

Bessoth, F. G., deMello, A. J., Manz, A., 1999, "*Microstructures for Efficient Continuous Flow Mixing*", *Anal. Commun.,* **36**, 213-215

Bhagat, A. A. S., Papautsky, I., 2008, "Enhancing particle dispersion in a passive planar micromixer using rectangular obstacles", *Journal of Micromechanics and Microengineering*, **18**, 9 pages

Bhagat, A. A. S., Peterson, E. T. K., Papautsky, I., 2007, "A passive planar micromixer with obstructions for mixing at low Reynolds numbers", *Journal of Micromechanics and Microengineering*, **17**, 1017-1024

Chang, C. K., Shih, T. R., Chung, C. K., 2011, "Design and fabrication of an advanced rhombic micromixer with branch channels", *Proceedings of the 2011 6th IEEE International Conference on Nano/Micro Engineered and Molecular Systems*, February 20-23, 2011, Kaohsiung, Taiwan

Cerbelli, S., Giona, M., 2008, "On the estimate of mixing length in interdigital micromixers", *Chemical Engineering Journal*, **138**, 523-537

Chen, J. J., Chen, C. H., Shie, S., R., 2011a, "Optimal Designs of Staggered Dean Vortex Micromixers*", International Journal of Molecular Science*s, **12**, 3500-3524

Chen, J. J., Lai, Y. R., Tsai, R., T., Lin, J., D., Wu, C., Y., 2011b, "Crosswise ridge micromixers with split and recombination helical flows", *Chemical Engineering Science*, **66** (10), 2164-2176

Chen, L., Wang, G., Lim, C., Seong, G.H., Choo, J., Lee, E. K., Kang, S. H., Song, J. M., 2009, "Evaluation of passive mixing behaviours in pillar obstruction poly(dimethylsiloxane) microfluidic mixer using fluorescence microscopy", *Microfluid Nanofluid*, **7**, 267-273

Choudhary, R., Bhakat, T., Singh, R. K., Ghubade, A., Mandal, S., Chosh, A., Rammohan, A., Sharma, A., Bhattacharya, S., 2010, "Bilayer staggered herringbone micro-mixers with symmetric and asymmetric geometries", *Microfluid Nanofluid*, **10**, 271-286

Chung, C. K., Shih, T. R., 2007, "A rhombic micromixer with asymmetrical flow for enhancing mixing", *Journal of Micromechanics and Microengineering*, **17**, 2495-2504

Chung, C. K., Shih, T. R., 2008, "Effect of geometry on fluid mixing of the rhombic micromixers", *Microfluid Nanofluid*, **4**, 419-425

den Toonder, J., Bos, F., Broer, D., Filippini, L., Gillies, M., de Goede, J., Mol, T., Reijme, M., Talen, W., Wilderbeek, H., Khatavkar, V., Anderson, P., 2008, "Artificial cilia for active micro-fluidic mixing", *Lab on a Chip*, **8** (4), 533-541

Du, Y., Zhang, Z., Yim, C.H., Lin, M., Cao, X., 2010, "A simplified design of the staggered herringbone micromixer for practical applications", *Biomicrofluidics*, **4**, 204105, 13 pages

Elmabruk, A. M., Ye, M., Wang, Y., Dai, Y., 2008, "A State-of-the-Art Review of Mixing in Microfluidic Mixers", *Chinese Journal of Chemical Engineering*, **16** (4), 503-516

Fan, Y. F., 2009. *Experimental and Numerical Investigations of Novel Passive Micromixers using μ-IF*. Thesis (MASc). Concordia University

Fan, Y. F., Hassan, I., 2010, "Experimental and Numerical Investigation of a Scaled-up Passive micromixer using Fluorescence Technique", *Experiments in Fluids*, **49**, 733-747

Gendron, P.-O., Avaltroni, F., Wilkinson, K. J., 2008, "Diffusion Coefficients of Several Rhodamine Derivatives as Determined by Pulsed Field Gradient-Nuclear Magnetic resonance and Fluorescence Correlation Spectroscopy", *Journal of Fluorescence*, **18**, 1093-1101

Hardt, S., Schönfeld, F., 2003, "laminar mixing in Different Interdigital Micromixers: II. Numerical Simulations", *AIChE Journal*, **49** (3), 578-584

Hessel, V., Löwe, H., Schönfeld, F., 2005, "Micromixers- a review on passive and active mixing principles", *Chemical Engineering Science*, **60**, 2479-2501

Hessel, V., Hardt, S., Löwe, H., Schönfeld, F., 2003, "Laminar Mixing in Different Interdigital Micromixers: I Experimental Characterization", *AIChE Journal*, **49** (3), 566-577

Hong, C.-C., Choi, J.-W., Ahn, C. H., 2004, "A novel in-plane passive microfluidic mixer with modified Tesla structures", *Lab on a Chip*, **4**, 109-113

Howell, P. B. Jr., Mott, D. R., Golden, J. P., Ligler, F. S., 2004, "Design and evaluation of a Dean vortex based micromixer", *Lab on a Chip*, **4**, 663-669

Hsieh, C.-Y., Yang, A.-S., 2009, "Mixing Enhancement of a Passive Micromixer by Applying Boundary Protrusion Structures", *Advanced Materials Research*, **74**, 77-80

Hsiung, S.-K., Lee, C.-H., Lin, J.-L., Lee, G.-B., 2007, "Active micro-mixers utilizing moving wall structures activated pneumatically by buried side chambers", *Journal of Micromechanics and Microengineering*, **17**, 129-138

Hu, Y. H., Chang, M., Lin, K. H., 2006, "A Study of Two Fluids Mixing in a Helical-Type Micromixer", *Journal of Physics: Conference Series*, **48**, 531-536

Jeong, G. S., Chung, S., Kim, C.-B., Lee, S.-H., 2010, "Applications of micromixing technology", *Analyst*, **135**, 460-473

Jiang, F., Drese, K.S., Hardt, S., Kupper, M., Schönfeld, F., 2004, "Helical Flows and Chaotic Mixing in Curved Micro Channels", *AIChE Journal*, **50** (9), 2297-2305

Khatavkar, V. V., Anderson, P. D., den Toonder, J. M. J., Meijer, H. E. H., 2007, "Active micromixer based on artificial cilia", *Physics of Fluids*, **19**, 083605 (13 pages)

Li, L., Lee, J., Castro, J. M., Yi, A. Y., 2010a "Improving mixing efficiency of a polymer micromixer by use of a plastic shim divider", *J. Micromechanics and. Microengineering*, **20** (3), 9pp

Li, L., Yang, C., Shi, H., Liao, W.-C., Huang, H., Lee, L. J., Castro, J. M., Yi, A. Y., 2010b, "Design and Fabrication of an Affordable Polymer Micromixer for Medical and Biomedical Applications", *Polymer Engineering and Science*, **50** (8), 1594-1604

Lim, T. W., Son, Y., Jeong, Y. J., Yang, D.-Y., Kong, H.-J., Lee, K.-S., Kim, D.-P., 2011, "Three-dimensionally crossing manifold micro-mixer for fast mixing in a short channel length", *Lab on a Chip*, **11**, 100-103

Lin, C.-M., Liu, H.-P., Lai, Y.-S., Tseng, C.-C., Chen, C.-Y., Wo, A. M., 2011, "Micromixing via recirculatory flow generated by an oscillatory microplate", *Microfluid Nanofluid*, **11**, 167-176

Lin, Y. C, Chung, Y.C., Wu, C.Y., 2007, "Mixing enhancement of the passive microfluidic mixer with J-shaped baffles in the tee channel", *Biomed Microdevices*, **9**, 215-221

Löb, P., Drese, K. S., Hessel, V., Hardt, S., Hofmann, C., Löwe, H., Schenk, R., Schönfeld, F., Werner, B., 2004, "Steering of Liquid Mixing Speed in Interdigital Micro Mixers- from Very Fast to Deliberately Slow Mixing", *Chem. Eng. Technol.*, **27** (3), 340-345

Lu, Z., McMahon, J., Mohamed, H., Barnard, D., Shaikh, T. R., Manella, C. A., Wagenknecht, T., Lu, T.M., 2010, "Passive microfluidic device for submillisecond mixing", *Sensors and Actuators*, **B 144**, 301-309

Luong, T.-D., Phan, V.-N., Nguyen, N.-T., 2011, "High-throughput micromixers based on acoustic streaming induced by surface", *Microfluid Nanofluid*, **10**, 619-625

Lynn, N. S., Dandy, D. S., 2007, "Geometric optimization of helical flow in grooved micromixers", *Lab on a Chi*p, **7** (5), 580-587

Mouza, A. A., Patsa, C. M., Schönfeld F., 2008, "Mixing performance of a chaotic micro-mixer", *Chemical Engineering Research and Design*, **86**, 1128-1134

Nguyen, N.-T. 2007. Mixing in Microscale. In S. Hardt and F. Schönfeld (Eds.), *Microfluidic Technologies for Miniaturized Analysis Systems* (117-155) Springer.

Nguyen, N.-T., Wu, Z., 2005, "Micromixers- a review", Journal of Micromechanics and Microengineering, **15**, R1-R16

Nguyen, T. N. T, Kim, M.-C., Park, J.-S., Lee, N.-E., 2008, "An effective passive microfluidic mixer utilizing chaotic advection", *Sensors and Actuators*, **B 132**, 172-181

Schönfeld, F., Hardt, S., 2004, "Simulation of Helical Flows in Microchannels", *AIChE Journal*, **50** (4), 771-778

Stroock A. D., Dertinger, S.K.W., Ajdari, A., Mezić, I., Stone, H. A, Whitesides, G. M., 2002, "Chaotic Mixer for Microchannels", Science, **295**, 647-651

Sudarsan A. P., Ugaz, V. M., 2006, "Fluids mixing in planar spiral microchannels", *Lab on a Chip*, **6**, 74-82

Tan, H. Y. Loke, W. K., Tan, Y. T., Nguyen, N.-T., 2008, "A lab-on-a-chip for detection of nerve agent sarin in blood", *Lab on a Chip*, **8**, 885-891

Tofteberg, T., Skolimowski, M., Andreassen, E, Deschke, O., 2010, A novel passive micromixer: lamination in a planar channel system. *Microfluid Nanofluid*, **8**, 209-215

Tsai, R.-T., Wu, C.-Y., 2011, "An efficient micromixer based on multidirectional vortices due to baffles and channel curvature", *Biomicrofluidics*, **5**, 014103 (13 pages)

Tseng, L.-Y., Yang, A.-S., Lee, C.-Y., Hsieh, C.-Y., 2011, "CFD-based optimization of a diamond-obstacles inserted micromixer with boundary protrusions", *Engineering Applications of Computational Fluid Mechanics*, **5** (2), 210-222

Vilfan, M., Potočnik, A., Kavčič, B., Osterman, N., Poberaj, I., Vilfan, A., Babič, D., 2010, "Self-assembled artificial cilia", *Proceedings of the National Academy of Sciences*, **107** (5), 1844-1847

Wen, C.-Y., Yeh, C.-P., Tsai, C.-H., Fu, L.-M., 2009, "Rapid magnetic microfluidic mixer utilizing AC electromagnetic field", *Electrophoresis*, **30**, 4179-4186

Wu, Z., Nguyen, N.-T., 2005, "Convective-Diffusive transport in parallel lamination micromixers", *Microfluid Nanofluid*, **1**, 208-217

Xia, H. M., 2009. *Fluid Mixing Enhancement through Chaotic Advection in Mini/Micro-Channel.* Thesis, (PhD). National University of Singapore

Xie, H., Fan, Y., Yang, H., 2011, "New 3D SAR micromixer based on 2D standard photolithographic technique", *Micro & Nano Letters*, **6** (6), 366-371

Yang, J.-T., Huang, K.-J., Lin, Y.-C., 2005, "Geometric effects on fluid mixing in passive grooved micromixers*", Lab on a Chip*, **5**, 1140-1147

Yang, J.-T., Fang, W.-F., Tung, K.-Y., 2008, "Fluids mixing in devices with connected-groove channels", *Chemical Engineering Science*, **63**, 1871-1881

Yeo, L. Y., Friend, J. R., 2009, "Ultrafast microfluidics using surface acoustic waves", *Biomicrofluidics*, **3** (1), 012002, 23 pages

Web references

Abramowitz, M., Davidson, M. W., "Fluorochrome Data Tables." M*icroscopy Resource Center*. Retrieved January 9, 2012, from

http://www.olympusmicro.com/primer/techniques/fluorescence/fluorotable2.html

Johnson, I. D., Davidson, M. W., "Jablonski Energy Diagram." M*icroscopy Resource Center*. Retrieved November 7, 2011, from

http://www.olympusmicro.com/primer/java/jablonski/jabintro/index.html

Appendix A. IF Data: Parallel Lamination

Micromixer with Tear Drop Obstructions

a) L1

b) L2

c) L3

d) L4
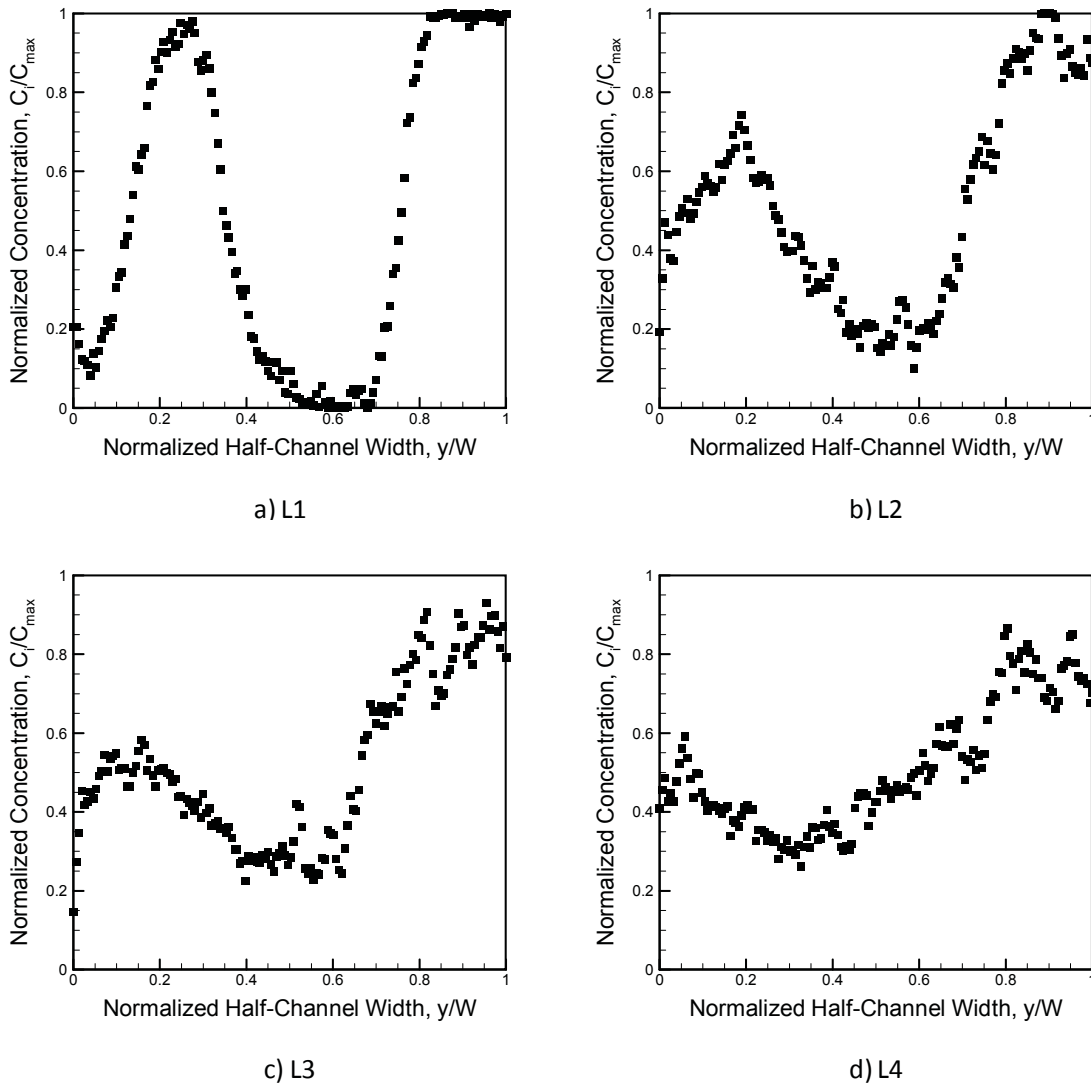
Figure A.1: Re = 1.

a) L1
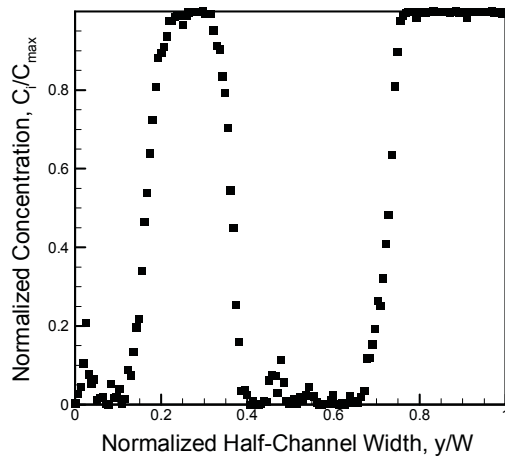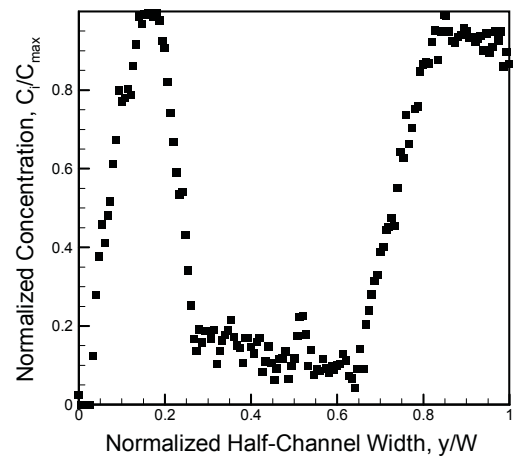
b) L2
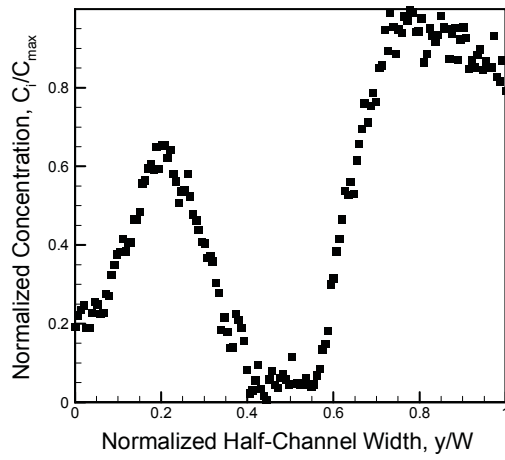
c) L3
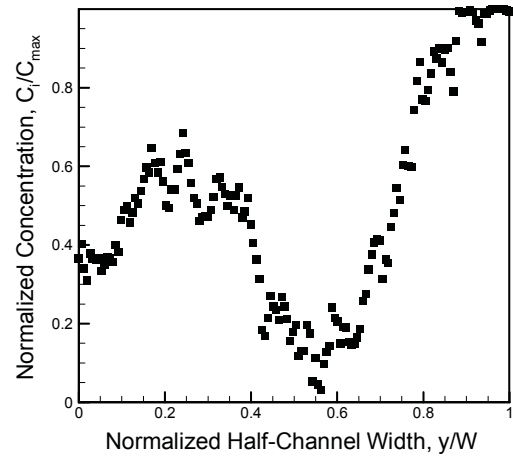
d) L4

Figure A.2: Re = 5.

a) L1
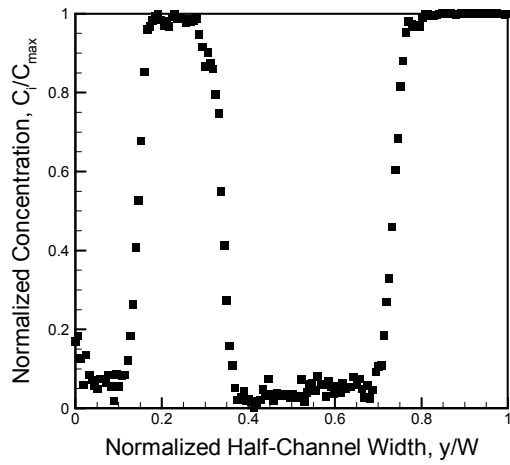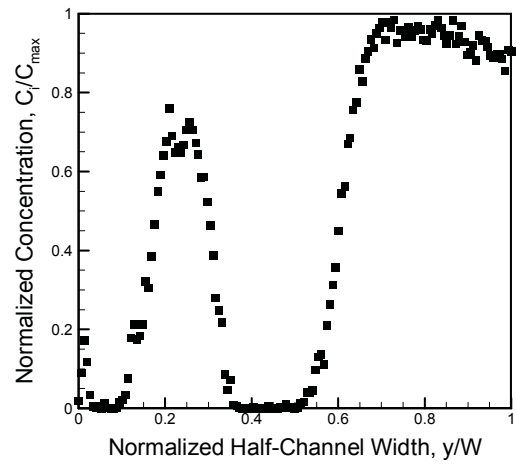
b) L2
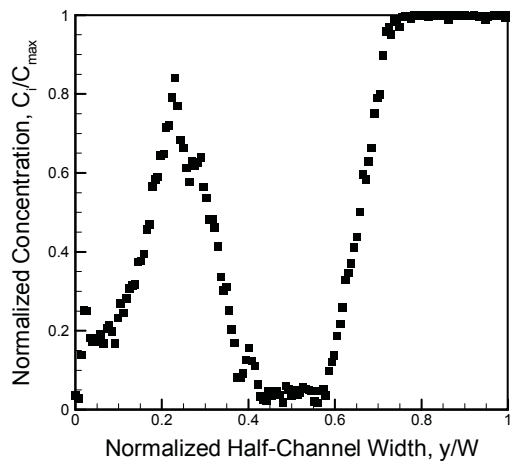
c) L3
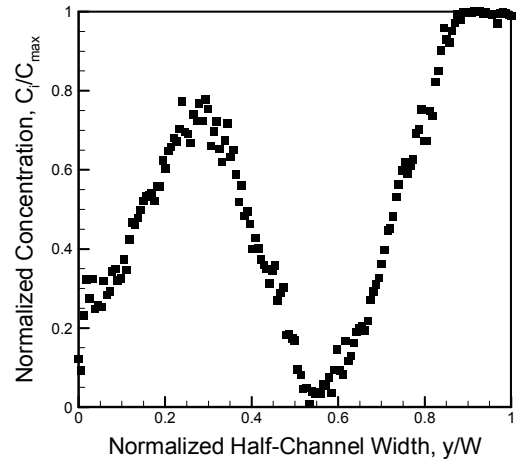
d) L4

Figure A.3: Re = 10.

a) L1
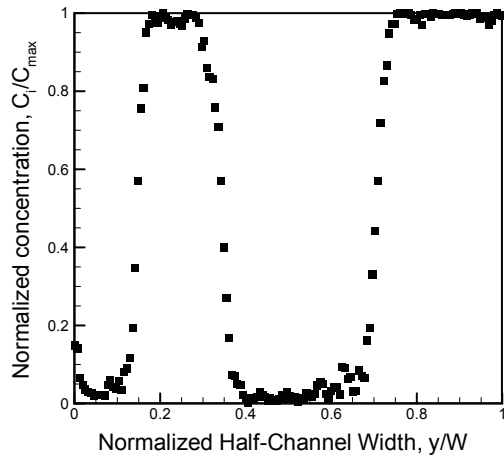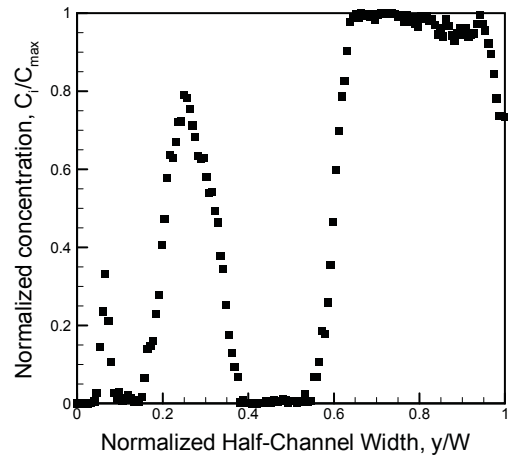
b) L2
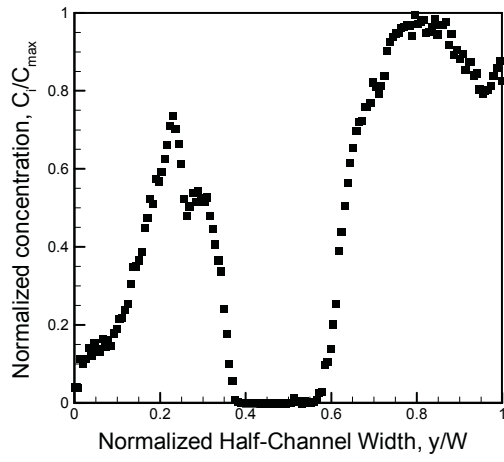
c) L3
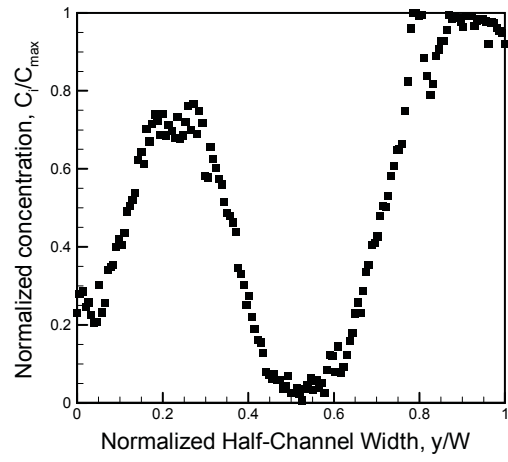
d) L4

Figure A.4: Re = 25.

a) L1
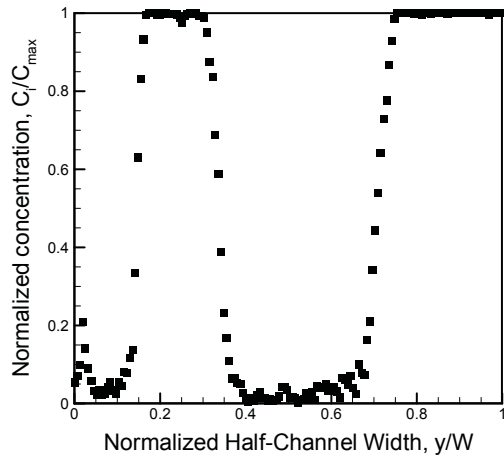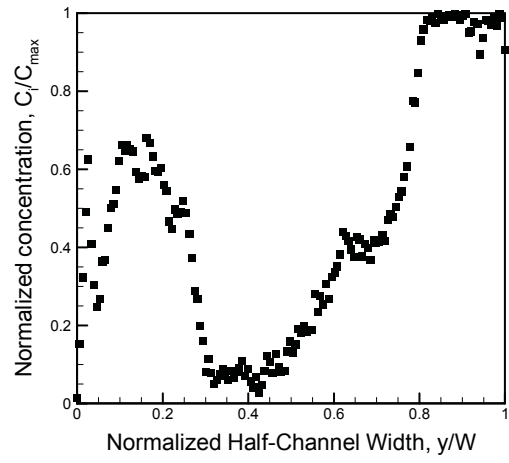
b) L2
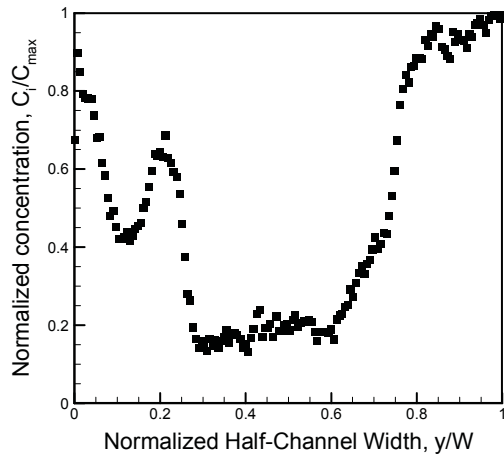
c) L3
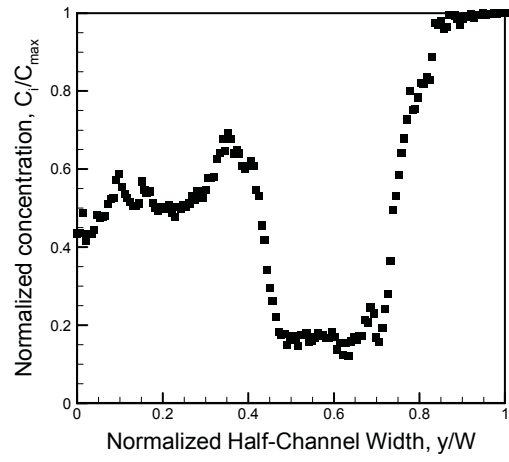
d) L4

Figure A.5: Re = 50.

Appendix B. IF Data: Groove-Enhanced Serpentine

Micromixer

a) L1

b) L2

c) L3

d) L4

e) L5
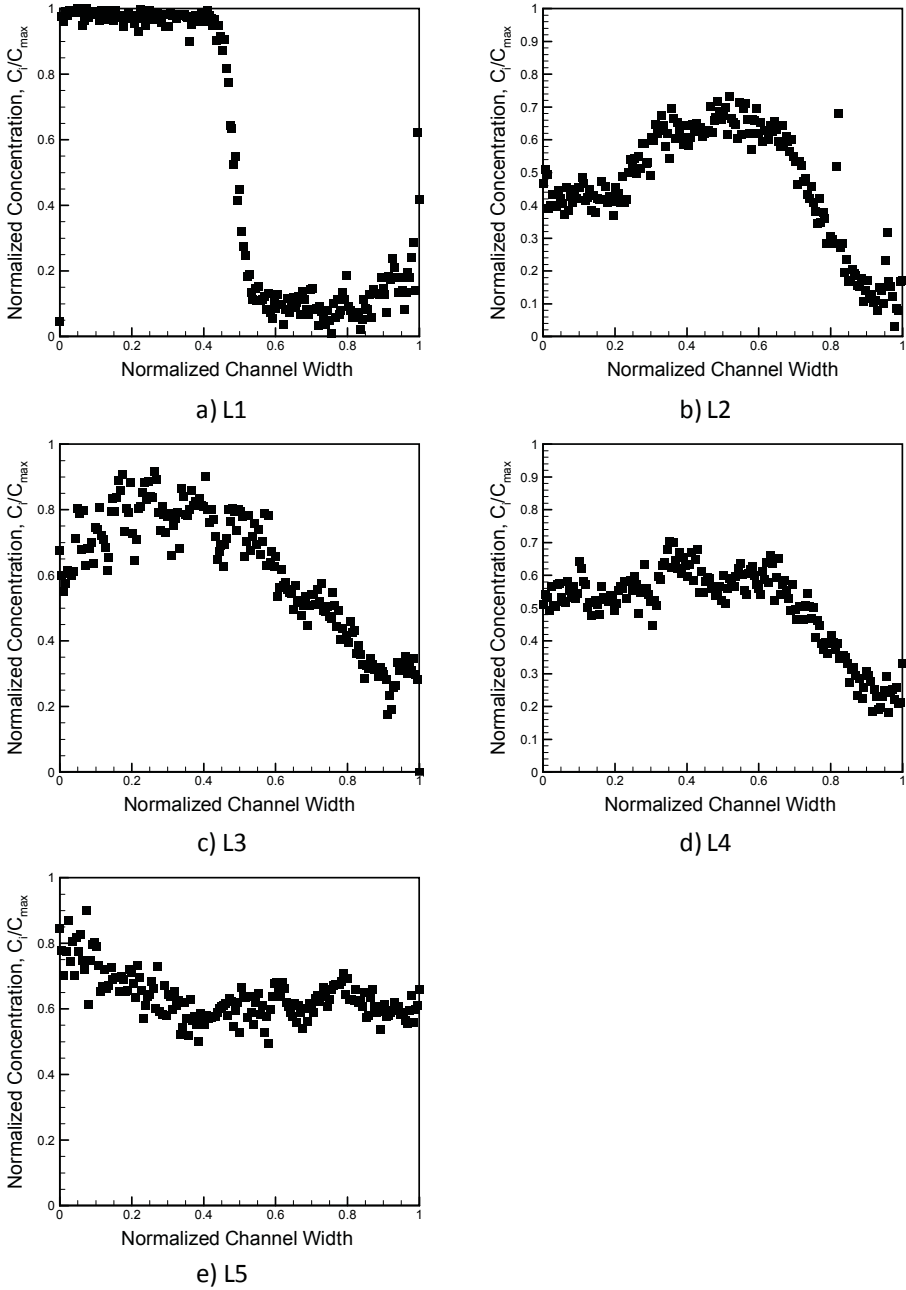
Figure B.1: Re = 1.

a) L1

b) L2
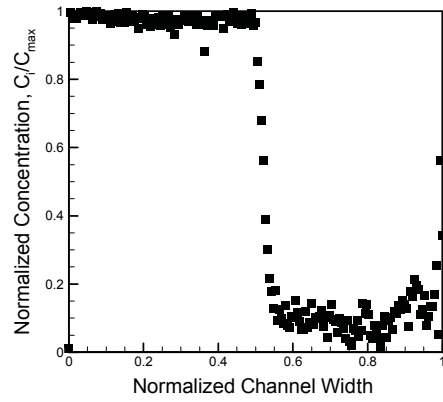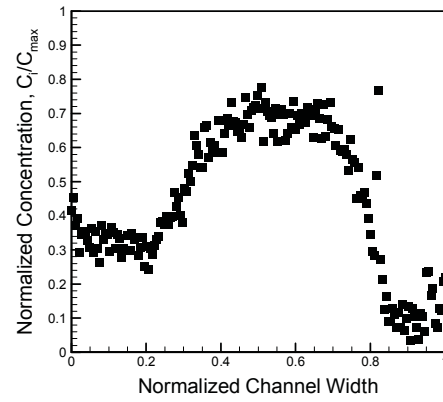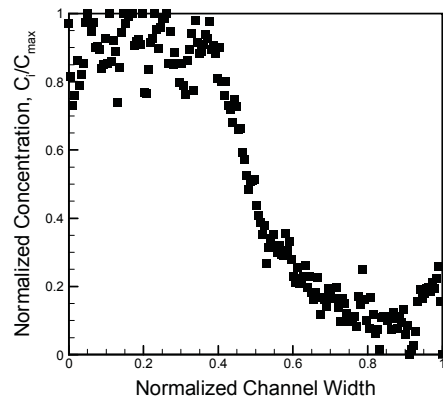
c L3
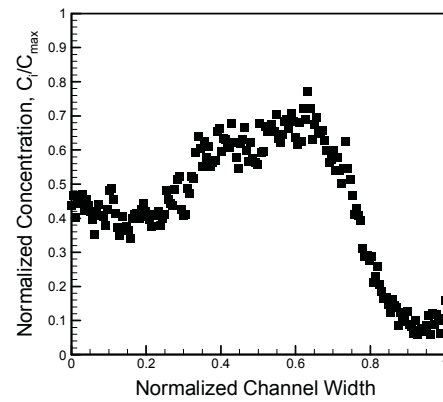
d) L4
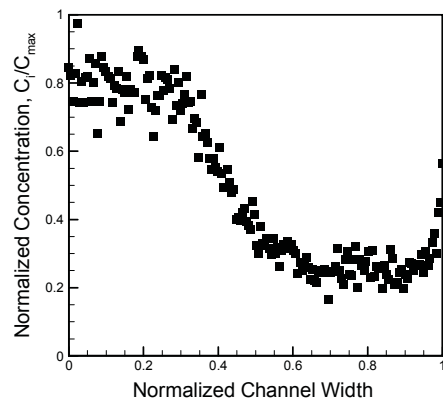
e) L5

Figure B.2: Re = 5.

a) L1

b) L2
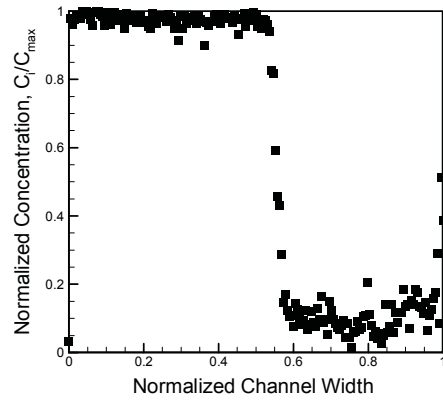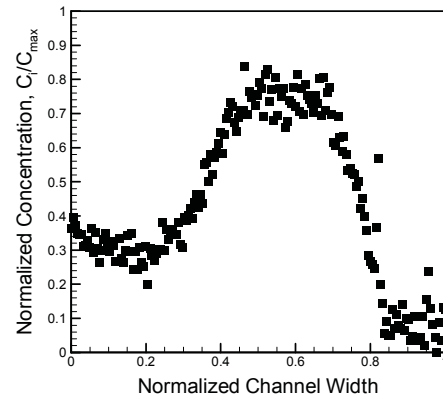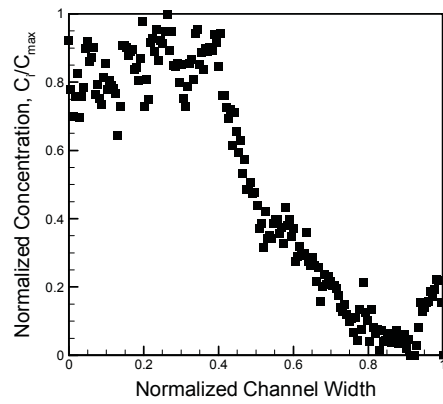
c) L3
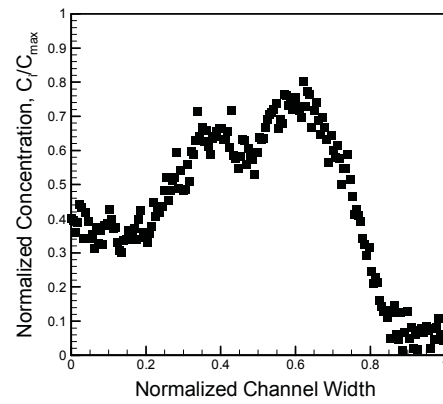
d) L4
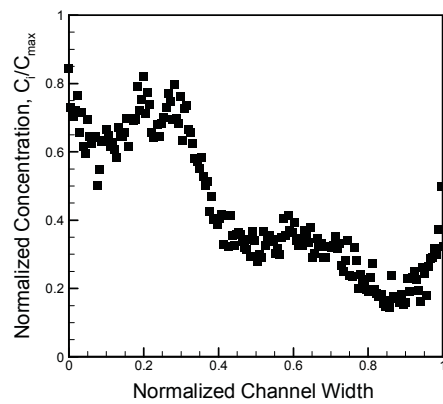
e) L5

Figure B.3: Re = 10.

a) L1

b) L2
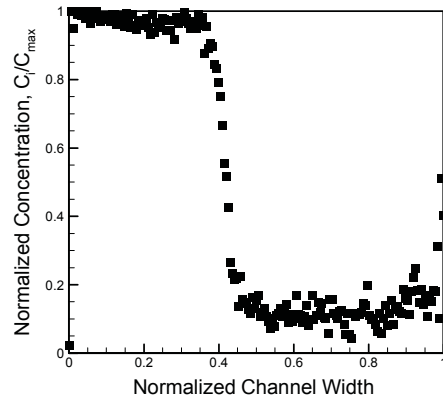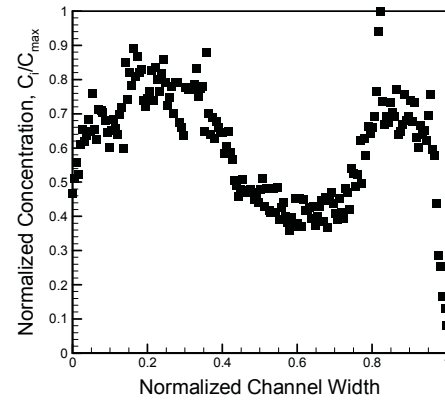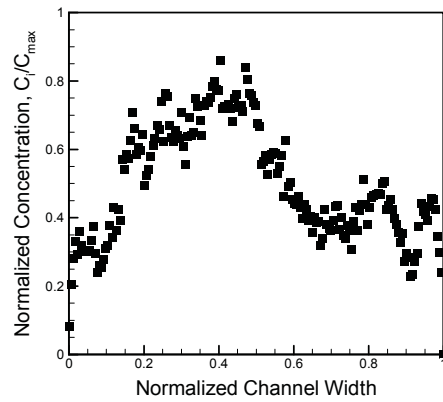
c) L3
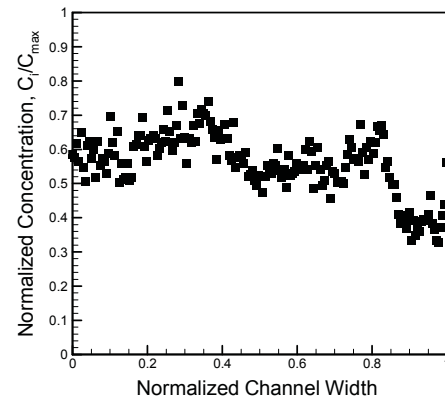
d) L4
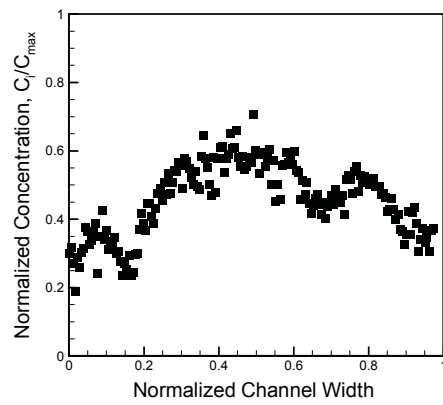
e) L5

Figure B.4: Re = 50.

Appendix C. IF Data: Micromixer with Groove-Enhanced Division Elements

a) S1

b) S2

c) S3

d) S4

e) S5

f) S6
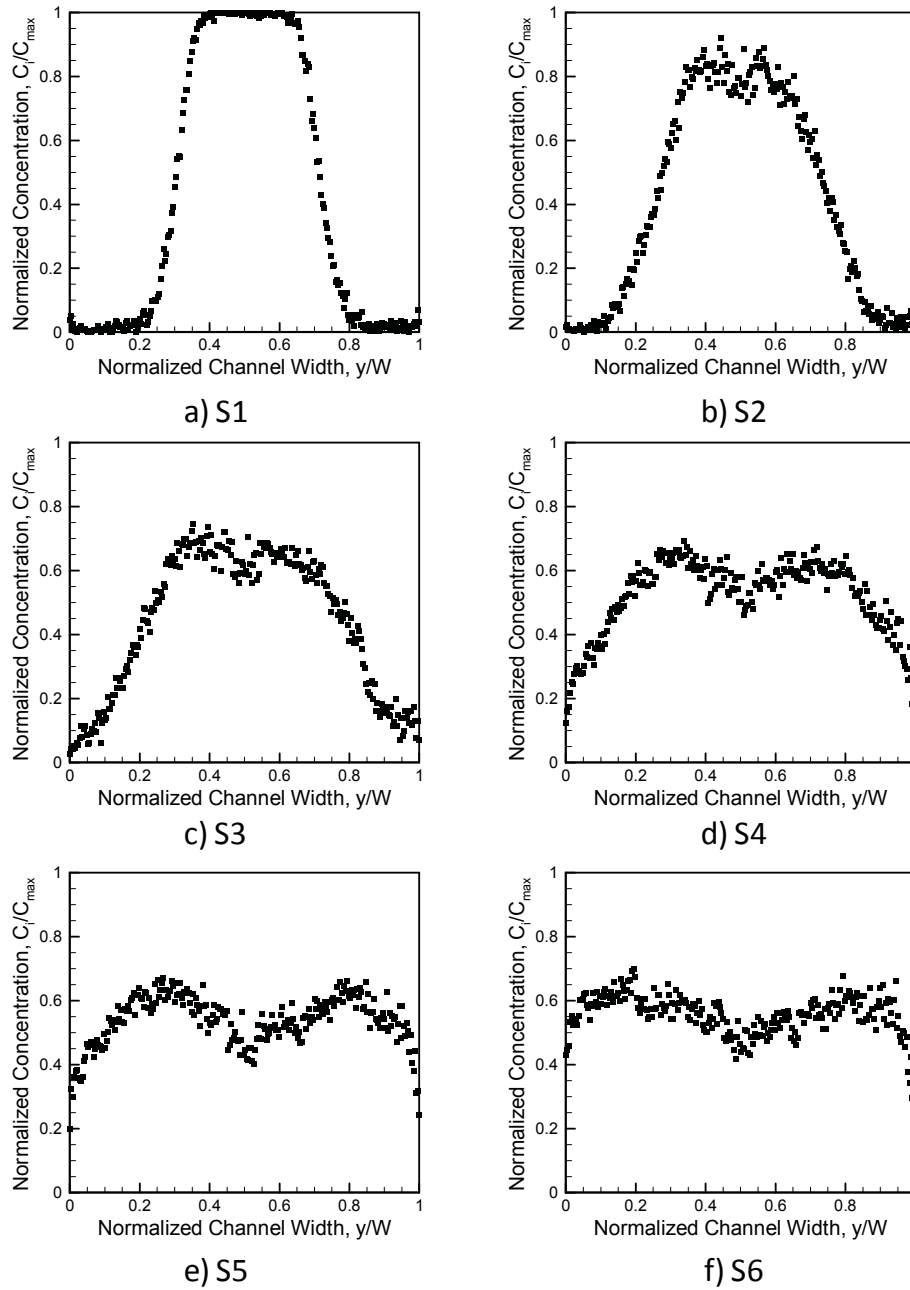
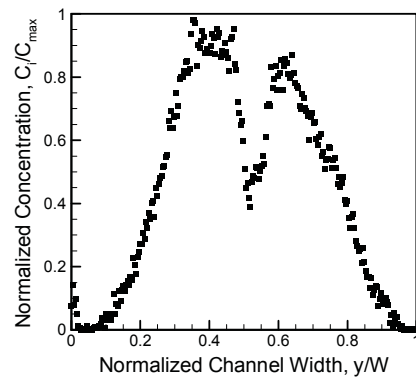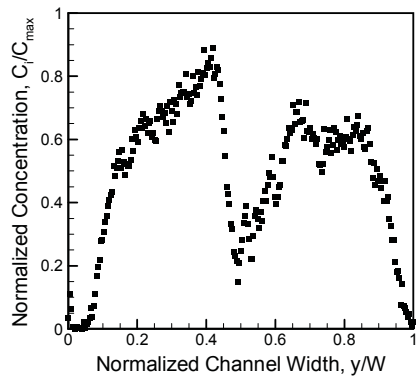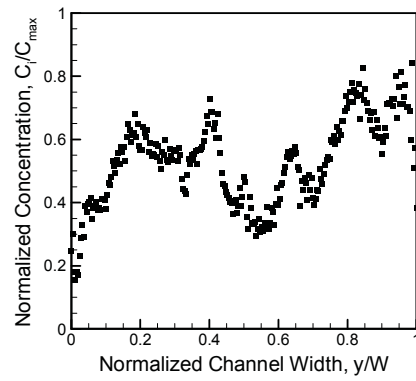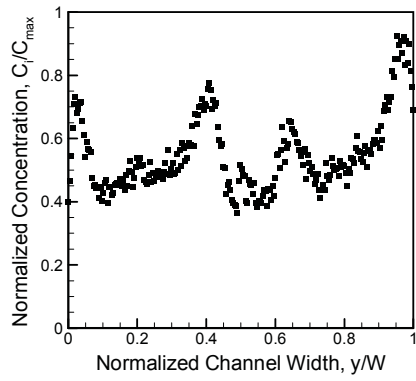**Figure C.1**: Re = 0.5.
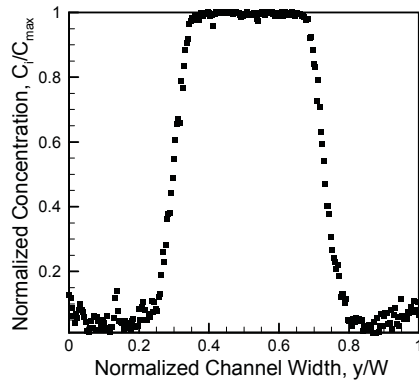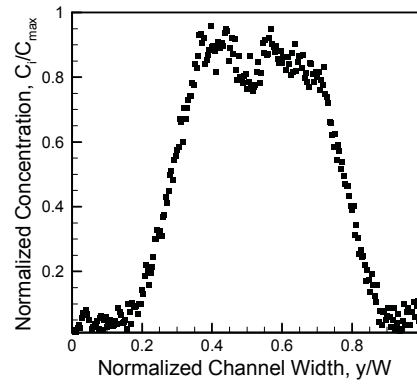
a) S1　　　　　　　　　　　b) S2
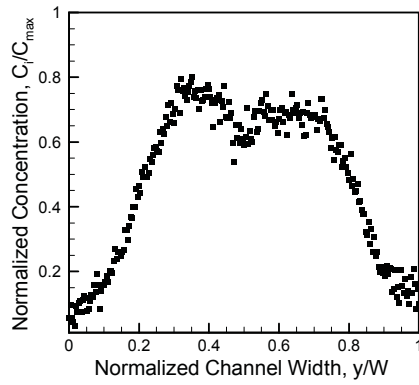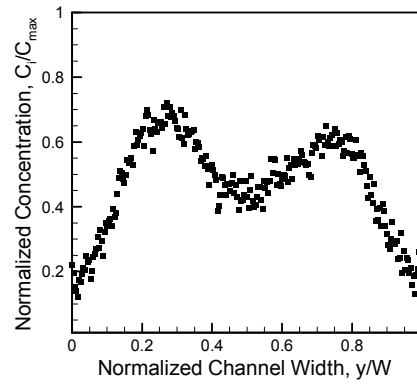
c) S3　　　　　　　　　　　d) S4
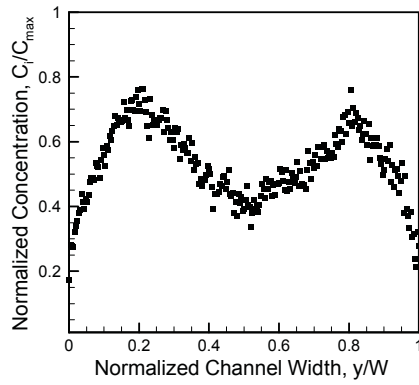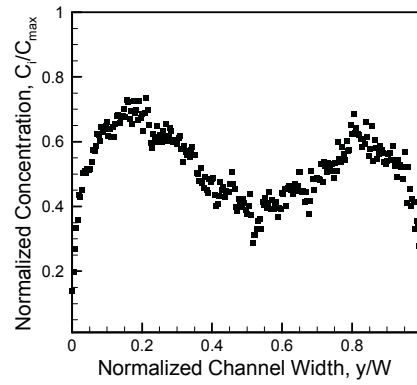
e) S5　　　　　　　　　　　f) S6

Figure C.2: Re = 1.

a) S1

b) S2

c) S3
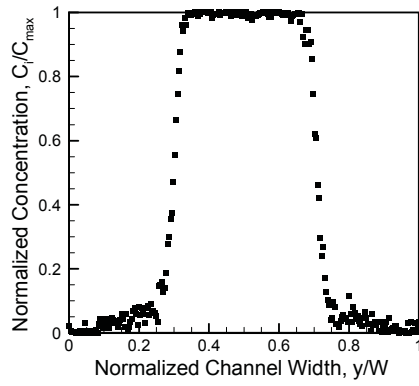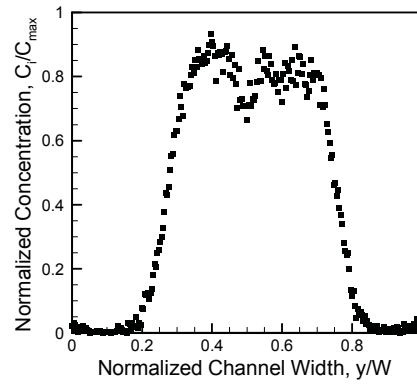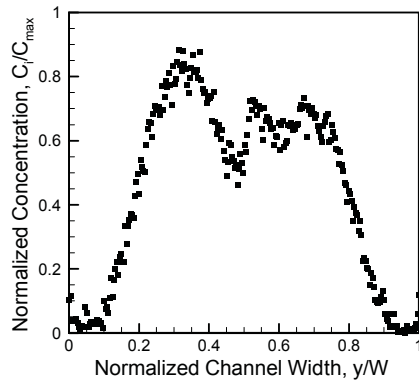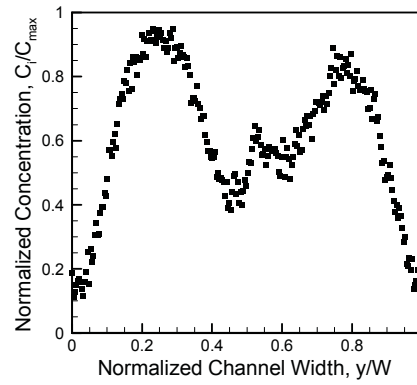
d) S4
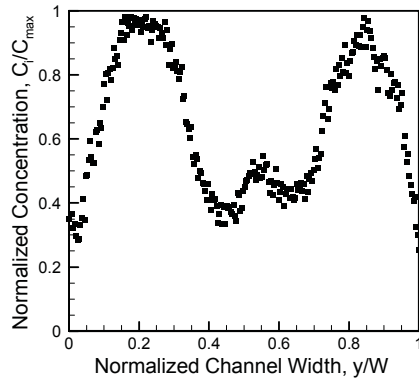
e) S5
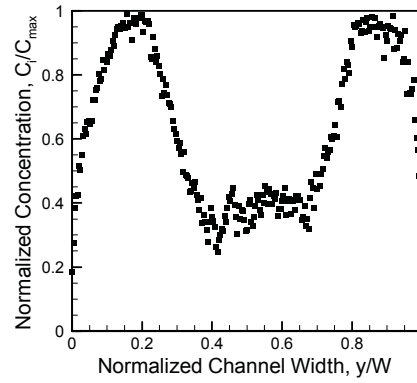
f) S6

Figure C.3: Re = 5.

a) S1

b) S2

c) S3
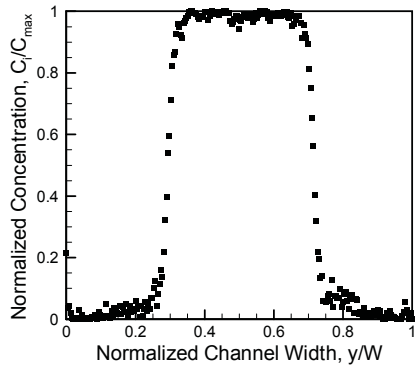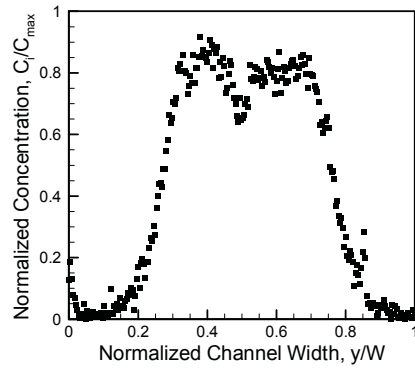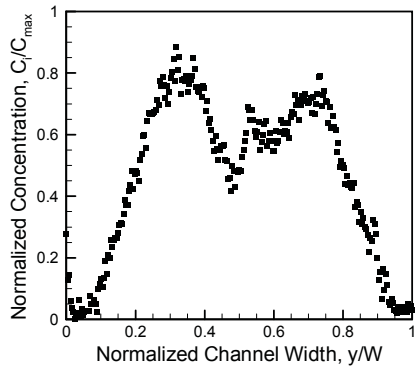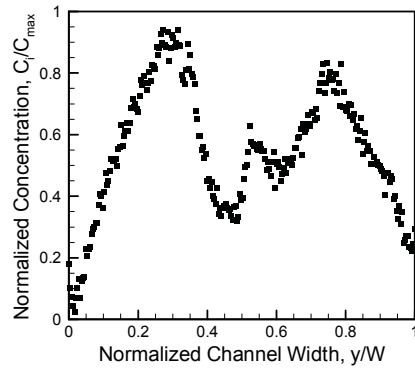
d) S4
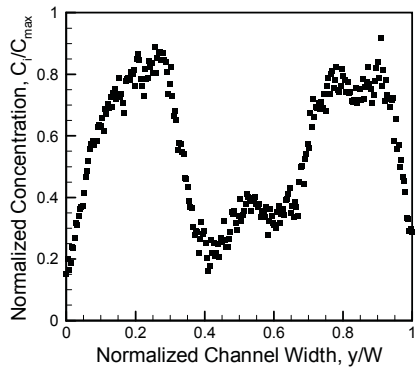
e) S5
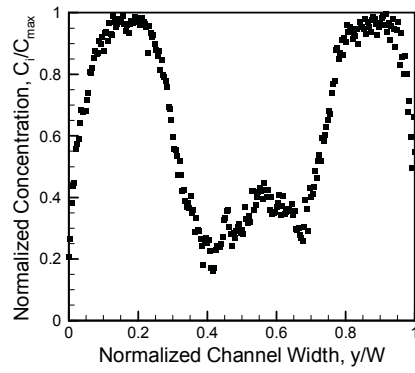
f) S6

Figure C.4: Re = 10.

a) S1

b) S2
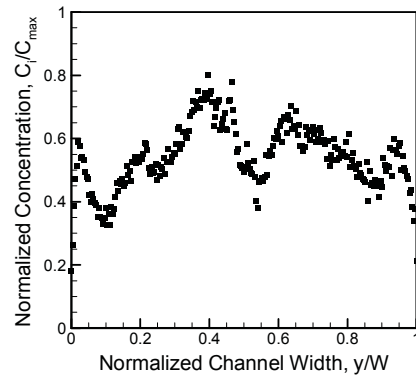
c) S3
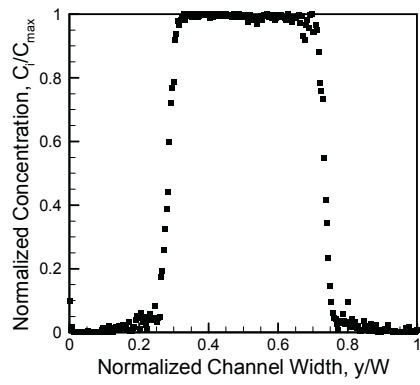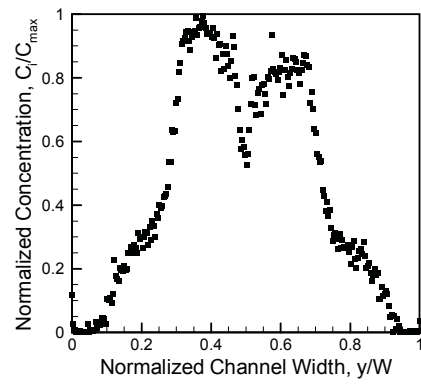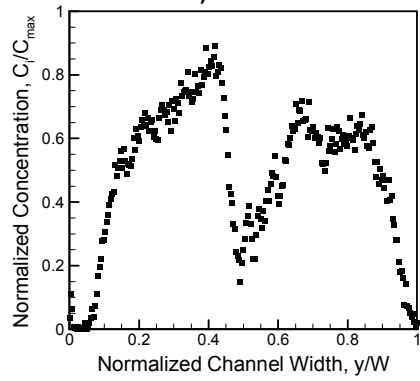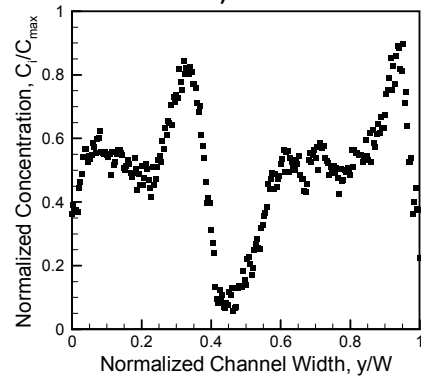
d) S4
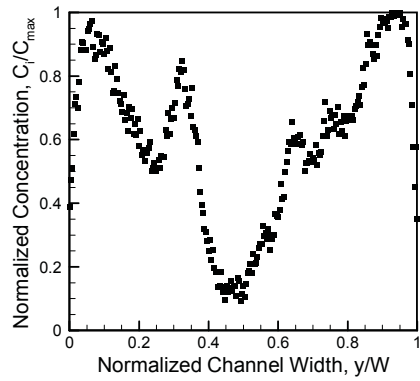
e) S5
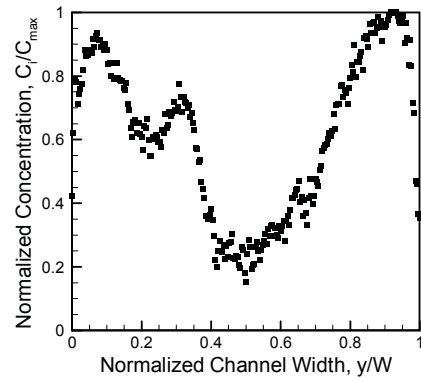
f) S6

Figure C.5: Re = 50.

a) S1

b) S2

c) S3
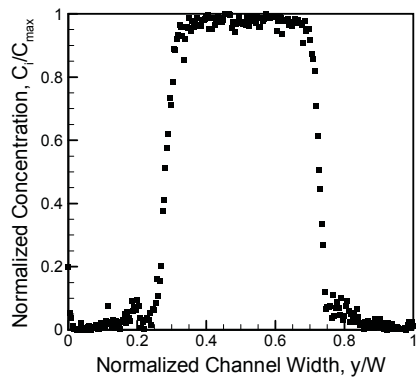
d) S4

e) S5

f) S6

Figure C.6: Re = 100.